Statistical Methods To Study Turbulence In The Magnetized Interstellar Medium

by

Dinesh Kandel

A thesis submitted in partial fulfillment of the requirements for the degree of

Master of Science

Department of Physics
University of Alberta

Abstract

It has been well known that turbulent motions are ubiquitous in the interstellar medium. These motions are very important in governing various astrophysical processes like star formation. Both observational and numerical studies are important to understand turbulent motions, and a gap between these two studies exists. To bridge this gap, various statistical techniques have been developed. These techniques so far have assumed isotropy and homogeneity in space. While this assumption is good in the absence of magnetic fields, isotropy is broken in the presence of magnetic field as the direction of magnetic field breaks the symmetry in space. In this thesis, we have developed an extension to current statistical techniques, which use intensity maps, such as velocity channel analysis and velocity centroids, to study turbulence anisotropy, and have discussed how statistical anisotropy of intensity maps can be used to study media magnetization, and separate different fundamental MHD modes: Alfvén, fast and slow modes.

Preface

This thesis is original work by Dinesh Kandel in collaboration with Prof. Alex Lazarian and Prof. Dmitri Pogosyan. The details and results presented in this thesis are published in Kandel et al. (2016a) and Kandel et al. (2016b).

"Big whirls have little whirls that feed on their velocity,
and little whirls have lesser whirls and so on to viscosity. "

Lewis F. Richardson

Acknowledgements

First and foremost, I want to thank my advisor Prof. Dmitri Pogosyan. It has been an honour to be his Masters student. He has truly inspired and taught me on carrying out theoretical physics research. I appreciate all the time he has given for productive and stimulating discussions, and the opportunities he has given me to attend research internship in Paris, and a conference in Germany. His support and encouragement have enormously helped me during any difficult moments I faced.

I would also like to thank my collaborator Prof. Alex Lazarian for providing me with interesting, and challenging research problems, and for hosting me in Madison for research collaboration. It was truly an honour to work with a brilliant scientist like him.

Finally, I would like to thank my family for all their love and encouragement. For my parents who curiously listened to what I do, despite having lack of any scientific background. And most of all for my loving, supportive, and encouraging girl friend Pratikshya who constantly cheered me up and supported me, especially, during the final stages of my Masters program. Thank you.

Contents

List of Tables

List of Figures

List of Abbreviations

List of commonly used abbreviations

AU	Astronomical unit (1.496×10^{11} m)
ISM	Interstellar medium
kpc	kiloparsec (3.086×10^{19} m)
LOS	Line-of-sight
MHD	Magnetohydrodynamic
PPP	Position-position-position
PPV	Position-position-velocity
UVC	Unnomalized velocity centroid
VCA	Velocity channel analysis
VC	Velocity centroid
VCS	Velocity coordinate spectrum

Chapter 1

Introduction

The interstellar medium (ISM) is turbulent on scales ranging from AU to kiloparsecs (kpc). The Big Power Law in the sky obtained with electron scattering and scintillations (Armstrong et al., 1995) and extended with Wisconsin Hα Mapper data in Chepurnov and Lazarian (2010) points towards the presence of astrophysical turbulence. Other numerous examples include non-thermal Doppler broadening of spectral lines, for e.g. 21 cm H I line, fluctuations of density and synchrotron emission (see Elmegreen and Scalo 2004; Mac Low and Klessen 2004; McKee and Ostriker 2007).

Observations show that our ISM is magnetised, suggesting that in such environment turbulence is magnetohydrodynamic (MHD). This MHD turbulence is accepted to be of key importance for fundamental astrophysical processes, e.g. star formation (see, e.g., McKee and Ostriker 2007), propagation and acceleration of cosmic rays (see Brandenburg and Lazarian 2013 and references therein).

How to study astrophysical turbulence? In recent years, there have been significant observational data sets available for study of turbulence. These include high resolution mapping of 21 cm H I line (Miville-Deschênes et al., 2003), H I absorption (Deshpande et al., 2000), map of dust emission (Miville-Deschênes et al., 2010), as well as ^{12}CO and ^{13}CO spectral line maps (Bensch

et al., 2001). At the same time, numerical simulations have demonstrated that they can produce synthetic data sets that resemble observations (see e.g. Federrath 2013) in terms of structures and scaling laws. However, because of their limited dynamical range, the range of turbulence scales obtained in simulations is rather limited.

Statistical studies represent the best hope of understanding observations, and bridging the gap between simulations and observations. Statistical descriptions are nearly indispensable strategy when dealing with turbulence, which is a stochastic and random process. The big advantage of statistical techniques is that they extract underlying regularities of the flow and reject incidental details. One of the main statistical measure of turbulence is the power spectrum, which can be used to compare observations with both numerical simulations and theoretical predictions. The energy spectrum $E(k)\mathrm{d}k$ of turbulence characterizes how much energy resides at the interval of wavenumbers $k, k+\mathrm{d}k$. On one hand, at large scales $l(\sim 1/k)$ which correspond to small k, one expects to observe features reflecting energy injection, while at small scales one should see the scales corresponding to dissipation of kinetic energy. On the other hand, the spectrum at intermediate scales, called inertial range, is determined by a complex process of energy transfer, which often leads to power-law spectra. For example, in the Kolmogorov description of unmagnetized incompressible turbulence, difference in velocities at different points in turbulent fluid increases on average with the separation between points as a cubic root of the separation, i.e. $|\delta v| \sim l^{1/3}$, which corresponds to the energy spectrum of $E(k) \sim k^{-5/3}$ in the inertial range. Thus, observational studies of the turbulence spectrum can determine sinks, sources and energy transfer mechanisms of astrophysical turbulence.

Beside the traditional power spectrum, there are many techniques that have been developed to study and parametrize observational magnetic turbulence. These include higher order spectra, such as the bispectrum (Burkhart et al.,

2009), higher order statistical moments (Kowal et al. 2007; Burkhart et al. 2009), density/column-density PDF analyses (Federrath et al. 2008; Burkhart and Lazarian 2012), topological techniques (such as genus, see Chepurnov et al. 2008), clump and hierarchical structure algorithms (such as dendrograms, see Rosolowsky et al. 2008; Burkhart et al. 2013), Delta variance analysis (Stutzki et al. 1998; Ossenkopf et al. 2008), principal component analysis (PCA; Heyer and Schloerb 1997; Heyer et al. 2008; Roman-Duval et al. 2011; Correia et al. 2016), Tsallis function studies for ISM turbulence (Esquivel and Lazarian 2010; Tofflemire et al. 2011), velocity channel analysis and velocity coordinate spectrum (Lazarian and Pogosyan 2004, 2006, 2008), structure/correlation functions as tests of intermittency and anisotropy (Cho and Lazarian 2003; Esquivel and Lazarian 2005; Kowal and Lazarian 2010; see also Federrath et al. 2009; Federrath et al. 2010; Konstandin et al. 2012), analysis of turbulence phase information (Burkhart and Lazarian, 2015), and also recent work on filament detection (see Smith et al. 2014; Federrath 2016) that links the structure and formation of filaments in the ISM to the statistics of turbulence.

There have been many attempts to obtain the turbulence spectra (see Münch and Wheelon 1958; Kleiner and Dickman 1985; O'dell and Castaneda 1987; Miesch et al. 1999) using intensity of emission lines. The fluctuations of intensity reflect the fluctuations of density of emitters as well as the velocity of their motion. Understanding these two effects, and separating their contribution motivated the study in Lazarian and Pogosyan (2000, 2004) (henceforth LP00 and LP04, respectively), which resulted in the analytical description of the statistical properties of intensity of Doppler-shifted emission lines in the position-position-velocity (PPV) space. In those papers, the observed statistics of intensity was related to the underlying 3D spectra of velocity and density, respectively, in the astrophysical turbulent volume. In LP00 the volume was considered transparent, but later in LP04, the treatment was generalized for the volume with self-absorption.

LP00 and LP04 proposed to analyse the intensity of velocity slices of PPV data cubes by gradually changing their thickness in order to find the underlying spectra of velocity and density of astrophysical turbulent motions. The technique was termed Velocity Channel Analysis (VCA), and has been successfully tested in a number of subsequent papers (Lazarian et al. 2001; Chepurnov and Lazarian 2009; Koch et al. 2017) and was successfully applied to a number of observations (see an incomplete list in Lazarian 2009).

Sky maps of velocity centroids (VC), which are intensity weighted mean velocities along V direction of PPV data cube, are another important technique to study ISM turbulence. The correlation of VC is shown to reflect the statistics of density and velocity field of turbulent media. Numerical study in Esquivel et al. (2007) shows that VC are not suitable for studies of supersonic turbulence, such as what is found in molecular clouds and diffuse cold ISM. However, they are particularly useful in studying velocity statistics of turbulent regions which are subsonic, for e.g. H II regions.

Previous VCA and VC techniques were developed in approximation of isotropic turbulence, which masked the magnetized nature of the medium. However, MHD turbulence is known to have anisotropic properties with magnetic field defining the preferred direction (Montgomery and Turner 1981; Shebalin et al. 1983; Higdon 1984). For the first time, the possibility of studying magnetic field with observational data was discussed in Lazarian et al. (2002). The numerical research that followed (see Esquivel and Lazarian 2005; Heyer et al. 2008; Burkhart et al. 2015) proved the utility of the studying anisotropies to obtain Alfvén Mach number of turbulence $M_{\rm A} \equiv V_L/V_{\rm A}$, where V_L and $V_{\rm A}$ are the injection and Alfvén velocities, respectively. Importantly, $M_{\rm A}$ determines magnetization of turbulence, and this determines crucial properties of turbulent fluid including diffusion of cosmic rays (see Yan and Lazarian 2002, 2004, 2008), heat (Narayan and Medvedev 2001; Lazarian 2006), as well as reconnection diffusion (Lazarian 2005; Santos-Lima et al. 2010, 2014; Lazarian

et al. 2012; Leão et al. 2013; González-Casanova et al. 2016; see Lazarian 2014 for a review), which has been identified as a crucial process for star formation (see Li et al. 2015).

In a recent study by Esquivel et al. (2015), the dependence of anisotropy of intensity fluctuations in velocity slices of PPV data cubes has been quantified using synthetic observations obtained from 3D MHD simulations. It confirmed that the anisotropy of the correlations of intensity in the velocity slice reflects the magnetic field direction and provided the empirical dependence of the observed anisotropy on the Alfvén Mach number $M_{\rm A}$. This work motivates our present analytical study aimed at the analytical description of the anisotropies in the velocity slices of PPV data cubes.

In this thesis, we have developed theory of VCA and VC for fully anisotropic MHD turbulence. We use the modern representation of MHD turbulence as the combination of three cascades, i.e. the Alfvén, fast and slow modes (see Goldreich and Sridhar 1995; Lithwick and Goldreich 2001; Cho and Lazarian 2002, 2003; Kowal and Lazarian 2010). For the purpose of observational studies, we describe magnetic fluctuations in the frame of the mean magnetic field, which is different from the local magnetic field of reference used in the theory of turbulence (see Cho and Lazarian 2003). Similar approach was adopted in Lazarian and Pogosyan (2012, 2016) (henceforth, LP12 and LP16 respectively) to study anisotropy of synchrotron fluctuations, and their polarizations. We have shown that the anisotropies produced by different MHD modes to be different which opens a way to separate the contributions from these different modes, allowing us to potentially separate incompressible and compressible turbulence. We have also shown the dependence of anisotropy of correlation of channel maps intensity as well as correlation of VC in Alfvén Mach number.

VCA and VC provide a way of studying astrophysical turbulence by making use of extensive spectroscopic surveys, in particular H I and CO data. The present study significantly enhances their value and abilities by extending

these techniques to account for anisotropy of turbulent media. Such study of turbulence anisotropies will help determine various magnetic properties of a turbulent gas cloud.

Chapter 2

Basic statistics of turbulence

Turbulence is highly non-linear and random phenomenon, and therefore physically important quantities like velocity $\mathbf{v}$, pressure p, magnetic field $\mathbf{B}$, density ρ are random functions of position $\mathbf{x}$. Two important statistical descriptors of a random quantity $\mathcal{A}$ are the correlation function

$$\xi(\mathbf{x}_1, \mathbf{x}_2) = \langle \mathcal{A}(\mathbf{x}_1)\mathcal{A}(\mathbf{x}_2) \rangle \ , \tag{2.1}$$

and the structure function

$$d(\mathbf{x}_1, \mathbf{x}_2) = \left\langle (\mathcal{A}(\mathbf{x}_1) - \mathcal{A}(\mathbf{x}_2))^2 \right\rangle \ . \tag{2.2}$$

We assume turbulence to be homogeneous, in which case the correlation and structure function is a function of radial separation, i.e. $\xi(\mathbf{x}_1, \mathbf{x}_2) = \xi(\mathbf{x}_1 - \mathbf{x}_2) = \xi(\mathbf{r})$ and the same for structure function. In addition, if turbulence is assumed to be isotropic, correlation and structure functions are purely dependent on scalar separation, i.e. $\xi(\mathbf{x}_1, \mathbf{x}_2) = \xi(r)$, and so on. The assumption of isotropy is not suitable for a magnetised media, however.

Scaling of power distribution of random fields are of two types: steep and shallow. For a steep field, power of fluctuations is dominated by moderate to large scale fluctuations, while for shallow field, power is dominated by small

scale fluctuations. Depending upon whether fluctuations are steep or shallow, it is appropriate to either use structure function or use correlation function, respectively. A major difference between correlation function and structure function is that, while structure function at scale r is determined by the integrated power of fluctuations over scales smaller than r, correlation function is determined by the integral of the power over scales larger than r.

Observations show that velocity spectra in the ISM is steep, while density can be either steep or shallow. Scaling properties of turbulence typically lead to power-law spectra in the inertial range between injection-scale and dissipation scale. Leaving discussion of angular dependence of velocity and density statistics to further relevant sections, we thus take the LOS velocity structure function as

$$D_z(r) = D_z(S) \left(\frac{r}{S}\right)^{\nu} , \qquad r < S \tag{2.3}$$

where $\nu > 0$. In the above equation, S is the injection scale of turbulence, and for isolated clouds, we assume that S is comparable to the size of the cloud. Modelling of the structure function outside the inertial range $r > S$ requires modelling of the injection process. The correlation length of velocity field is comparable to the energy injection scale.

Similarly, the structure function of steep density field is taken to be

$$D_\rho(r) \approx 2\sigma_\rho^2 \left(\frac{r_c}{r}\right)^{-\nu_\rho} , \quad \nu_\rho < 0 , \quad r < r_c , \tag{2.4}$$

while for shallow density spectrum, the density correlation is modelled as

$$\xi_\rho(r) \approx \rho_0^2 + \sigma_\rho^2 \left(\frac{r_c}{r}\right)^{\nu_\rho} , \quad \nu_\rho > 0 , \quad r > r_c , \tag{2.5}$$

where ρ_0 is the mean density, σ_ρ the density dispersion, and r_c the correlation length of the density field. In the case steep density field, r_c is comparable to the size of injection scale, i.e. $r_c \sim S$, and the power law scaling regime lies

at $r < r_c$, while for shallow density, r_c is small, and the power law scaling is exhibited at $r > r_c$. In the subsequent parts of this thesis, we use Eq. (2.4) when $\nu_\rho < 0$ and Eq. (2.5) when $\nu_\rho > 0$.

2.1 Velocity correlation tensor for MHD turbulence

To describe turbulence in ISM, one should account for the magnetization of the media. In MHD turbulence, there exists a preferred direction pointing towards the direction of mean magnetic field; therefore, the concept of isotropy applicable to hydrodynamic Kolmogorov turbulence breaks down, and the turbulent statistics are anisotropic. Here we adopt the same representation of the anisotropic MHD turbulence using axisymmetric tensors, as the one developed in LP12 in the framework of studies of anisotropies of synchrotron intensities (see more justification in LP12).

In what follows, we are describing the statistics of anisotropic velocity field, which has many similarities with the statistics of anisotropic turbulent magnetic field described in LP12. We would like to stress that the description of MHD turbulence deeply entrenched in the literature is based on a model having mean magnetic field plus *isotropic* fluctuations, which contradicts theoretical, numerical and observational studies of magnetized turbulence and therefore should be discarded[1]. Indeed, MHD turbulence is neither isotropic nor can it be represented by mean field with isotropic fluctuations. The correct description of MHD turbulence involves the combination of three different cascades with different degree of fluctuation anisotropies, and this is the description we use in the present work.

Following the notation of Chandrasekhar (1950), the velocity correlation

[1]We note that the present day models of the cosmic microwave background foreground still use this erroneous model for representing magnetic fields.

tensor of axisymmetric turbulence is

$$\langle v_i(\mathbf{x}_1)v_j(\mathbf{x}_2)\rangle = A\hat{r}_i\hat{r}_j + B\delta_{ij} + C\hat{\lambda}_i\hat{\lambda}_j + D\left(\hat{\lambda}_i\hat{r}_j + \hat{\lambda}_i\hat{r}_j\right) \ , \qquad (2.6)$$

where $\hat{\lambda}$ unit vector specifies the preferred direction [2], and the coefficients A, B, C and D are functions of r and $\mu = \hat{\mathbf{r}} \cdot \hat{\lambda}$. For isotropic turbulence, the coefficients C and D of the velocity correlation tensor are zero. At zero separation, $\mathbf{r} \to 0$, the correlation function gives the variance tensor

$$\langle v_i(\mathbf{x}_1)v_j(\mathbf{x}_1)\rangle = B(0)\delta_{ij} + C(0)\hat{\lambda}_i\hat{\lambda}_j. \qquad (2.7)$$

Similarly, we can define the structure function tensor for the velocity field

$$D_{ij}(\mathbf{r}) \equiv \langle (v_i(\mathbf{x}_1) - v_i(\mathbf{x}_2))\,(v_j(\mathbf{x}_1) - v_j(\mathbf{x}_2))\rangle \, . \qquad (2.8)$$

The main quantity that will appear in our analysis is the z- projection of the velocity structure function

$$D_z(\mathbf{r}) = D_{ij}\hat{z}_i\hat{z}_j = 2[(B(0) - B(r,\mu)) + (C(0) - C(r,\mu))\cos^2\gamma \\ -A(r,\mu)\cos^2\theta - 2D(r,\mu)\cos\theta\cos\gamma] \ . \qquad (2.9)$$

There are four angles that we keep track of. First, we have θ and ϕ which are spherical coordinates of the separation vector in the frame where the z-axis is aligned with the LOS and the x-axis is aligned with projection of the symmetry axis on the plane of the sky. Dependence of the observed intensity correlation on ϕ is the main focus of the thesis, while θ get integrated along the LOS. Angle γ is a fixed parameter of the problem that describes the direction of the mean magnetic field with respect to the z-axis. Lastly, μ is angle between the separation vector and the symmetry axis. The local axisymmetric properties of

[2] All results are invariant under replacement of $\hat{\lambda}$ by $-\hat{\lambda}$ that specify the same axis.

the turbulence models depend explicitly on μ only. Between these four angles there is a relation

$$\mu(\gamma, \theta, \phi) = \sin\gamma \sin\theta \cos\phi + \cos\gamma \cos\theta. \tag{2.10}$$

Eq. (2.9) is the general form of (2.3) for the case of anisotropic MHD turbulence. The power-law behaviour is shown by the coefficients $B(0) - B(r, \mu)$, etc.

2.2 Representing MHD Turbulence Modes

Before we proceed with the formal mathematical description, a few statements about the properties of MHD turbulence are due (see a more detailed discussion in Brandenburg and Lazarian 2013). It is natural to accept that the properties of MHD turbulence depend on the degree of magnetization. Those can be characterized by the Alfvén Mach number $M_{\rm A} = V_L/V_{\rm A}$, where V_L is the injection velocity at the scale S and $V_{\rm A}$ is the Alfvén velocity. It is intuitively clear that for $M_{\rm A} \gg 1$ magnetic forces should not be important in the vicinity of injection scale. This is the limiting case of super-Alfvénic turbulence. The case of $M_{\rm A} = 1$ is termed trans-Alfvénic and the case of $M_{\rm A} < 1$ sub-Alfvénic turbulence. Naturally, $M_{\rm A} \ll 1$ should correspond to magnetic field with only marginally perturbed field direction, since in this case strong magnetic field resists motion of gas.

The modern theory of MHD turbulence started with the seminal paper by Goldreich and Sridhar (1995), (henceforth GS95). They suggested the theory of turbulence of Alfvénic waves or Alfvénic modes, as in turbulence non-linear interactions modify wave properties significantly. For instance, in GS95 theory Alfvénic perturbations cascade to a smaller scale in just about one period ($\equiv l/v_l$, l being the eddy size), which is definitely not a type of linear wave behaviour. The GS95 was formulated for trans-Alfvénic turbulence, e.g. for

$M_{\rm A} = 1$. The generalization of GS95 for $M_{\rm A} < 1$ and $M_{\rm A} > 1$ can be found in Lazarian and Vishniac (1999) (henceforth LV99).

The original GS95 theory was also augmented by the concept of local system of reference (LV99; Cho and Vishniac 2000; Maron and Goldreich 2001; Cho et al. 2002) that specifies that the turbulent motions should be viewed not in the system of reference of the mean magnetic field, but in the system of reference of magnetic field comparable with the size of the eddies. From the point of view of the observational study that we deal with in this thesis, the local system of reference is not available. Therefore, we should view Alfvénic turbulence in the global system of reference which for sub-Alfvénic turbulence is related to the mean magnetic field (see the discussions in Cho and Lazarian 2002; Esquivel and Lazarian 2005; LP12). In this system of reference, the observed statistics of turbulence is somewhat different. While in GS95 there are two different energy spectra, namely, the parallel and perpendicular, in the global system of reference the perpendicular fluctuations dominate which allows us to use a single spectral index for the two directions in our treatment. Similarly, if in the local system of reference, the anisotropy is increasing with the decrease of size of the eddies, it stays constant in the global system of reference. It is this property that allows the theoretical description for axisymmetric turbulence by Chandrasekhar (1950) in order to describe observed turbulent fluctuations.

For super-Alfvénic turbulence, the turbulent motions are essentially hydrodynamic up to the scale of $l_A = LM_{\rm A}^{-3}$ and after that scale they follow along the GS95 cascade. If we observe Alfvénic turbulence at scales larger than l_A, we will not see anisotropy. However, if our tracers are clustered on scales less than $l_{\rm A}$, we will see the anisotropy corresponding to the size of largest eddy. For instance, for a turbulent molecular cloud, scales less than $l_{\rm A}$ will show anisotropy.

For sub-Alfvénic turbulence, the original cascade is *weak* with parallel scale of perturbations of magnetic field not changing, while the perpendicular scale

getting smaller and smaller as the turbulence cascades (see LV99). However, at scale $l_{\rm trans} \sim LM_{\rm A}^2$ the turbulence gets *strong* in terms of its non-linear interactions, with the modified GS95 scalings (see LV99) being applicable.

To obtain the full description of MHD turbulence, the motions in an isothermal turbulent plasma can be decomposed into three types of MHD modes —Alfvén, fast and slow modes. While the entrenched notion in literatures is that for compressible turbulence Alfvén, slow and fast modes are strongly coupled and therefore cannot be considered separately, the numerical study in Cho and Lazarian (2003) provided a decomposition of the modes and proved that they form cascades of their own (see a bit more sophisticated method of decomposition employed in Kowal and Lazarian 2010). This was used in LP12 to provide the representation of these modes for the observational studies of magnetic field. In what follows, we discuss the turbulent velocity field, which entails some modifications compared to LP12.

The power law scaling of modes is defined by the theory but exact spectral index of each mode may depend on the turbulent environment. Therefore, following the tradition of VCA development (LP00) and our synchrotron studies (LP00; LP16), for the purpose of our observational study, we keep the indices of velocity and density as parameters that can be established by observations. This is intended to provide a test using the VCA of the modern MHD theory and induce its further development.

In this thesis, our focus is to understand how turbulence anisotropies transfer into the anisotropy of the statistics of intensity fluctuations within PPV slices and how the latter statistics changes with the thickness of the slices. As was shown in LP00, the statistics of intensity fluctuations within a PPV slice can be affected by both the velocity statistics and density statistics, and there are regimes when only velocity fluctuations determine the fluctuations of intensity within a thin slice. In this section we shall discuss correlation tensors of velocity fields $\langle v_i(\mathbf{x}_1) v_j(\mathbf{x}_1+\mathbf{r})\rangle$ generated by each MHD modes. In

contrast to the magnetic field, velocity field is not necessarily divergence free, since turbulence can be compressible.

The details of the velocity correlation tensor of each mode depend on the allowed displacement of plasma $\hat{\xi}$ in the mode and the distribution of power among different wavelengths. We start our consideration in Fourier space. In general, the Fourier component of velocity in a mode is given by $\mathbf{v}(\mathbf{k}) = a_{\mathbf{k}}\hat{\xi}(\hat{\mathbf{k}}, \hat{\lambda})$, where $\mathbf{k}$ is the wavevector, $a_{\mathbf{k}}$ is the random complex amplitude of a mode and $\hat{\xi}$ is the direction of allowed displacement. Therefore, the velocity correlation is given in Fourier space by

$$\langle v_i(\mathbf{k}) v_j^*(\mathbf{k}')\rangle = \langle a_{\mathbf{k}} a_{\mathbf{k}'}^*\rangle \left(\hat{\xi}_{\mathbf{k}} \otimes \hat{\xi}_{\mathbf{k}'}^*\right)_{ij} \equiv \mathcal{A}(k, \hat{\mathbf{k}}\cdot\hat{\lambda}) \left(\hat{\xi}_{\mathbf{k}} \otimes \hat{\xi}_{\mathbf{k}}^*\right)_{ij} \delta(\mathbf{k}-\mathbf{k}'), \tag{2.11}$$

where $\mathcal{A}(k, \hat{\mathbf{k}}\cdot\hat{\lambda}) = \langle \hat{a}_{\mathbf{k}} \hat{a}_{\mathbf{k}}^*\rangle$ is the power spectrum which in our case depends on the angle $\mu_k \equiv \hat{\mathbf{k}}\cdot\hat{\lambda}$. Fourier transform of Eq. (2.11) gives velocity correlation tensor in the real space

$$\langle v_i(\mathbf{x}_1) v_j(\mathbf{x}_1+\mathbf{r})\rangle = \int \mathrm{d}k\, k^2\, \mathrm{d}\Omega_k\, \mathrm{e}^{i\mathbf{k}\cdot\mathbf{r}} \mathcal{A}(k, \hat{\mathbf{k}}\cdot\hat{\lambda}) \left(\hat{\xi}_{\mathbf{k}} \otimes \hat{\xi}_{\mathbf{k}}^*\right)_{ij}. \tag{2.12}$$

The power spectrum can be decomposed into spherical harmonics as

$$\mathcal{A}(k, \hat{\mathbf{k}}\cdot\hat{\lambda}) = \sum_{\ell_1 m_1} \frac{4\pi}{2\ell_1+1} \mathcal{A}_{\ell_1}(k) Y_{\ell_1 m_1}(\hat{\mathbf{k}}) Y_{\ell_1 m_1}^*(\hat{\lambda}), \tag{2.13}$$

and similarly

$$\left(\hat{\xi}_{\mathbf{k}} \otimes \hat{\xi}_{\mathbf{k}}^*\right)_{ij} = \sum_{\ell_2 m_2} c_{\ell_2 m_2}^{ij}(\hat{\lambda}) Y_{\ell_2 m_2}(\hat{\mathbf{k}}) \ , \tag{2.14}$$

where $c_{\ell_2 m_2}^{ij}$ coefficients depend on the mode structure, and are tabulated further in this section for each mode. With these definitions, Eq. (2.12) can be

expressed as

$$\langle v_i v_j \rangle = \sum_{\ell m} 4\pi \mathrm{i}^{\ell} Y^*_{\ell m}(\hat{r}) \sum_{\ell_1 m_1} \frac{4\pi}{2\ell_1 + 1} Y^*_{\ell_1 m_1}(\hat{\lambda}) \sum_{\ell_2 m_2} c^{ij}_{\ell_2 m_2}(\hat{\lambda}) \mathcal{T}_{\ell \ell_1}(r) \Psi_{\ell m, \ell_1 m_1, \ell_2 m_2} \ , \tag{2.15}$$

where we have defined

$$\mathcal{T}_{\ell \ell_1}(r) \equiv \int \mathrm{d}k \, k^2 j_{\ell}(kr) \mathcal{A}_{\ell_1}(k), \tag{2.16}$$

and Ψ is a shorthand notation for the combination of Wigner 3-j symbols given in detail in Appendix B. On the other hand, the velocity structure tensor is given by Eq.(2.6), and therefore, the above equations can be used to find the coefficients A, B, C and D. The procedure that we use to obtain them is also described in Appendix B.

The intensity statistics of a turbulent field is also affected by the density fluctuations. In a turbulent field, if density fluctuations are weak, it is easy to understand density correlation for different modes from linear treatment of continuity equation. Assuming that the density is given by $\rho \to \rho_o + \delta\rho$, where ρ_0 is the mean density of the turbulent medium and $\delta\rho$ is the overdensity such that $|\delta\rho| \ll \rho_0$, the continuity equation

$$\frac{\partial \rho}{\partial t} + \nabla \cdot (\rho \mathbf{v}) = 0, \tag{2.17}$$

gives (in Fourier space) $\delta\rho_{\mathbf{k}}/\rho_0 \sim \hat{a}(\hat{k} \cdot \hat{\xi})$, using which we obtain the over-density power spectrum

$$\langle \delta\rho_{\mathbf{k}} \delta\rho^*_{\mathbf{k}} \rangle = \rho_0^2 \mathcal{A}(k, \hat{\mathbf{k}} \cdot \hat{\lambda}) |\hat{k} \cdot \hat{\xi}|^2. \tag{2.18}$$

In real space, the overdensity correlation is given by

$$\langle \delta\rho(\mathbf{x}_1) \delta\rho(\mathbf{x}_1 + \mathbf{r}) \rangle = \rho_0^2 \int \mathrm{d}k \, k^2 \, \mathrm{d}\Omega_k \, \mathrm{e}^{i\mathbf{k}\cdot\mathbf{r}} \mathcal{A}(k, \hat{\mathbf{k}} \cdot \hat{\lambda}) |\hat{k} \cdot \hat{\xi}|^2. \tag{2.19}$$

These equations for density correlation are only valid when density perturbations are weak. Linear approximation is not appropriate for high sonic Mach number turbulence, as in this case density perturbations are caused by shocks, and these perturbations are comparable to the density itself (Beresnyak et al. 2005; Kowal et al. 2007).

To understand the effects of non-linear density fluctuations in the intensity statistics, we propose the following ansatz for the density correlation function $\xi(\mathbf{r}, \mu)$. This ansatz is based on the results of Jain and Kumar (1961) where density statistics is presented as a infinite series over spherical harmonics. We take only up to the second harmonics and in the case of shallow spectrum:

$$\xi(\mathbf{r}, \mu) = \langle\rho\rangle^2 \left[1 + \left(\frac{r_c}{r}\right)^{\nu_\rho} (1 + c_\rho P_2(\mu))\right], \qquad \nu_\rho > 0, \tag{2.20}$$

whereas in the case of steep spectrum for $r \ll r_c$:

$$\xi_\rho(\mathbf{r}, \mu) = \langle\rho\rangle^2 \left[1 - \left(\frac{r_c}{r}\right)^{\nu_\rho} (1 + c_\rho P_2(\mu))\right], \qquad \nu_\rho < 0, \tag{2.21}$$

where r_c denotes a cut-off scale, and c_ρ is a parameter, which depends on the details of the turbulent mode. An important criterion that the two ansatz presented above should satisfy in order to be called a 'correlation function' is that their Fourier transform should be positive definite. It can be shown that this condition is true only when the following condition is satisfied:

$$c_\rho > \frac{2\nu_\rho}{3 - \nu_\rho}, \tag{2.22}$$

for steep spectra whereas for shallow spectra the condition is

$$c_\rho < \frac{2\nu_\rho}{3 - \nu_\rho}. \tag{2.23}$$

Our representation above captures several essential features. First, the

above correlation can be immediately broken into two parts: a constant and a part with spatial and angular dependence. With this it is natural to talk about pure velocity and pure density effects, and equations (3.8) and (A.9) become applicable. Second important feature of the above correlation is that it carries information about anisotropy. In an axisymmetric turbulence, only even harmonics survive due to symmetry and therefore, $P_2(\mu)$ is the dominant term which carries information on the anisotropy[3].

Now we describe the properties of individual MHD modes. For compressible modes, these properties vary depending on the magnetization of the media, which are determined by the parameter β, which is the ratio of thermal plasma energy density to the energy density of magnetic field. Thus this ratio, in addition to $M_{\rm A}$ should be considered. To describe correlation tensors of these modes we use their dispersion relations. Our treatment of MHD modes below is analogous to the one in LP12. Below we treat velocity fluctuations associated with MHD modes, while LP12 dealt with magnetic fluctuations. A brief summary of mode structures is also presented in Table 2.1.

2.2.1 Alfvén mode

Alfvén modes are essentially incompressible modes where displacement of plasma in an Alfvén wave is orthogonal to the plane spanned by the magnetic field and wavevector, so that

$$\mathbf{v}_A \propto \hat{\xi}_{\mathbf{k}} = \frac{\hat{\mathbf{k}} \times \hat{\lambda}}{\sqrt{1-(\hat{\mathbf{k}}\cdot\hat{\lambda})^2}}. \tag{2.24}$$

The corresponding tensor structure for Alfvén mode is then

$$(\hat{\xi}_{\mathbf{k}} \otimes \hat{\xi}^*_{\mathbf{k}})_{ij} = (\delta_{ij} - \hat{k}_i\hat{k}_j) - \frac{(\hat{\mathbf{k}}\cdot\hat{\lambda})^2\hat{k}_i\hat{k}_j - (\hat{\mathbf{k}}\cdot\hat{\lambda})(\hat{\lambda}_i\hat{k}_j + \hat{\lambda}_j\hat{k}_i) + \hat{\lambda}_i\hat{\lambda}_j}{1-(\hat{\mathbf{k}}\cdot\hat{\lambda})^2}, \tag{2.25}$$

[3]For a highly anisotropic density fluctuation, higher order harmonics also contribute. We are, however, only concerned with the mild density anisotropy.

In the above equation, the part in the first parentheses is referred to as E-type correlation, and the second part is referred to as F-type correlation. The E-type correlation has been studied in detail in LP12.

In the case of Alfvén mode, the power spectrum in the global system of reference is given by

$$\mathcal{A}(k,\mu_k) = E(k,\mu_k) \propto k^{-11/3} \exp\left[-M_{\rm A}^{-4/3} \frac{|\mu_k|}{(1-\mu_k^2)^{2/3}}\right], \tag{2.26}$$

where $\mu_k = \hat{\mathbf{k}} \cdot \hat{\lambda}$.

The correlation tensor of Alfvén mode in real space is calculated in Appendix C.1. The coefficients A, B, C and D are given by Eqs. (C.5), (C.9), (C.11) and (C.10), respectively.

As Alfvén modes are incompressible, to the first-order approximation, they do not create any density fluctuations. Indeed, for Alfvén waves, $\hat{\xi}$ is orthogonal to wavevector, and therefore the overdensity correlation must be zero (cf. Eq. (2.19)).

2.2.2 Fast mode

Fast modes are compressible type of modes. In high-β ($\equiv P_{\rm gas}/P_{\rm mag}$) plasma, they behave like acoustic waves, while in low-β plasma they propagate with Alfvén speed irrespective of the magnetic field strength (Cho and Lazarian, 2005). The power spectrum of this mode is isotropic and is given by

$$\mathcal{A}(k,\mu_k) \propto k^{-7/2}. \tag{2.27}$$

In this subsection, we will present the velocity correlation tensor as well as over-density correlation for fast modes in two regimes: high and low β.

High-β regime

In the high-β regime, displacement in fast modes is parallel to wavevector $\hat{k}$, and the velocity is $\mathbf{v} \propto \hat{k}$. These are essentially sound waves compressing magnetic field. This mode is purely compressional type, and its tensor structure in Fourier space is given by

$$\left(\hat{\xi}_{\mathbf{k}} \otimes \hat{\xi}^*_{\mathbf{k}}\right)_{ij} = \hat{k}_i \hat{k}_j. \tag{2.28}$$

The correlation tensor structure of fast modes in real space is presented in Appendix C.2. It has been shown that C and D parameters of this mode vanish, while A and B are given by Eqs. (C.14) and (C.16), respectively.

In the case when density perturbations are weak, the over-density correlation in fast modes in high-β regime is (cf. Eq.(2.19))

$$\langle \delta\rho(\mathbf{x}_1)\delta\rho(\mathbf{r}+\mathbf{x}_1)\rangle = \int \mathrm{d}^3\mathbf{k} \mathrm{e}^{i\mathbf{k}.\mathbf{r}} k^{-7/2} = 4\pi \int \mathrm{d}k\, k^{-3/2} j_0(kr). \tag{2.29}$$

Note that the above correlation represents steep density spectra for which structure function should be used for appropriate analysis to avoid divergence issues.

Low β regime

In the low-β regime, velocity is orthogonal to the direction of symmetry $\hat{\lambda}$, and therefore, the velocity is

$$\mathbf{v} \propto \hat{\xi}_{\mathbf{k}} = \frac{(\hat{\lambda} \times \hat{\mathbf{k}}) \times \hat{\lambda}}{\sqrt{1 - (\hat{\mathbf{k}} \cdot \hat{\lambda})^2}}. \tag{2.30}$$

This mode can be associated with compression of magnetic field. Using the above equation, we have

$$\left(\hat{\xi}_{\mathbf{k}} \otimes \hat{\xi}^*_{\mathbf{k}}\right)_{ij} \propto \frac{\hat{k}_i\hat{k}_j - (\hat{\mathbf{k}} \cdot \hat{\lambda})(\hat{k}_i\hat{\lambda}_j + \hat{k}_j\hat{\lambda}_i) + (\hat{\mathbf{k}} \cdot \hat{\lambda})^2\hat{\lambda}_i\hat{\lambda}_j}{1 - (\hat{\mathbf{k}} \cdot \hat{\lambda})^2}. \tag{2.31}$$

Table 2.1: Summary of mode structure

Mode	*Power spectrum*	*Type*	*Equation*
Alfvén	Anisotropic	Solenoidal	2.25, 2.26
Fast (high β)	Isotropic	Potential	2.28, 2.27
Fast (low β)	Isotropic	Compressible	2.31, 2.27
Slow (high β)	Anisotropic	Solenoidal	2.34, 2.26
Slow (low β)	Anisotropic	Compressible	2.34, 2.26
Strong	Anisotropic	Solenoidal	C.33

The velocity correlation function in real space for the above tensor is presented in the Appendix C.3. Because the power spectrum for this mode is isotropic, the correlation tensor is heavily simplified. The parameters A, B, C and D for this mode are presented in Eqs. (C.18), (C.19), (C.20) and (C.21).

In the case when density perturbations are weak, the over-density correlation in fast modes in low β regime is (cf. Eq.(2.19))

$$\begin{aligned}\langle\delta\rho(\mathbf{x}_1)\delta\rho(\mathbf{r}+\mathbf{x}_1)\rangle &= \int \mathrm{d}^3\mathbf{k}\mathrm{e}^{i\mathbf{k}.\mathbf{r}}k^{-7/2}(1-(\hat{\mathbf{k}}\cdot\hat{\lambda})^2)\\ &= \frac{4\pi}{3}\int \mathrm{d}k\, k^{-3/2}j_0(kr) + \frac{8\pi}{3}\int \mathrm{d}k\, k^{-3/2}j_2(kr)P_2(\mu). \qquad (2.32)\end{aligned}$$

2.2.3 Slow mode

Slow modes in high-β plasma are similar to pseudo-Alfvén modes in incompressible regime, while at low-β they are density perturbations propagating with sonic speed parallel to magnetic field (see Cho and Lazarian 2003). The power spectrum of this mode is the same as that of Alfvén mode (cf equation 2.26).

In this section, we will present the velocity correlation and over-density correlation of this mode in low- and high-β regime.

High-β

In the high-β regime, displacement is perpendicular to the wavevector $\hat{k}$, and therefore,

$$\mathbf{v} \propto (\hat{\mathbf{k}} \times \hat{\lambda}) \times \hat{k} \ . \tag{2.33}$$

Therefore, this gives us a full tensor structure is

$$\left(\hat{\xi}_{\mathbf{k}} \otimes \hat{\xi}^*_{\mathbf{k}}\right)_{ij} = \frac{(\hat{\mathbf{k}} \cdot \hat{\lambda})^2 \hat{k}_i \hat{k}_j - (\hat{\mathbf{k}} \cdot \hat{\lambda})^2 (\hat{\lambda}_i \hat{k}_j + \hat{\lambda}_j \hat{k}_i) + \hat{\lambda}_i \hat{\lambda}_j}{1 - (\hat{\mathbf{k}} \cdot \hat{\lambda})^2}. \tag{2.34}$$

Slow modes are essentially incompressible types of mode in this regime. The above tensor structure is pure F-type, and the F-type correlation tensor in real space is derived in Appendix C.4. The correlation parameters A, B, C and D are presented in Eqs. (C.24), (C.26), (C.30) and (C.28).

Slow modes in high-β regime have zero density fluctuations in a turbulent field where density perturbations are sufficiently weak (cf. Eq. (2.19)).

Low β

In this case, the displacement is parallel to the symmetry axis $\hat{\lambda}$, and therefore, the correlation tensor is $\langle v_i v_j \rangle \propto \hat{\lambda}_i \hat{\lambda}_j$. The real space correlation function of these modes is derived in Appendix C.5, and the result (Eq. (C.32))

$$\langle v_i(\mathbf{x}_1) v_j(\mathbf{x}_1 + \mathbf{r}) \rangle = \sum_\ell 4\pi i^\ell \mathcal{T}_{\ell\ell}(r) P_\ell(\mu) \hat{\lambda}_i \hat{\lambda}_j, \tag{2.35}$$

where $\mathcal{T}_{\ell\ell}(r)$ is defined in Eq.(B.7), and is related to the power spectrum of the mode. Although the tensor structure of this mode is isotropic, the structure function is nevertheless anisotropic due to anisotropic power spectrum.

In the case when density perturbations are weak, the over-density correla-

tion in slow modes in low-β regime is (cf. Eq.(2.19))

$$\langle \delta\rho(\mathbf{x}_1)\delta\rho(\mathbf{r}+\mathbf{x}_1)\rangle = \int \mathrm{d}^3\mathbf{k} \mathrm{e}^{i\mathbf{k}.\mathbf{r}} k^{-11/3} (\hat{\mathbf{k}}\cdot\hat{\lambda})^2$$
$$= \frac{4\pi}{3}\int \mathrm{d}k\, k^{-5/3} j_0(kr) - \frac{8\pi}{3}\int \mathrm{d}k\, k^{-5/3} j_2(kr) P_2(\mu). \qquad (2.36)$$

Chapter 3

Intensity statistics of emission lines

3.1 Radiative transfer equation

The point-wise measurements of intensity in XYZ space, and therefore the direct informations of the statistics of magnetized turbulence, are not available with spectroscopic measurements. Instead, the measurements of intensity of emission lines are defined in PPV space (see the right-hand panel of Fig. 3.1). PP corresponds to the sky position of the observation, and V to the velocity of emitters along the LOS, which we assume to be aligned along the z-axis. Doppler shifts are affected only by the line of sight component of turbulence velocities, which to simplify our notations we denote as v.

The theory of PPV space was pioneered in LP00 and was later extended for special cases in LP04, LP06, LP08. The main expressions of the theory that we are going to use within our study are summarized in Appendix A. These expressions describe the non-linear velocity mapping of turbulence irrespective of the degree of turbulence anisotropy.

In this thesis, we are studying how intensity statistics reflects the anisotropic nature of the velocity and density fields in magnetized turbulence. The intensity

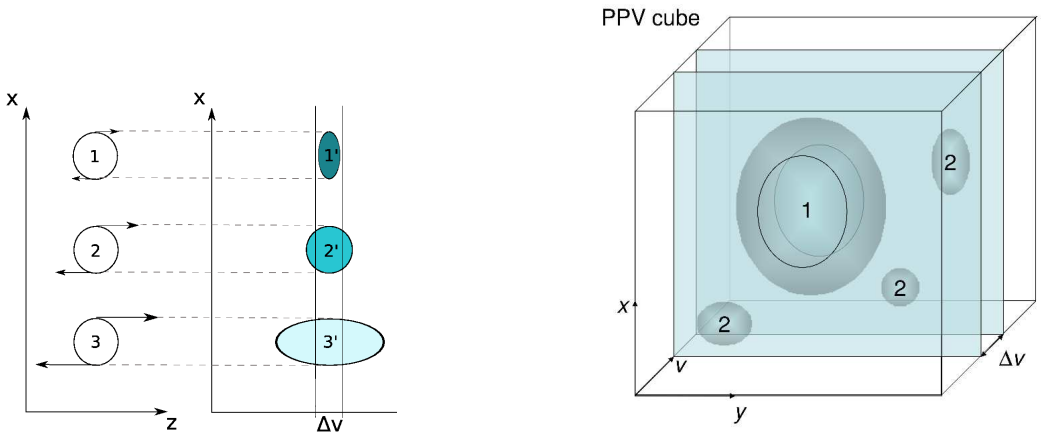

Figure 3.1: Left: an illustration of the mapping from the real space to the PPV space. In the real 'PPP' space, the three eddies have the same size, the *same density* of emitting material, but different velocities. They are being mapped to the PPV space and there they have the same PP dimensions, but a different v-size. The larger the velocity of eddies, the larger the v-extent of the eddies, which in turn implies less density of emitting atoms *over the image of the eddy*. Therefore, in terms of the intensity of fluctuations in the velocity channel Δv, the largest contribution comes from the eddy with the least velocity dispersion, i.e. eddy 1, while the eddy with the largest velocity dispersion, i.e. eddy 3, produces the faintest PPV image. Right: PPV data cube. Illustration of the concepts of the thick and thin velocity slices. The slices are thin for the PPV images of the large eddies, and thick for the images of small eddies. From Lazarian (2009).

.

from an emitting medium in PPV space is dependent on density of emitters and their velocity distribution in PPV space. For negligible dust absorption, the standard equation of radiative transfer is (Spitzer Jr, 2008)

$$\mathrm{d}I_\nu = -g_\nu I_\nu \mathrm{d}z + j_\nu \mathrm{d}z \ . \tag{3.1}$$

In the case of self-absorbing emission in spectral lines that is proportional to first power of density

$$g_\nu = \alpha\rho(z)\Phi_\nu(z) \ , \tag{3.2}$$

$$j_\nu = \epsilon\rho(z)\Phi_\nu(z) \ , \tag{3.3}$$

where ρ is the density of emitting gas, and $\Phi_\nu(z)$ is the observed frequency distribution of emitters at position z on LOS. The solution to the Eq. (3.1) takes the following form

$$I_{v_1}(\mathbf{X}) = \frac{\epsilon}{\alpha}\left[1 - \mathrm{e}^{-\alpha\rho_s(\mathbf{X},v_1)}\right] \ , \tag{3.4}$$

where ρ_s is the density of emitters in PPV space, and is given by

$$\rho_s(\mathbf{X}, v_1) = \int_0^S \mathrm{d}z\, \rho(\mathbf{x})\Phi_{v_1}(\mathbf{x}) \ . \tag{3.5}$$

In writing the above equations, we have used that fact that the Doppler-shifted frequency information can be used to deduct LOS velocity of the emitters, and hence all frequency dependence in radiative transfer equation can be equivalently designated as velocity dependence $\nu \to v$. The local LOS velocity v is given by overall motion of the volume element at a point which is sum of thermal velocity, coherent velocity v_c, and turbulent velocity u. In Eq. (3.4),

$\Phi_v(\mathbf{x})$ is the thermal distribution around the mean value given by $u(\mathbf{x})+v_c(\mathbf{x})$:

$$\Phi_v(\mathbf{x}) = \frac{1}{\sqrt{2\pi\beta}} \exp\left[-\frac{(v-u(\mathbf{x})-v_c(\mathbf{x}))^2}{2\beta}\right] , \tag{3.6}$$

where $u(\mathbf{x})$ is the LOS component of turbulent velocity and $v_c(\mathbf{x})$ is the LOS component of coherent velocity that is not part of turbulent cascade. In this thesis, we assume that $v_c(\mathbf{x})$ is small, else it has to be modelled independently.

In the case when self-absorption is negligible, i.e. $\alpha \to 0$, Eq. (3.4) reduces to

$$I_{v_1}(\mathbf{X}) = \epsilon\rho_s(\boldsymbol{X}, v_1) = \epsilon \int_0^S \mathrm{d}z\, \rho(\mathbf{x})\Phi_{v_1}(\mathbf{x}) , \tag{3.7}$$

Unless explicitly mentioned, we carry out further analysis for spectral lines with negligible self-absorption, and negligible dust absorption.

3.2 Intensity and centroid statistics

3.2.1 Intensity statistics

In this section, the framework of studying ISM turbulence using intensity maps of optically thin lines will be developed. The observed intensity correlation function $\xi_I(\mathbf{R}) \equiv \langle I(\mathbf{X}_1)I(\mathbf{X}_1+\mathbf{R})\rangle$ for a turbulent field is related to the underlying statistics of density and velocity as (LP04):

$$\xi_{\rm I}(R,\phi,\Delta v) \propto \frac{\epsilon^2\bar{\rho}^2}{2\pi} \int_{-S}^{S} \mathrm{d}z[1+\tilde{\xi}_\rho(R,\phi)]\,[D_z(\mathbf{r})+2\beta_{\rm T}]^{-1/2} \int_{-\Delta v/2}^{\Delta v/2} \mathrm{d}v \exp\left[-\frac{v^2}{2(D_z(\mathbf{r})+2\beta_{\rm T})}\right], \tag{3.8}$$

where $\mathbf{r}=\mathbf{x}_1-\mathbf{x}_2$ is the spatial separation of two turbulent points, $\mathbf{R}=\mathbf{X}_1-\mathbf{X}_2$ is their separation in two dimensional sky, ϕ is the angle that R makes with sky-projected magnetic field, D_z is the z-projection of velocity structure function, $\tilde{\xi}_\rho$ is the over-density correlation, and $\beta_{\rm T} \equiv k_B T/m$ is the thermal broadening.

Observations of intensity is done in velocity channels of width Δv, and study of dependence of statistics in Δv is the central ingredient of VCA. Note that in Eq. (3.8), the coherent velocity of the turbulent cloud is ignored.

From Eq.(3.8), one can observe that because of the presence of the factor $1 + \tilde{\xi}_\rho(R, \phi)$, the integral can be separated into two parts such that one part contains only the contribution from velocity effects, and is present even when density is uniform, whereas other part contains the contribution from density effects as well. Formally, we can write

$$\xi_{\rm I}(R, \phi, \Delta v) = \xi^v_{\rm I}(R, \phi, \Delta v) + \xi^\rho_{\rm I}(R, \phi, \Delta v), \tag{3.9}$$

where the superscripts v and ρ are to remind ourselves which effects these term comprise of. Naturally, in the absence of any density fluctuations, only the first term in the above equation survives. The usefulness of the above expression comes from the fact that at various regions of interest, one or the other term becomes unimportant, as we shall see this in more detail in this thesis.

To describe intensity statistics at small scales, it is more convenient to use the intensity structure function,

$$\mathcal{D}(R, \phi, \Delta v) = 2\left[\xi_{\rm I}(R = 0, \Delta v = 0) - \xi_{\rm I}(R, \phi, \Delta v)\right]. \tag{3.10}$$

The above two equations are the main equations that we will use for our subsequent analysis.

3.2.2 Centroid statistics

In this section we develop a framework to study ISM turbulence using velocity centroids (VC) maps. We work in PPV space to study how the VC reflect velocity spectra as well as anisotropic nature of the velocity and density statistics in magnetized turbulence. For that we first derive the VC correlation as

Table 3.1: Different types of centroids

Type of centroids	*Definition*	*Structure function*
Normalised centroid	$C_N(\mathbf{X}) = \frac{\int \mathrm{d}v_1\, v_1 I_{v1}(\mathbf{X})}{\int \mathrm{d}v_1\, I_{v1}(\mathbf{X})}$	Not used in this thesis
Unnormalised centroid	$C(\mathbf{X}) = \int \mathrm{d}v_1\, v_1 I_{v1}(\mathbf{X})$	Eq. (3.20)
Modified centroids	only structure function is defined	Eq. (5.24)

well as structure function through PPV space. The description of VC through PPV space formalism turns out to be valuable to understand the effects of self-absorption on VC.

The VC, which are intensity weighted mean velocities along V direction of PPV data cube, are defined as (see Miesch and Bally 1994)

$$C_N(\mathbf{X}) = \frac{\int \mathrm{d}v_1\, v_1 I_{v1}(\mathbf{X})}{\int \mathrm{d}v_1\, I_{v1}(\mathbf{X})}\ , \tag{3.11}$$

where I_{v1} is the spectral intensity and v_1 is the line of sight velocity. The spectral intensity in the presence of self-absorption is given by Eq. (3.4), where as for optically thin emission line, it is given by Eq. (3.7).

Due to presence of denominator term in the definition of VC in Eq. (3.11), $C_M(\mathbf{X})$ is non-linear function of I, which complicates relation between statistics of VC and intensity. To remedy this difficulty, LE03 introduced 'unnormalised' VC (UVC) defined as

$$C(\mathbf{X}) = \int \mathrm{d}v_1\, v_1 I_{v1}(\mathbf{X})\ . \tag{3.12}$$

The geometric construction of UVC is presented in right-hand side panel of Fig. 3.2.

A summary of different types of VC that appear in literatures is presented in Table 3.1. In all the subsequent sections, we carry out analysis with unnormalised VC.

We first review unnormalised VC in the case when self-absorption is negli-

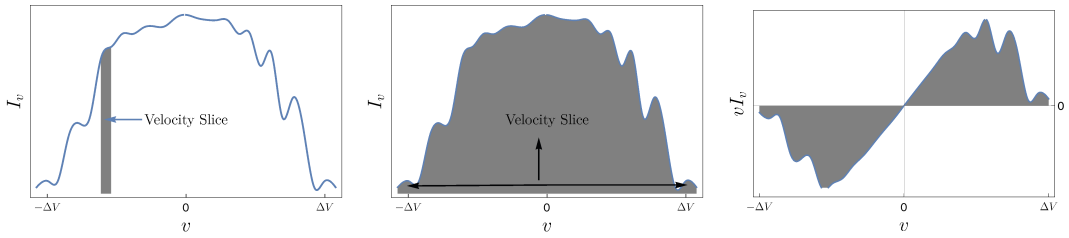

Figure 3.2: Schematic showing geometrical differences between construction of VCA and of VC. Left-hand panel: Construction of thin-slice VCA. Only channels of thin total velocity width δv needs to be used to find the intensity. Central panel: Construction of thick-slice VCA. Effectively, integration over the entire line width is carried out to find intensity. Right-hand panel: Construction of velocity VC. Velocity weighted moment of intensity is constructed and integrated over entire line width.

gible. In this case, Eq. (3.12) together with Eq. (3.7) give

$$C(\mathbf{X}) = \epsilon \int \mathrm{d}v\, v \rho_s(\mathbf{X}, v) \ . \tag{3.13}$$

The usual approach in the study of VC is to work in position-position-position space rather than PPV space. This can be achieved by writing Eq. (3.13) as

$$C(\mathbf{X}) = \epsilon \int \mathrm{d}v\, v \int \mathrm{d}z\, \rho(\mathbf{x}) \Phi(v - u(\mathbf{x})) = \epsilon \int \mathrm{d}z\, u(\mathbf{x}) \rho(\mathbf{x}) \ , \tag{3.14}$$

where $\rho(\mathbf{x})$ is the real space density and $u(\mathbf{x})$ is the z-component of the turbulent velocity.

However, in order to make a smooth connection between the optically thin case to the optically thick case, we derive VC correlation function by working in the PPV space. This is straightforwardly achieved by utilising the theory of fluctuations of PPV space density $\rho_s(\mathbf{X})$ developed in LP00 and LP04. Using Eq. (3.12), the correlation of VC can be written as

$$\begin{aligned} \xi(\mathbf{R}) = \int_{-S}^{S} \mathrm{d}z_1 \int_{-S}^{S} \mathrm{d}z_2\, \xi_\rho(\mathbf{r}) \int_{-\infty}^{\infty} \mathrm{d}v_1\, v_1 \\ \int_{-\infty}^{\infty} \mathrm{d}v_2\, v_2 \langle \Phi(v_1 - u(\mathbf{x}_1)) \Phi(v_2 - u(\mathbf{x}_2)) \rangle \ , \end{aligned} \tag{3.15}$$

where $\mathbf{R} = \mathbf{X}_1 - \mathbf{X}_2$, $\mathbf{r} \equiv (\mathbf{R}, z) = \mathbf{x}_1 - \mathbf{x}_2$ and $\xi_\rho(\mathbf{r})$ is the density correlation function. In Eq. (3.15), $\langle .. \rangle$ denotes the averaging over turbulent velocity $u(\mathbf{x})$ as a random quantity. The main assumption in writing Eq. (3.15) is that the density and velocity fields are uncorrelated. This assumption has been tested in the past papers (eg. Esquivel et al. 2007), and seems to be sufficiently accurate for subsonic turbulence with density dispersion less than the mean density of a turbulent cloud. Introducing change of variables $v_+ = (v_1 + v_2)/2$ and $v_- = (v_1 - v_2)$, and assuming that the turbulent velocity is a Gaussian random vector, Eq. (3.15) reduces to

$$\xi(\mathbf{R}) = \frac{1}{2\pi} \int_{-S}^{S} \mathrm{d}z \left(1 - \frac{|z|}{2S}\right) \int_{-\infty}^{\infty} \mathrm{d}v_- \int_{-\infty}^{\infty} \mathrm{d}v_+ \left(v_+^2 - \frac{v_-^2}{4}\right) \frac{\xi_\rho(\mathbf{r})}{\sqrt{D_z(\mathbf{r}) + 2\beta_\mathrm{T}}} \exp\left[-\frac{v_-^2}{2(D_z(\mathbf{r}) + 2\beta_\mathrm{T})}\right] \sqrt{\frac{2}{D^+(S,\mathbf{r})}} \exp\left[-\frac{v_+^2}{D^+(S,\mathbf{r})}\right] , \tag{3.16}$$

where

$$D^+(S,\mathbf{r}) \equiv \beta_\mathrm{T} + D_z(S) - D_z(\mathbf{r})/2 , \tag{3.17}$$

and $D_z(\mathbf{r})$ is the z-projected velocity structure function, $\beta_\mathrm{T} \equiv k_B T/m$ is the thermal broadening, m being the mass of atoms, T being the temperature and k_B being the Boltzmann constant. After performing the integration over v and v_+, we finally obtain

$$\xi(\mathbf{R}) = \frac{1}{2} \int_{-S}^{S} \mathrm{d}z \left(1 - \frac{|z|}{2S}\right) \xi_\rho(\mathbf{r}) (D_z(S) - D_z(\mathbf{r})) . \tag{3.18}$$

Notice that our formalism cleanly shows how thermal effects drop out in VC upon carrying out the integral in Eq. (3.16) to obtain Eq. (3.18). This shows that turbulence velocity spectrum can be recovered with VC regardless of the temperature[1], which is distinct from other techniques (e.g. VCA).

[1]For very hot plasmas, noise levels can distort VC statistics.

The VC structure function is defined as

$$\mathcal{D}(R) = \left\langle [C(\mathbf{X}_1 + \mathbf{R}) - C(\mathbf{X}_1)]^2 \right\rangle \ . \tag{3.19}$$

Utilising Eqs. (3.18) and (3.19), we obtain the VC structure function

$$\mathcal{D}(\mathbf{R}) \approx \int_{-S}^{S} \mathrm{d}z \left\{ D_z(S) \left(\xi_\rho(0,z) - \xi_\rho(\mathbf{r}) \right) + \left[\xi_\rho(\mathbf{r}) D_z(\mathbf{r}) - \xi_\rho(0,z) D_z(0,z) \right] \right\} \ . \tag{3.20}$$

With the assumption of zero correlation between density and velocity, the above result for optically thin line is identical to that obtained in LE03, where the same result was obtained by directly utilising Eq. (3.14). However, working from first principles in the PPV space, as is done in this thesis, is especially useful to deal with VC in the presence of self-absorption.

For a constant density field, with $D_z(r)$ given by Eq. (2.3), and at $R \ll S$, the VC structure function scales as

$$\mathcal{D}(R) \propto R^{1+\nu} \ . \tag{3.21}$$

We will refer to this scaling further in this thesis.

Chapter 4

Anisotropy of Intensity Statistics

4.1 Anisotropic statistics of PPV velocity slices

In the previous sections, we have defined the tools that are required for our achieving our goal, i.e. describing the anisotropy of the PPV. In this section, we develop the analytical framework for the study of anisotropic turbulence through the intensity statistics of the PPV velocity slices. The scale Δv in Eq. (3.8) is the slice thickness, and by comparing this slice thickness with the variance of velocity, we develop notion of thin and thick slice. If Δv is smaller than the velocity dispersion at the scale of study, it is a *thin* channel, whereas if Δv is much larger than the velocity dispersion, it is called a *thick* channel.

Anisotropy in intensity statistics is seen in the ϕ dependence of intensity structure function. To study this angular dependence, we will carry out a multipole expansion of the structure function in circular harmonics. Such an expansion is useful as these multipoles can be studied observationally. In particular, for an isotropic turbulence, only monopole moment survives.

4.1.1 Intensity statistics in a thin slice regime

We first study intensity fluctuations in the thin slice limit. In the case of thin velocity channel, which is the case when $\Delta v < D_z(S) + 2\beta$, utilising equations (3.8), the intensity structure function can be expressed as

$$\mathcal{D}(R,\phi) \propto \frac{2\epsilon^2}{2\pi}\int_{-S}^{S} \mathrm{d}z \left[\frac{1+\tilde{\xi}_\rho(0,z)}{\sqrt{D_z(0,z)}} - \frac{1+\tilde{\xi}_\rho(\mathbf{R},z,\phi)}{\sqrt{D_z(\mathbf{R},z,\phi)}}\right], \tag{4.1}$$

where we have ignored the thermal effects. This can be justified by taking thermal effect as a part of slice thickness (LP00). From Eq. (3.9), the above equation can be broken into pure velocity and density terms. Let us consider the pure velocity contribution which is often dominant in the case of thin velocity width. In this case, the structure function is

$$\mathcal{D}_v(R,\phi) \propto \frac{2\epsilon^2}{2\pi}\int_{-S}^{S} \mathrm{d}z \left[\frac{1}{\sqrt{D_z(0,z)}} - \frac{1}{\sqrt{D_z(\mathbf{R},z,\phi)}}\right]. \tag{4.2}$$

To extract the non-trivial ϕ dependence from the above expression, we use multipole decomposition of the structure function in circular harmonics, and write the structure function as a series of sum of multipoles

$$\mathcal{D}_v(\mathbf{R},\phi,0) = \sum_m \tilde{d}_m(R)\mathrm{e}^{\mathrm{i}m\phi}, \tag{4.3}$$

where the multipole moments $\tilde{d}_m$, in the case of constant density, are given by

$$\tilde{d}_m(R) = \frac{\bar{\rho}^2}{2\pi}\left[2\pi\delta_{m0}\int_{-S}^{S}\mathrm{d}z\frac{1}{\sqrt{D_z(0,z)}} - \int_0^{2\pi}\mathrm{d}\phi\mathrm{e}^{-im\phi}\int_{-S}^{S}\mathrm{d}z\frac{1}{\sqrt{D_z(\mathbf{R},z,\phi)}}\right]. \tag{4.4}$$

In writing the above equation, we have considered the fact that the integral of $1/\sqrt{D_z(0,z)}$ over ϕ for non-zero m vanishes.

We also introduce a parameter called degree of Isotropy which is defined as

$$\text{Isotropy Degree} = \frac{\mathcal{D}(R, \phi = 0, \Delta v)}{\mathcal{D}(R, \phi = \pi/2, \Delta v)}, \tag{4.5}$$

where $\mathcal{D}$ is the intensity structure function. This parameter is particularly useful later to make comparisons with the numerical studies that have been carried out on anisotropic turbulence. It will be later shown that the isotropy degree has an interesting dependence on the thickness of velocity slice, which will be shown to be very useful in the study of intensity anisotropy.

We now proceed to find the multipole moments of intensity structure function in the thin slice limit at constant density. The most general form of velocity structure function projected along LOS is given by equation (2.9). The coefficients A, B, C and D in this projected structure function are in general a function of μ, and can be expressed through a multipole expansion over Legendre polynomials $P_n(\mu)$ as discussed in Appendix D. Although, projected structure function in general contains sum up to infinite order in multipole expansion, to obtain analytical results, we take the terms up to second order from the infinite sum for $A_n, B_n, \ddots$ and ignore the higher order terms. This approximation is justified due to two reasons. First, these coefficients all become exceedingly small for higher orders in the region of our interest, which is small $\mathbf{r}$. Secondly, upon carrying out integral over the LOS, the effects of the higher order coefficients get diminished[1]. With this approximation, the z-projection of velocity structure function can be shown to be (c.f Eq.(2.9))

$$D_z(\mathbf{r}) = f_1 \left(1 - f_2 \cos\phi - f_3 \cos^2\phi\right), \tag{4.6}$$

where f_1, f_2 and f_3 are some other functions of r, γ, θ and are independent of ϕ. The details about f_1, f_2 and f_3 are provided in Appendix D.

[1]This was tested numerically, and this statement is good as long as the power spectrum is not highly anisotropic.

To evaluate Eq. (4.4), it is usually convenient to carry out ϕ-integral first and z-integral later. This has been done in Appendix E and F. Utilizing equations (E.4), (F.6) and (F.8) and Table D.1, we arrive at the following form of the intensity structure function

$$\mathcal{D}_v(\mathbf{R},\phi,0) \propto \sum_{m,2}^{\infty} \mathcal{W}_m (\sin\gamma)^m \mathrm{e}^{im\phi}, \tag{4.7}$$

where $\mathcal{W}_m$ is defined to be weightage function. However, we are only interested in the monopole and quadrupole coefficients. Although Eq. (E.4) has sum that extends to infinity, for most of our purposes, it is enough to just take first few terms. Therefore, for monopole we take first two terms and for quadrupole term we only take the leading-order term in the sum. Note that the factors f_1, f_2 and f_3 in Eq. (4.6) are further written in terms of other factors $q_1, q_2, \ldots$ which are dependent on mode composition of turbulence. The details of these factors are presented in Appendix D and Table D.1. Keeping this in mind, we have the monopole weightage function as

$$\begin{aligned}\mathcal{W}_0 \approx -\Bigg\{ &\sqrt{\frac{\pi}{q_1+q_2}} \left(\frac{\Gamma\left(\frac{\nu}{4}-\frac{1}{2}\right)}{\Gamma\left(\frac{\nu}{4}\right)} - \frac{q_2}{2(q_1+q_2)} \frac{\Gamma\left(\frac{\nu}{4}+\frac{1}{2}\right)}{\Gamma\left(\frac{\nu}{4}+1\right)} \right) \\ &- \frac{\sqrt{\pi}}{4q_1^{3/2}} \left(\frac{\Gamma\left(\frac{\nu}{4}+\frac{1}{2}\right)}{\Gamma\left(\frac{\nu}{4}+1\right)} - \frac{3}{4}\frac{q_2}{q_1} \frac{\Gamma\left(\frac{\nu}{4}+\frac{3}{2}\right)}{\Gamma\left(\frac{\nu}{4}+2\right)} \right) u_1 \sin^2\gamma \Bigg\} R^{1-\nu/2}. \end{aligned} \tag{4.8}$$

Similarly, the quadrupole weightage function is given by

$$\mathcal{W}_2 \approx -R^{1-\nu/2} \frac{\sqrt{\pi}}{4q_1^{3/2}} \left(\frac{\Gamma\left(\frac{\nu}{4}+\frac{1}{2}\right)}{\Gamma\left(\frac{\nu}{4}+1\right)} - \frac{3}{4}\frac{q_2}{q_1} \frac{\Gamma\left(\frac{\nu}{4}+\frac{3}{2}\right)}{\Gamma\left(\frac{\nu}{4}+2\right)} \right) u_1. \tag{4.9}$$

Eqs. (4.8) and (4.9) are only approximate and should be used with caution. In particular, equation (4.8) is good only when $(q_1+q_2) > q_2$, while equation (4.9) is good when $q_1 > q_2$. However, even in the regime where these conditions do not hold, these equations are robust enough to predict approximate numerics

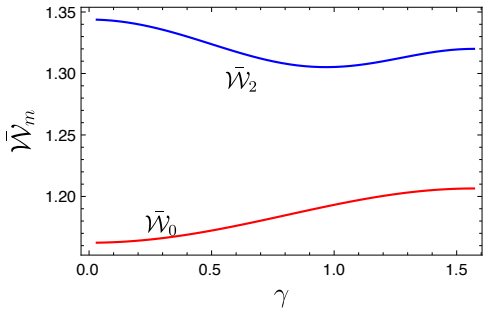

Figure 4.1: The ratio of $\mathcal{W}_m$ obtained from analytical expressions (equations 4.8 and 4.9) to the one obtained from numerical calculations for Alfvén mode at $M_{\rm A} = 0.7$. Note that the velocity structure function is truncated to the same multipole for both numerical and analytical calculations.

that are not too far from the exact result. The ratio of weightage function $\mathcal{W}_m$, obtained from equations (4.8) and (4.9), to that obtained numerically has been plotted in Fig. (4.1). As shown in the figure, the analytical results are close to the numerical results.

It is interesting to note that the isocontours of intensity structure function can be elongated towards the direction parallel to the projection of magnetic field or perpendicular to it depending on the sign of u_1. For $u_1 > 0$, the isocontours should be aligned towards the parallel direction, while for $u_1 < 0$, they should be aligned towards the perpendicular direction.

It is usually useful to obtain expressions for quadrupole-to-monopole ratio, as this is the one which gives the measure of anisotropy. In our case, we have

$$\frac{\tilde{d}_2}{\tilde{d}_0} = \frac{\mathcal{W}_2 \sin^2\gamma}{\mathcal{W}_0}. \tag{4.10}$$

It is clear from the above equation that at $\gamma = 0$, the anisotropy vanishes.

4.1.2 Intensity statistics in a thick slice regime

LP00 showed that density effects are dominant if the velocity slice is 'very thick'. In this limit, velocity effects get washed away in an optically thin

medium. In this section, we derive expressions for intensity statistics in the case of very thick velocity slice. Using the results of LP04, we have the intensity correlation

$$\xi_{\rm I}(R,\phi) \propto \int_{-S}^{S} {\rm d}z \frac{\xi_\rho(\mathbf{r})}{\sqrt{D_z(\mathbf{r})+2\beta_T}} \int_{-\infty}^{\infty} {\rm d}v \exp\left[-\frac{v^2}{2(D_z(\mathbf{r})+2\beta_T}\right], \tag{4.11}$$

which upon carrying out the integration over v gives

$$\xi_{\rm I}(R,\phi) \propto \int_{-S}^{S} {\rm d}z\, \xi_\rho(\mathbf{r}). \tag{4.12}$$

This expression clearly shows that at thick slice, all the velocity information is erased, and density effects play a primary role in intensity statistics. Eq. (4.12) allows us to obtain the intensity structure function as

$$\mathcal{D}(R,\phi) \propto \int_{-S}^{S} {\rm d}z \left[\xi_\rho(z) - \xi_\rho(\mathbf{r})\right]. \tag{4.13}$$

Using a general model of density correlation defined in Eq. (2.20) and (2.21), it can be shown that

$$\mathcal{D}(R,\phi) \propto \pm(1+c_\rho P_2(\cos\gamma)) \int_{-S}^{S} {\rm d}z \left((z^2+R^2)^{-\nu_\rho/2} - |z|^{-\nu_\rho/2}\right) \pm \frac{3}{2} c_\rho (\sin^2\gamma\cos^2\phi - \cos^2\gamma) R^2 \int_{-S}^{S} {\rm d}z (z^2+(R)^2)^{-\nu_\rho/2-1}, \tag{4.14}$$

where + sign is for steep density spectra whereas − sign is for shallow density spectra. The above expression can be evaluated analytically and yields

$$\mathcal{D}(R,\phi) \propto \pm(1+c_\rho P_2(\cos\gamma))\Bigg(R^{-\nu_\rho}\,{}_2F_1\left(\frac{1}{2},\frac{\nu_\rho}{2};\frac{3}{2};-\frac{S^2}{R^2}\right) + \frac{S^{-\nu_\rho}}{\nu_\rho-1}\Bigg) \pm \frac{3}{2}c_\rho(\sin^2\gamma\cos^2\phi-\cos^2\gamma)R^{-\nu_\rho} \,{}_2F_1\left(\frac{1}{2},\frac{\nu_\rho+2}{2};\frac{3}{2};-\frac{S^2}{R^2}\right), \tag{4.15}$$

for $-1 < \nu_\rho < 1$. Note that for $\nu_\rho < -1$, intensity correlation function should be used. We are interested in small separation asymptote, i.e. $R/S \ll 1$, given by

$$\mathcal{D}(R,\phi) \propto \pm\frac{\sqrt{\pi}\Gamma\left(\frac{\nu_\rho-1}{2}\right)}{\Gamma\left(\frac{\nu_\rho}{2}\right)}\Bigg[(1+c_\rho P_2(\cos\gamma)) + \frac{3}{2}c_\rho\frac{\nu_\rho-1}{\nu_\rho}(\sin^2\gamma\cos^2\phi-\cos^2\gamma)\Bigg]R^{1-\nu_\rho}. \tag{4.16}$$

The above equation gives some important qualitative features. First, the anisotropy vanishes at $\gamma = 0$, which is again consistent with the fact that if the magnetic field is aligned along the LOS, then the statistics reduces to the isotropic statistics. Secondly, c_ρ primarily determines the degree of anisotropy. Next, the iso-correlation contour is aligned towards the direction parallel to the sky-projected magnetic field if $c_\rho < 0$ and towards direction orthogonal to the sky-projected magnetic field if $c_\rho > 0$. It is expected that the fluctuations are elongated along the direction of magnetic field, and this would mean that for a *steep* spectrum, $c_\rho < 0$, while for a *shallow* spectrum, it can be similarly shown that $c_\rho > 0$. It has been shown that the density effects are isotropic at large sonic Mach number M_s (Kowal et al. 2007). Therefore, we expect c_ρ to approach 0 as M_s goes large. Density anisotropy depend on Alfvén Mach number M_A as well, although the dependence of anisotropy on sonic Mach number is more pronounced (Kowal et al. 2007). Therefore, c_ρ should be a function of

M_s and $M_{\rm A}$, and observational results might allow us in future to obtain good functional form of c_ρ.

4.1.3 VCA and interferometric studies

Interferometric studies provide yet another way of studying turbulence. The 2D spectra of fluctuations of intensities in velocity slice are easy to obtain as these 2D spectra can be measured by interferometers. Therefore, using interferometers one does not need to first create intensity maps, but can use the raw interferometric data. This gives a significant advantage for studying turbulence in extragalactic objects as well as for poorly resolved clouds in Milky Way. For obtaining the spectrum, just a few measurements corresponding to different baselines, i.e. for different $|\mathbf{K}|$, of an interferometer are sufficient[2].

For the anisotropy studies, one can also use raw interferometric data with missing frequencies, but it is important to sample the fluctuations for different direction of the two-dimensional vector $\mathbf{K}$. This provides more stringent requirements to the interferometric data compared to just studying of velocity and density spectra with the VCA, but still it is much easier than restoring the full spatial distribution of intensity fluctuations.

A simple estimate of the degree of anisotropy of the interferometric signal can be obtained by taking the Fourier transform of the monopole and quadrupole part of the expansion in Eq. (4.3). With this, we have the quadrupole power spectrum

$$\begin{aligned} P(\mathbf{K}) &= \sum_m P_m(K)\cos(m\phi_K) \\ &= \sum_m \int \mathrm{d}^2\mathbf{R}\,\mathrm{e}^{i\mathbf{K}.\mathbf{R}}\tilde{d}_m(R)\cos(m\phi), \end{aligned} \tag{4.17}$$

where $\cos\phi_k = \hat{\mathbf{K}}\cdot\hat{\Lambda}$ and $P_m(K)$ is the quadrupole moment in Fourier space.

[2]The procedures are also discussed in LP16 for synchrotron polarization data.

After expanding the two-dimensional plane wave as

$$\mathrm{e}^{iKR\cos\theta} = \sum_{n=-\infty}^{\infty} i^n J_n(KR)\mathrm{e}^{in\theta}, \tag{4.18}$$

where $J_n(z)$ is the Bessel function of first kind, the angular part of the integral in Eq. (4.17) gives

$$P_m(K) = \int \mathrm{d}R\, R\tilde{d}_m(R)J_m(KR). \tag{4.19}$$

The above equation provides important information that the anisotropy in real space manifests as anisotropy in Fourier space, and each multipole in real space has one-to-one correspondence with the multipoles in Fourier space.

The asymptotic form of $P_m(K)$ for large K can be obtained analytically and the result in the case of pure velocity contribution is

$$P_m(K) = \frac{2^{2-\frac{\nu}{2}}\Gamma\left(\frac{1}{4}(2m-\nu+6)\right)}{\Gamma\left(\frac{1}{4}(2m+\nu-2)\right)}\tilde{d}_m(KS)^{3-\nu/2} \tag{4.20}$$

where $\tilde{d}_m$ is the real space intensity moment after R dependence being explicitly factored out. With this the ratio of quadrupole to monopole moment is

$$\frac{\tilde{d}_{2K}}{\tilde{d}_{0K}} = -\frac{6-\nu}{2-\nu}\frac{\tilde{d}_2}{\tilde{d}_0}. \tag{4.21}$$

Note that the sign of quadrupole moment changes in Fourier space when compared to real space. Moreover, the ratio of quadrupole to monopole is enhanced by a factor of $(6-\nu)/(2-\nu)$ which for $\nu = 2/3$ is 4. Therefore, the anisotropy is much more apparent in Fourier space. This provides a unique way to study turbulence with interferometric signal as we can utilize both the isotropic part and the anisotropic parts (like quadrupole moment) to study turbulence spectra.

4.1.4 Effects of spatial and spectroscopic resolution

The effects of telescope resolution for the VCA ability to get the spectra were considered in LP04. Naturally, the finite resolution of telescopes introduced the uncertainty of the order of δK which is inversely proportional to $\delta\theta$ that characterize the resolution of telescopes. For the analysis of anisotropies in this thesis, the requirement is that we study anisotropies at the separation $\gg \delta\theta$. Anisotropies can be studied at large separations, even in the absence of good spectroscopic resolution, as the slices are effectively thin in this scale.

While the studies of velocity spectra critically depend on the thickness of velocity slices, the velocity resolution is not so critical for studies of the media magnetization. Indeed, even with the limited velocity resolution, it is possible to observe the anisotropy of fluctuations within the velocity slice. This opens ways of using instruments with limited velocity resolution to study magnetic fields.

On the other hand, in the presence of various velocity slice thicknesses, we have more statistical information that can be studied. Thin velocity slices can be used to study turbulence spectra at small separation, intermediate slices can be used for intermediate scale and thick velocity slices can be used to study spectra at large separation.

To study effects of finite resolution on intensity anisotropy, we start with some of the equations presented in LP06. The intensity measured by a telescope is $\int \mathrm{d}\mathbf{X}\, B(\mathbf{X}-\mathbf{X}_0) I(\mathbf{X}, v)$, where $B(\mathbf{X})$ is the beam of the instrument centred at $\mathbf{X} = \mathbf{X}_0$. With some analysis, the intensity structure function is given by (LP06)

$$\mathcal{D}(\mathbf{R}_0, v) \approx \int \mathrm{d}^2\mathbf{R}\, B^2(\mathbf{R}-\mathbf{R}_0)[d_s(\mathbf{R}, v) - d_s(0, v)] \ . \tag{4.22}$$

We take Gaussian beam

$$B^2(\mathbf{R}-\mathbf{R}_0) = \frac{1}{\pi\theta_0} \mathrm{e}^{-\frac{|\mathbf{R}-\mathbf{R}_0|^2}{\theta_0^2}}, \tag{4.23}$$

where θ_0 is the diagram of the instrument, relating to the resolution. θ_0 should be compared with the separation $\mathbf{R}_0$ between LOS at which the correlation is measured. If $\theta_0 \gg R_0$, the resolution is poor, and the correlation scale is not resolved. If $\theta_0 \ll R_0$, $B^2(\mathbf{R}) \to \delta(\mathbf{R} - \mathbf{R}_0)$, the and resolution is increasingly good, and we return to the VCA regime.

With decreasing resolution, it is expected that the anisotropy decreases. To understand this effect, we consider the multipole expansion of the intensity structure function. Contribution to its mth multipole moment with account for a finite resolution is

$$\begin{aligned}\mathcal{D}_m(\mathbf{R}_0, v) &= \frac{1}{\pi\theta_0}\int \mathrm{d}^2\mathbf{R}\,\mathrm{e}^{-\frac{|\mathbf{R}-\mathbf{R}_0|^2}{\theta_0^2}}\tilde{d}_m(R)\cos(m\phi) \\ &= \frac{2\mathrm{e}^{-R_0^2/\theta_0^2}}{\theta_0}\cos(m\phi_0)\int \mathrm{d}R\,R\mathrm{e}^{-R^2/\theta_0^2} I_m\left(\frac{2RR_0}{\theta_0^2}\right)\tilde{d}_m(R), \end{aligned} \tag{4.24}$$

where $I_m(x)$ is the hyperbolic Bessel function of the first kind. This factor $I_m(2RR_0/\theta_0^2)$ acts as a suppressing factor for increasing m. This has been shown in the left-hand panel of Fig. 4.2, where $I_2(x) < I_0(x)$ for all x. Therefore, we should expect quadrupole to vanish for $\theta_0 \gg R_0$. The change of isotropy with changing diagram has been illustrated in the central panel of Fig. 4.2. At $\theta_0/R_0 \sim 0$, we have a finite anisotropy which corresponds to the previous VCA results. With the increasing diagram θ_0, the statistics become more isotropic and for $\theta_0 > R_0$, information on anisotropy is completely lost. As a function of R_0 (right-hand panel), we see that practically as soon as we start measuring correlations at resolved scales $R_0 > \theta_0$, the anisotropy can be recovered.

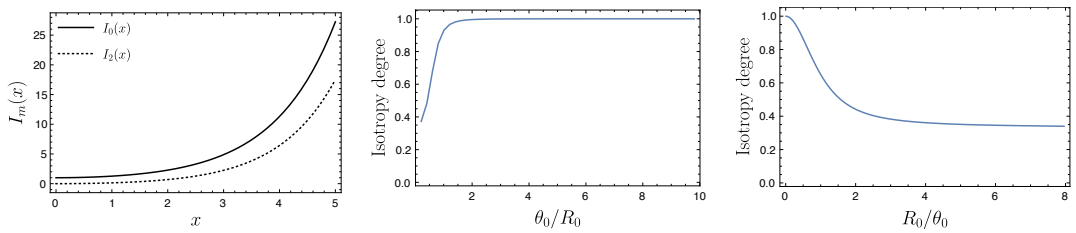

Figure 4.2: Left: hyperbolic Bessel function of the first kind. Center: isotropy degree for varying diagram θ_0 and fixed R_0. Right: same for varying lag R_0 and fixed θ_0.

4.2 Anisotropic statistics of intensity fluctuations for MHD turbulence

In previous sections, we formulated measures of intensity fluctuations for a general form of the velocity and density turbulent fields. In what follows, we use the model of compressible MHD turbulence, which comprises of Alfvén, fast and slow modes. Each mode has a specific structure of velocity, and thus gives a distinct fluctuation of intensity. However, unless amplitude of density fluctuations are small in comparison to the mean density, the anisotropic model of density for each mode is still uncertain. Thus, we still treat density with a general anisotropic model given by Eqs. (2.20) and (2.21), such that the free parameters can be established observationally.

4.2.1 Effect of Velocity Fluctuations induced by each MHD modes

First we consider pure velocity effects due to each MHD modes, treating density to be constant. The effects of fluctuating density will be considered in a subsequent section in this chapter.

Alfvén mode

For Alfvén modes, the component of velocity along the direction of the symmetry axis is zero and therefore $D = -A\mu$, and $C = A\mu^2 - B$, or equivalently $\tilde{C} = -A\mu^2 - \tilde{B}$, where $\tilde{C} \equiv C(0) - C(r)$. Therefore, the projection of structure function along the LOS is given by

$$\begin{aligned} D_z(\mathbf{r}) &= 2[\tilde{B} + \tilde{C}\cos^2\gamma - A\cos^2\theta - 2D\cos\theta\cos\gamma] \\ &= 2\left[\tilde{B}(\mathbf{r})\sin^2\gamma - A(\mathbf{r})(\mu\cos\gamma - \cos\theta)^2\right]. \end{aligned} \tag{4.25}$$

It is clear that the above structure function vanishes at $\gamma = 0$. In the limit when $\gamma \to 0$, $(\mu\cos\gamma - \cos\theta)^2 \to \sin^2\gamma\sin^2\theta\cos^2\phi$ and $\mu \to \cos\theta$ and therefore

$$D_z(\mathbf{r}) = 2\sin^2\gamma\left[\tilde{B} - A_0\cos^2\theta\cos^2\phi\right] \ , \quad \gamma \to 0 \ . \tag{4.26}$$

However, at $\gamma = 0$, all the emitters have the same LOS velocity $v_z = 0$. This implies that at this angle we are always in the thick slice regime [3]. With this observation, it is expected that the thin slice approximation will not work whenever γ is less than some critical angle γ_c. The criterion for a slice to be thick is $\Delta v > \sqrt{D_z(R)}$, where R is the separation between the two LOS. Therefore, we are in the thick slice regime whenever $\sin\gamma_c \lesssim \Delta v/(2\tilde{B})$. However, this only applies if the turbulent motions consist of only Alfvén modes. This situation is nevertheless quite rare because slow modes are also of solenoidal type and usually come along with Alfvén modes. Since slow modes have non-vanishing structure function at $\gamma = 0$, thin slice approximation would still be valid if we consider the contribution of both slow and Alfvén modes, as at small γ velocity structure function is dominated by slow modes. In a thin slice regime,

[3] In a thick slice regime, the intensity structure has a divergence of S^2, where S is the size of an emitting region. However, in a thin slice regime, the divergence is S. The fact that $1/\sin\gamma$ introduces an additional divergence is clear to explain that at $\gamma \sim 0$, thin slice approximation does not work.

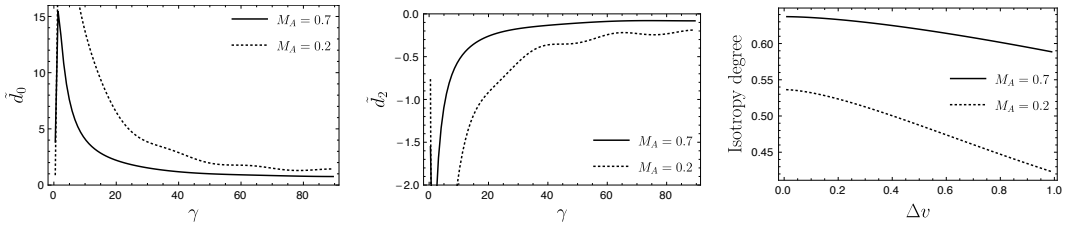

Figure 4.3: Alfvén mode. From left to right: monopole, quadrupole and isotropy degree. Monopole and quadrupole are as a function of angle between LOS and magnetic field, γ. Isotropy degree as a function of Δv is at $\gamma = \pi/2$. From top to bottom: top is at $M_{\rm A} = 0.4$, bottom at $M_{\rm A} = 0.7$

calculating monopole and quadrupole terms primarily requires the knowledge of q_1, q_2, q_3 and u_1 (cf. equations 4.8 and 4.9), which for the Alfvén modes are

$$q_1 = \left(2\tilde{B}_0 + B_2\right)\sin^2\gamma, \qquad u_1 = -2A_0\cos^2\gamma - 3B_2\sin^2\gamma$$
$$q_2 = -\left(3B_2\cos^2\gamma + 2A_0\sin^2\gamma\right)\sin^2\gamma, \qquad q_3 = 0. \tag{4.27}$$

Fig. 4.3 shows the monopole and quadrupole contributions as well as isotropy degree of intensity correlation from Alfvén modes. We highlight several important properties. First, both monopole and quadrupole components are decreasing with the increase in Alfvén Mach number, $M_{\rm A}$. Secondly, the anisotropic feature decreases with the increase in Alfvén Mach number, which is expected as higher Alfvén Mach number corresponds to higher isotropy. Moreover, both monopole and quadrupole are insensitive to γ for $\gamma \gtrsim \pi/4$, which can be a useful feature to determine Alfvén Mach number $M_{\rm A}$. In addition to that, it is clear from the figure that isotropy degree for Alfvén mode is less than 1. This implies that iso-correlation contours are elongated along the direction of sky projection of mean magnetic field. For Alfvén modes, this corresponds to the spectral suppression towards the direction parallel to the projected field. This effect is due to the structure of power spectrum of Alfvén modes. If this power spectrum was isotropic, the isocontours of this mode would be elongated along the direction orthogonal to the sky projection of mean-magnetic field (see

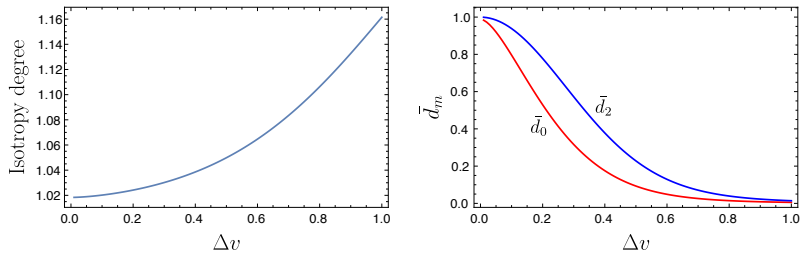

Figure 4.4: Alfvén mode. Left: The degree of anisotropy assuming an isotropic power spectrum $\mathcal{A}(k, \mu_k)$ (cf. Eq. 2.26). The observed anisotropy in this case comes purely from the anisotropic tensor structure (cf. Eq 2.25). Right: quadrupole and monopole at $M_{\rm A} = 0.7$. Both are normalised by their highest value.

the left-hand panel of Fig. 4.4). Note that both the monopole and quadrupole are increasing with the decrease in γ, which might look counter-intuitive. This increase is because of the fact that the structure function $D_z \propto \sin^2\gamma$, and therefore, the intensity structure function $\mathcal{D} \propto \sin^{-1}\gamma$ which reflects that more and more emitters are occupying the same velocity channel $v_z = 0$.

By looking at the left-hand panel of Fig. [4.4], one can observe the decrease of isotropy degree for increasing slice thickness [4], Δv. This decrease can be understood in the following sense: at small slice thickness, all emitters have similar LOS velocities and anisotropies are suppressed. But with the increase in slice thickness, the correlations of velocity are better sampled, thus increasing the anisotropy. The change of anisotropy with slice thickness is an important result of this thesis. This can be a useful tool in the study of MHD turbulence. It is however important to note that although the anisotropy increases with increasing Δv, the quadrupole and monopole individually approach to zero with increasing Δv. This is illustrated in the right-hand panel of Fig. 4.4, which clearly shows that both the monopole and quadrupole are clearly approaching zero as Δv approaches unity.

[4]Whenever we talk about slice thickness Δv, unless explicitly mentioned otherwise, we talk about slice thickness normalized by velocity dispersion.

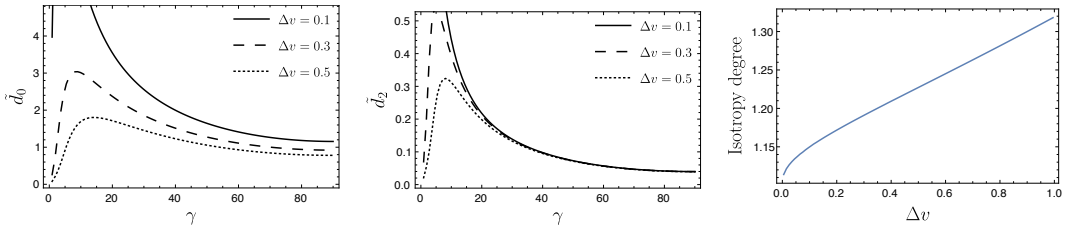

Figure 4.5: Fast mode low-β. From left to right, monopole and quadrupole and degree of isotropy. The curves in left-hand and central panels represent from top to bottom: $\Delta v = 0.1, \Delta v = 0.3$ and $\Delta v = 0.5$. The isotropy degree is at $\gamma = \pi/2$. All angles are in degrees.

Fast mode

Fast modes in high-β plasma correspond to sound waves, which are isotropic (see GS95; Cho and Lazarian 2003) .

Fast modes in low-β plasma have anisotropy in-built in the tensor structure, although their power spectrum is isotropic. For fast modes in low-β regime, the component of velocity along the direction of symmetry axis is zero, and therefore, the projection of structure function along the LOS takes the same form as that for the Alfvén mode,

$$D_z(\mathbf{r}) = 2\left[\tilde{B}(\mathbf{r})\sin^2\gamma - A(\mathbf{r})(\mu\cos\gamma - \cos\theta)^2\right]. \tag{4.28}$$

The above structure function also vanishes at $\gamma = 0$; therefore, the discussion about thin and thick slice applies to this mode as well. To find monopole and quadrupole terms, the coefficients q_1, q_2, q_3 and u_1 for this mode are given by equation (4.27).

Fig. 4.5 shows monopole, quadrupole and degree of anisotropy of low-β fast modes. Of particularly interesting pattern is the degree of isotropy which is greater than 1, unlike Alfvén modes which had this isotropy degree less than 1. This clearly implies that intensity structure iso-contours of fast modes are elongated along the direction perpendicular to magnetic field projection in the 2-D plane. This in fact validates our previous assertion that for an isotropic

power spectrum, the iso-contours should be elongated towards the direction perpendicular to sky-projected magnetic field. It is also interesting to note that even at $\gamma = \pi/2$ (which is the most anisotropic case), these modes are not so anisotropic. Therefore, observation of strong anisotropy signal could allow us to infer that fast modes are possibly important (this cannot totally eliminate fast modes, because a mixture of fast and Alfvén modes can, for example, produce strong anisotropy as long as fast modes are subdominant). Fig. [4.5] shows while monopole decreases rapidly with increasing slice thickness, the quadrupole is relatively less affected with the changing slice thickness; therefore, this increases the quadrupole-to-monopole ratio with increasing slice thickness.

Slow mode

Slow modes are anisotropic in both high and low-β. The detailed mode structure of this mode is studied in Appendix C.4. The structure function of low β slow mode is given is

$$D_z(\mathbf{r}) = 2(C(0) - C(\mathbf{r}))\cos^2\gamma. \tag{4.29}$$

Analytical calculation of the monopole and quadrupole contribution to the intensity structure function requires knowledge of various parameters as shown in equations (4.8) and (4.9), and these parameters are summarized in Table D.1.

Fig. 4.6 shows that slow modes in low β are highly anisotropic at low Alfvén Mach number $M_{\rm A}$. However, they become more isotropic at large $M_{\rm A}$, which shows that the observed anisotropy of intensity fluctuations from these modes is primarily due to the anisotropy in power spectrum. The anisotropy is pronounced for $\gamma \gtrsim \pi/4$. Moreover, the iso-correlation contours in this limit are always elongated towards the direction of sky-projected magnetic field, which is similar to the Alfvén mode. Comparing Figs. 4.3 and 4.6], it is easy to see

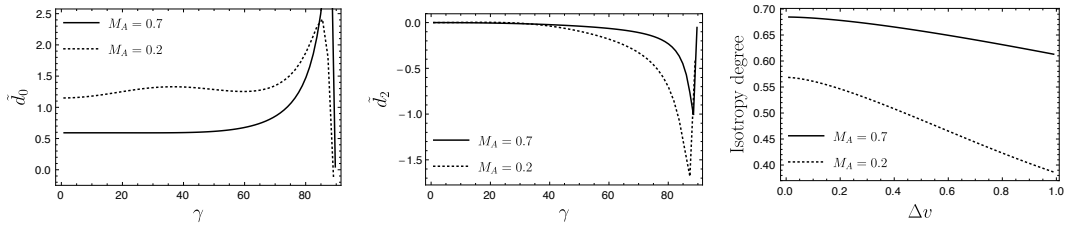

Figure 4.6: Slow mode low-β. From left to right, monopole and quadrupole and degree of isotropy at $M_{\rm A} = 0.2$ and 0.7, at $\Delta v = 0.1$. The isotropy degree is calculated at $\gamma = \pi/3$.

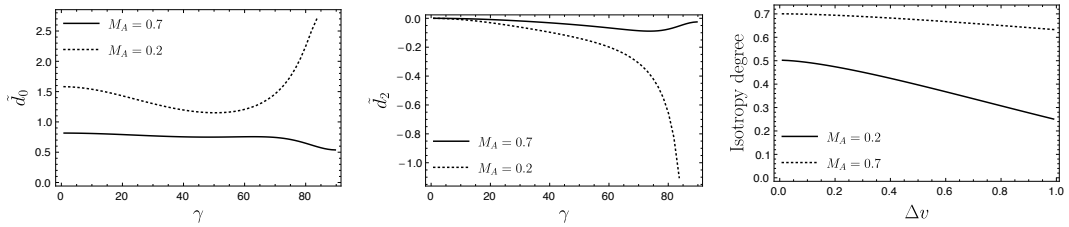

Figure 4.7: Slow Mode high β. Monopole and quadrupole and degree of isotropy for slow mode at high β. Left-hand and central panels are at $\Delta v = 0.1$. The isotropy degree is calculated at $\gamma = \pi/3$.

that in the regime $\gamma \gtrsim \pi/3$, slow modes in low β are more anisotropic than Alfvén modes for same $M_{\rm A}$.

Slow modes in high β regime show more interesting properties as shown in Fig. 4.7. The iso-correlation contours of this mode are aligned towards the direction parallel to the sky-projected magnetic field. The anisotropy comes from the anisotropy in-built in the tensor structure of this mode as well as from the power spectrum (cf. equation 2.26) of this mode. Similar to Alfvén mode, the iso-correlation contours of this mode are aligned towards the direction perpendicular to the sky-projected magnetic field.

However, our method of analysing the anisotropy by truncating the series of structure function (cf. Sec. 4.1.1) does not work well for very small $M_{\rm A}$. One reason is that the power spectrum in the regime of small $M_{\rm A}$ becomes more or less like $\delta(\hat{k}.\hat{\lambda})$, and therefore all $\mathcal{A}_n$ are important. Note that at small $M_{\rm A}$, the intensity structure function, and hence the anisotropy, of high β and low β

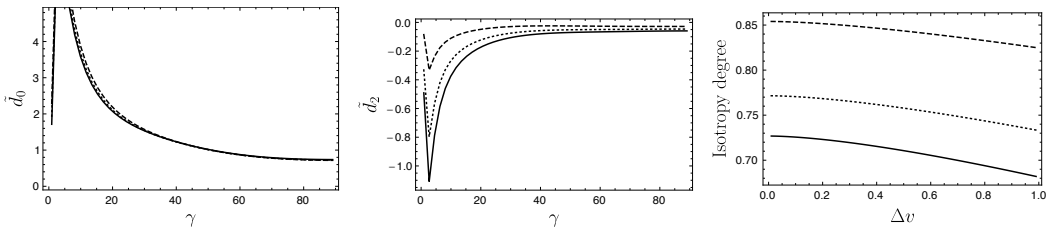

Figure 4.8: Alfvén + fast modes at low-β at $M_{\rm A} = 0.7$. Left and centre: monopole and quadrupole for various percentage of mixture. Right: isotropy degree at $\gamma = \pi/2$. The solid curve is for 95% Alfvén and 5% fast, dotted curve is for 90% Alvén and 10% fast and the dashed curve is for 80% Alvén and 20% fast.

slow modes should behave in a similar way. This is because the power spectrum (cf. equation 2.26) of high β slow mode behaves like $\delta(\hat{k} \cdot \hat{\lambda})$ at low $M_{\rm A}$, and therefore, the tensor structure of slow modes at high β (cf. equation 2.34) should reduce to the same form as that of low β slow modes, i.e. $D_z(\mathbf{r}) \propto \hat{\lambda}_i \hat{\lambda}_j$ for both modes.

Mixture of Different Modes

In this section, we show effects of mixing of modes in the isotropy degree. Mixing effects are interesting as real world MHD turbulences have different modes and our observations are the result of the combined effects of these modes.

We consider the mixture of Alfvén modes and fast modes, as well as mixture of Alfvén and slow modes. Fig. 4.8 shows that the mixture of Alfvén and fast mode in low-β increases the isotropy (cf. Fig. 4.3) when compared with pure Alfvén isotropy. This effect is caused by two factors: first, fast modes are less anisotropic than Alfvén and therefore, we expect their combination to be more isotropic than Alfvén alone. More important is the second factor: the quadrupole anisotropies of fast (in low-β) and Alfvén modes are opposite in sign. This means the anisotropy effects of the two modes act against each other. Therefore, even a small percentage of fast modes in the mixture can

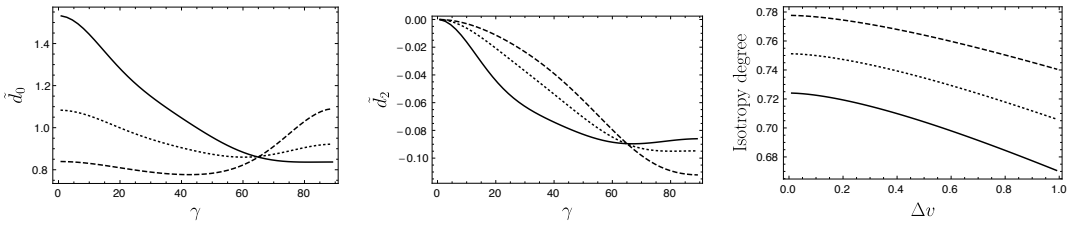

Figure 4.9: Alvén + low-β slow modes at $M_{\rm A} = 0.7$. Left and center: monopole and quadrupole for various percentage of mixture. Right: isotropy degree at $\gamma = \pi/4$. The solid curve is for 85% Alfvén and 15% slow, dotted curve is for 70% Alvén and 30% slow and the dashed curve is for 50% Alvén and 50% slow.

cause a significant difference in the anisotropy level. This has been confirmed in the left-hand and central panels of Fig. 4.8, which shows that while the monopole is relatively unaffected by the composition of mixture, the quadrupole is significantly affected with larger composition of fast modes. Note that we usually expect fast mode to be marginal in the mixture. Fast modes in high β, however, are *isotropic*. Therefore, we again expect the mixture of high-β fast and Alfvén mode to be more isotropic than Alfvén alone. However, unlike low-β fast mode , this mode at high-β does not have any quadrupole anisotropy to act against the Alfvén anisotropy. Therefore, the mixture of Alfvén and high β fast mode should be more anisotropic than the mixture of Afvén and low-β fast mode.

Another interesting mix is Alvén and slow modes in low-β plasma. We have shown that both of these modes have negative quadrupole moment. Moreover, these modes are different domains of dominance. At $\gamma \sim 0$, slow modes dominate while at $\gamma \sim \pi/2$, Alfvén modes dominate. Therefore, we expect the anisotropy level of their mixture to be not too different from the anisotropy level of each individual mode in the region of their dominance. This is shown in Fig. [4.9]. Note that in that figure, changing percentage of composition has relatively unaffected the level of anisotropy. This result shows that the anisotropy effects come primarily from the power spectra rather than the exact local structure of the spectral tensor (LP12).

It is important to note that for the case of mix between Alfvén and slow mode in low β, the anisotropy level is unaffected at $\gamma \sim \pi/2$ when compared with Alfvén mode. This is because of the fact that for low-β slow mode, the motions are along the direction of magnetic field, and therefore these motions should not affect the statistics in the direction perpendicular to them. Similarly, at smaller γ, the mix of Alfvén and low-β slow mode should produce anisotropy level similar to that of the slow mode alone. This effect is again primarily because of the anisotropy from power spectra.

4.2.2 Comparison with Esquivel et al. (2015)

One of the most interesting and important findings of our study is the decrease of isotropy degree with increasing slice thickness. This matches exactly with the findings of Esquivel et al. (2015). We compare our result with their results. In their study, for $M_{\rm A} = 0.7$ and $M_S = 2.2$, most of the contribution comes from Alfvén mode. Comparing our results for pure Alfvén effects and their result at constant density should be reasonable. In our case, at $M_{\rm A} = 0.7$, isotropy degree at thin slice regime is ~ 0.65, while their result shows an isotropy degree of ~ 0.6, which is close to our result. At $M_{\rm A} = 0.4$, however, our result shows an isotropy of 0.59, while they predicted much less isotropy degree of ~ 0.3. However, the overall trend of decreasing isotropy with increasing slice thickness matches well with our results.

4.2.3 Study of Density Effects

Besides velocity, density statistics also provide important contribution to intensity statistics. In LP00, the issue of separating density contribution from velocity contribution to the intensity statistics was addressed. For steep spectra, it was mentioned in LP04 that density effects are important at large lag R and velocity effects are important at small lags, but this was invalidated in

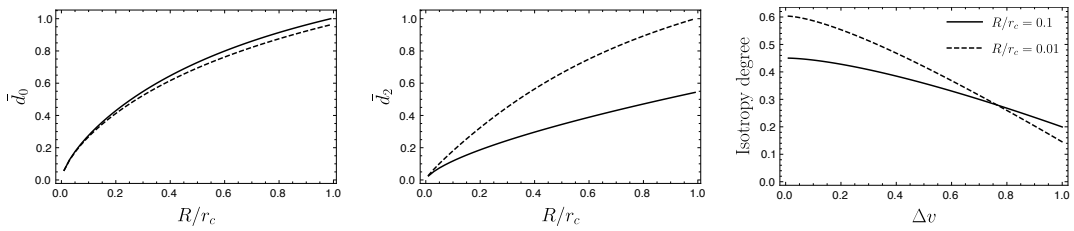

Figure 4.10: Steep density: normalized monopole (left) and normalized quadrupole (centre) for Alfvén mode at $\gamma = \pi/2$ and $c_\rho = -0.6$. The solid curve is for pure velocity contribution while the dotted curve is with steep density of Kolmogorov index. Right: Isotropy degree as a function of velocity slice thickness Δv for various R/r_c, all the parameters are the same as in the left-hand and central panels.

LP06, where it was clarified that velocity statistics are dominant in thin slice regime no matter what the scale R is. In the case of *shallow* spectra, however, density effects are important even in the thin velocity slice regime. With this, it is natural to expect that for steep spectra, anisotropy in intensity statistics should be primarily dominated by velocity effects in the thin slice regime, while for shallow spectra, anisotropy is affected by density effects as well in this regime. In the thick slice regime, only density effects are important.

We tested the effects of density anisotropy at different scales for both steep and shallow spectra. Fig. 4.10 shows some of the key features shown by density effects. Both quadrupole and monopole for the combination of velocity and density effects are similar to velocity effects alone at $R < r_c$ for a steep spectrum. This is consistent with the fact that for steep density spectra, the intensity correlation function is dominated by velocity effects at $R < r_c$. Interestingly, the quadrupole moment is affected by density effects, while monopole remains relatively unaffected. The relative importance of density effects in quadrupole moment depends on the degree of density anisotropy, c_ρ. For, sufficiently small c_ρ, we can not see any significant deviation from the pure velocity contributions. Therefore, studying monopole moment at small R should give us information on velocity statistics, while quadrupole moment will give infor-

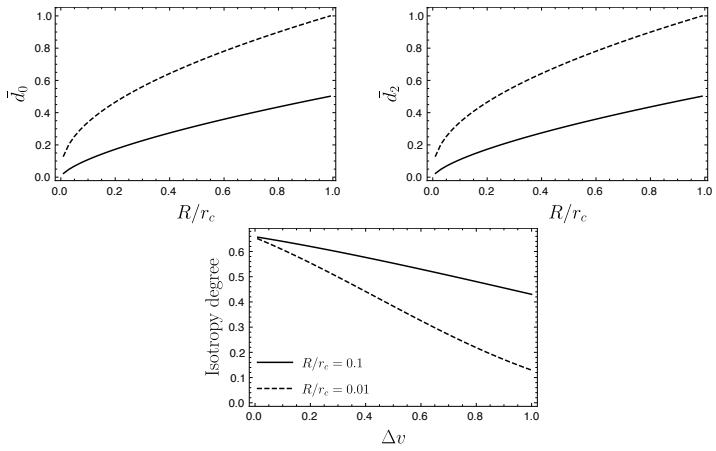

Figure 4.11: Shallow density: normalized monopole (left) and normalized quadrupole (right) for Alfvén mode at $\gamma = \pi/2$ and $c_\rho = 0.3$. The solid curve is for pure velocity contribution while the dotted curve is for shallow density of index $\nu_\rho = 1/3$. Right: Isotropy degree as a function of velocity slice thickness Δv for various R/r_c, all the parameters are the same as in the left and central panels.

mation about the presence of density effects. Note that at thick velocity slice, the intensity statistics is dominated by density effects alone.

If the density spectrum is shallow, the density effects become important at small scales. Therefore, we expect significant deviation from pure velocity effects in the case of shallow density spectrum. This is confirmed from Fig. [4.11], as the degree of isotropy changes significantly from the pure velocity effects.

4.2.4 Effects of Self-Absorption

In the previous sections, we studied anisotropy of channel maps in optically thin medium. However, knowledge of absorption effects can be important to understand the intensity statistics in various interstellar environments, for instance in molecular clouds. The effects of absorption in the intensity statistics were studied in LP04. Their study suggests that power-law behaviour of intensity statistics is distorted in the presence of absorption, and the velocity effects

are more prominent in this case.

In this section, we make use of the results of LP04 to study the effect of absorption in the degree of isotropy (cf. equation 4.5). In the presence of absorption, the intensity structure function is given by (LP04)

$$\mathcal{D}(\mathbf{R},\phi,\Delta v) \propto \int_{-\Delta v}^{\Delta v} \mathrm{d}v\, \tilde{W}(v) \mathrm{e}^{-\frac{\alpha^2}{2}\tilde{d}_s(0,v)} \left[d_s(\mathbf{R},v) - d_s(0,v)\right], \tag{4.30}$$

where $\tilde{W}(v)$ is the window which defines how integration over velocity is carried out, α is the absorption coefficient, and is zero in the case when absorption effect is absent. The most important feature shown by the above equation is the presence of an exponential factor. Due to the presence of this factor, velocity effects do not get washed out even if we enter thick slice regime, unlike the optically thin case when this factor was absent. Analysis presented in LP04 shows that in the case of Alfvén mode (which has a power law index 2/3),

$$\tilde{d}_s(0,v) \propto -v^2 \log v, \tag{4.31}$$

which is valid for small argument v. With this, for Alfvén modes Eq. (4.30) can be written as

$$\mathcal{D}(\mathbf{R},\phi) \propto \int \mathrm{d}v\, \tilde{W}(v) \mathrm{e}^{\frac{\alpha_{\mathrm{eff}}^2}{2} v^2 \log v} \left[d_s(\mathbf{R},v) - d_s(0,v)\right], \tag{4.32}$$

where α_{eff} is the effective absorption constant, which takes into account the proportionality constant of equation (4.31).

To study the effects of absorption on the anisotropy of channel maps, we performed numerical evaluation for the degree of anisotropy as a function of velocity width which results are shown in Fig. 4.12. These plots show that with absorption effect included, the intensity statistics become more isotropic. Fig. [4.12] shows that the deviation of isotropy degree of optically thick case from optically thin case occurs at a critical velocity thickness Δv_c roughly

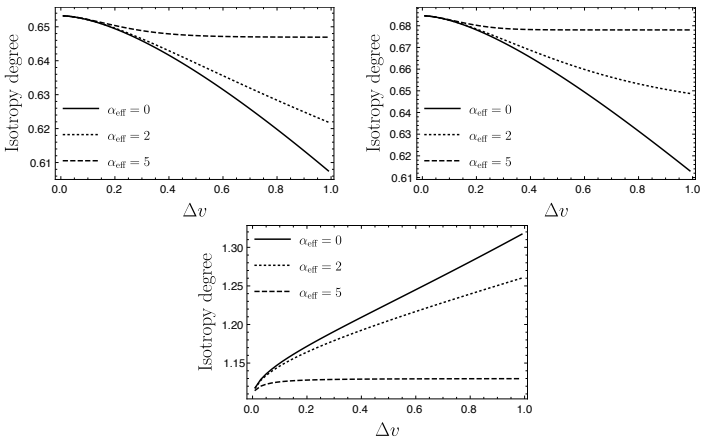

Figure 4.12: From left to right: isotropy degree for Alfvén (at $M_{\rm A} = 0.7$, $\gamma = \pi/2$), slow (low β at $M_{\rm A} = 0.7$, $\gamma = \pi/3$) and fast (low β at $\gamma = \pi/2$) in the presence of different degrees of absorptions.

given by the relation $-\alpha_{\rm eff}^2(\Delta v_c)^2 \log(\Delta v_c) = \alpha^2 d_s(0, v) \sim 1$, which in the case of $\alpha_{\rm eff} = 5$ gives $\Delta v_c \sim 0.1$, consistent with Fig. [4.12]. This is the cut-off beyond which non-linear effects become important while studying the effects of absorption (LP04). Therefore, this implies that although absorption affects the intensity statistics, the degree of isotropy however remains unaffected as long as we are in a regime where absorption is moderate.

In the regime where absorption is strong, the degree of isotropy decreases less rapidly in comparison to the case where absorption is absent. This can be understood in the following way: with stronger absorption effects, the thin slice statistics hold for larger range of velocity width and therefore, the degree of isotropy tends to flatten. This is shown by Fig. [4.12], where the flattening of this curve is shown in a gradual manner as we increase the absorption coefficient for $\alpha_{\rm eff} = 0$ to 5.

The fact that degree of isotropy for optically thick medium is similar to the degree of isotropy for the optically thin medium in the case when absorption is strong has important consequences that need to be addressed. LP04 showed that for optically thick case, at some intermediate scale R, a new asymptotic regime is seen. In this regime, the intensity statistics get independent of the

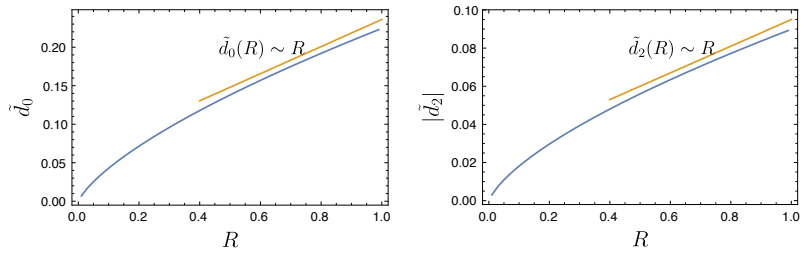

Figure 4.13: From left to right: monopole and quadrupole as a function of R for slow modes at low β at $\alpha_{\rm eff} = 5$ at $M_{\rm A} = 0.4$ and $\gamma = \pi/3$ and $\Delta v = 1$. Only pure velocity contribution is considered.

spectrum of the underlying velocity and density field by exhibiting a scaling $\sim R$. This can also be seen in Fig. 4.13, where at large R, the scalings for both monopole and quadrupole terms of the intensity structure function vary like $\sim R$. However, what is important is that even though the new intermediate asymptote is established, the imprint of anisotropy is left, which implies that some valuable information about the underlying turbulent field is still left in this regime. In fact, as we discussed earlier, the isotropy degree at this intermediate regime is still around the same as the isotropy degree in the case of thin slice. Therefore, isotropy degree can be an important tool to analyse turbulence in optically thick medium.

We analyse the relative importance of velocity and density anisotropy when both velocity and density effects are important. In the absence of absorption, LP00 showed that at small scales, velocity effects are important for thin channel thickness, while density effects become important for thick channels. Naturally, we expect anisotropy to be dominated by velocity effects for thin channels and by density effects for thick channel. Interestingly, in the presence of absorption, this is not true any more. Looking at Fig. 4.14, we see that in the presence of absorption, the degree of anisotropy is almost the same for both thin and thick channels even when the density effects are present. Note that we have considered a strong anisotropy $c_\rho = -0.6$ for density, and even this anisotropy does not affect much of the isotropy degree in the case of thick slice $\Delta v = 1$.

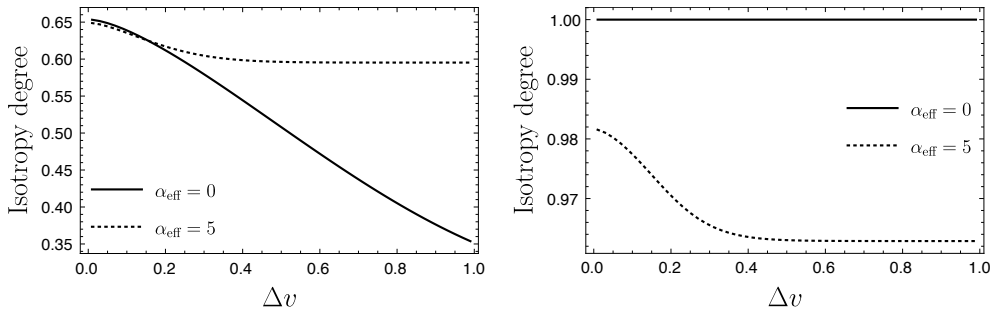

Figure 4.14: Left: isotropy degree for the combination of Alfvén modes with steep density of Kolmogorov index $\nu_\rho = -2/3$ and $c_\rho = -0.6$ at $R = 0.1$, $r_c = 10$, $M_{\rm A} = 0.7$ and $\gamma = \pi/2$. Right: isotropy degree for the anisotropic density field but isotropic velocity field for the same spectral index as the left figure. LOS angle $\gamma = \pi/2$, but all other parameters are also the same as in left-hand panel. In both panels, the solid curve is in the absence of the absorption while the dotted one is in the presence of absorption at $\alpha_{\rm eff} = 0.5$.

Therefore, what we can say is that in the presence of absorption, the anisotropy due to velocity effects is important at small scales even for the thick slice thickness where spectral resolution is absent.

In the case of isotropic velocity field and anisotropic density field, our previous discussion applies again for both shallow and steep density spectra. Due to the presence of strong absorption, the window $\mathrm{e}^{-\alpha^2 \tilde{d}_s(0,v)/2}$ in Eq. (4.30) suppresses any non-zero v and therefore in the case of strong absorption, it effectively acts like a delta function $\delta(v)$. This explains why even in the optically thick regime $\Delta v = 1$, we still have the anisotropy similar to optically thin regime.

Chapter 5

Centroid anisotropy

5.1 General formalism

In this section, the study of VC will be carried out keeping in mind that the ISM is magnetized and therefore there exists a preferred direction, which in the global frame of reference is the direction of the mean magnetic field. Due to the presence of this preferred direction, turbulence is anisotropic; to be more precise, axisymmetric. This anisotropy is built in the general tensors representing velocity, density and magnetic field correlations. The study of magnetic correlation was carried out in LP12 , and the study of velocity correlation and its application to study intensity anisotropies was carried out in Chapter 4. In this chapter, we present another way of studying anisotropies, which is through the study of anisotropy of VC correlation. The main focus of this section is to develop a general formalism to study VC anisotropy for *constant* density field.

The velocity correlation in Fourier space $\langle v_i(\mathbf{k}) v_j^*(\mathbf{k}')\rangle$ is given by Eq. (2.11), and its representation in the real space $\langle v_i(\mathbf{x}_1) v_j(\mathbf{x}_1+\mathbf{r})\rangle$ is given by Eq. (2.12). Since the VC structure function in the case of constant density for an optically thin medium is given by (cf. Eq. (3.20))

$$\mathcal{D}(R) \propto \int \mathrm{d}z (D_z(R,z) - D_z(0,z)) \ , \tag{5.1}$$

one needs to evaluate integral of the type $\int \mathrm{d}z\langle v_i v_j\rangle$ in order to evaluate the above integral. This can effectively be obtained by noting that the integration over the entire line of sight is equivalent to setting $k_z = 0$ in the spectral domain (LP12) . Therefore, we can use Eq. (2.12) to obtain

$$\int \mathrm{d}z\langle v_i v_j\rangle = \frac{1}{(2\pi)^2}\int \mathrm{d}^2\mathbf{K}\,\mathrm{e}^{\mathrm{i}\mathbf{K}\cdot\mathbf{R}}\mathcal{A}(K,\hat{\mathbf{K}}\cdot\hat{\Lambda})\left(\hat{\xi}_{\mathbf{K}}\otimes\hat{\xi}^*_{\mathbf{K}}\right)_{ij} \ . \tag{5.2}$$

We use the plane wave expansion

$$\mathrm{e}^{\mathrm{i}\mathbf{K}\cdot\mathbf{R}} = \mathrm{e}^{\mathrm{i}KR\cos\zeta_R} = \sum_{n=-\infty}^{\infty}\mathrm{i}^n J_n(KR)\mathrm{e}^{\mathrm{i}n\zeta_R} \ , \tag{5.3}$$

where $\cos\zeta_R = \hat{\mathbf{K}}\cdot\hat{\mathbf{R}}$. Similarly, decomposing the two dimensional power spectra into series of harmonics

$$\mathcal{A}(K,\hat{\mathbf{K}}\cdot\hat{\Lambda}) = \sum_{p=-\infty}^{\infty}K^{-3-\nu}\hat{\mathcal{A}}_p\mathrm{e}^{\mathrm{i}p\zeta_\Lambda} \ , \tag{5.4}$$

where $\cos\zeta_\Lambda = \hat{\mathbf{K}}\cdot\hat{\mathbf{\Lambda}}$, we obtain

$$\begin{aligned}\int \mathrm{d}z\langle v_i v_j\rangle = \frac{1}{(2\pi)^2}\int \mathrm{d}\mathbf{K}\,K^{-2-\nu}\sum_{n=-\infty}^{\infty}\mathrm{i}^n\mathrm{e}^{\mathrm{i}n\phi}J_n(KR)\\ \sum_{p=-\infty}^{\infty}\hat{\mathcal{A}}_p\mathrm{e}^{-\mathrm{i}(n-p)\psi}\left(\hat{\xi}_{\mathbf{K}}\otimes\hat{\xi}^*_{\mathbf{K}}\right)_{ij} \ ,\end{aligned} \tag{5.5}$$

where $\cos\psi = \hat{\mathbf{K}}\cdot\hat{\mathbf{\Lambda}}$. Due to the axisymmetric nature of the turbulence, only even p is allowed in Eq. (5.4). With this, we finally obtain the following form of VC structure function

$$\begin{aligned}\mathcal{D}(\mathbf{R}) = \frac{1}{(2\pi)^2}\int \mathrm{d}\mathbf{K}\,K^{-2-\nu}\sum_{n=-\infty}^{\infty}\mathrm{i}^n\mathrm{e}^{\mathrm{i}n\phi}(J_n(0)\delta_{n0}\\ -J_n(KR))\sum_{p=-\infty}^{\infty}\hat{\mathcal{A}}_p\mathrm{e}^{-\mathrm{i}(n-p)\psi}\left(\hat{\xi}_{\mathbf{K}}\otimes\hat{\xi}^*_{\mathbf{K}}\right)_{zz} \ ,\end{aligned} \tag{5.6}$$

where n is even due to the fact that p is even. To study anisotropy of the structure function, it is convenient to expand the structure function in series of two dimensional circular harmonics

$$\mathcal{D}(R,\phi) = \sum_{n=-\infty}^{\infty} \mathcal{D}_n(R) \mathrm{e}^{\mathrm{i}n\phi} \ , \tag{5.7}$$

where $\mathcal{D}_n(R)$ is the multipole moment of the VC structure function given by (cf. Eq. (5.6))

$$\mathcal{D}_n(R) = C_n(\nu) \sum_{p=-\infty}^{\infty} \hat{\mathcal{A}}_p \mathcal{W}_{n-p} R^{1+\nu} \ , \tag{5.8}$$

and $\mathcal{W}_p$ is the spectral weight function, which is the integral of the tensor structure of a specific mode over the two dimensional angle ψ, given by

$$\mathcal{W}_p = \frac{1}{2\pi} \int_0^{2\pi} \mathrm{d}\psi \, \mathrm{e}^{-\mathrm{i}p\psi} \left(\hat{\xi}_{\mathbf{K}} \otimes \hat{\xi}^*_{\mathbf{K}} \right)_{zz} \ , \tag{5.9}$$

and

$$C_n(\nu) = \mathrm{i}^n \int \mathrm{d}K \, K^{-2-\nu} (J_n(0)\delta_{n0} - J_n(K)) = -\frac{\mathrm{i}^n \Gamma\left[\frac{1}{2}(|n| - \nu - 1)\right]}{2^{2+\nu}\Gamma\left[\frac{1}{2}(|n| + \nu + 3)\right]} \ . \tag{5.10}$$

Eqs. (5.7) and (5.8) are the main equations that will be used subsequently to obtain VC structure function of each MHD modes. An useful parameter for comparison with past numerical work is the isotropy degree, defined as

$$\text{Isotropy Degree} = \frac{\mathcal{D}(R, \phi = 0)}{\mathcal{D}(R, \phi = \pi/2)} \ . \tag{5.11}$$

5.2 Centroids for different MHD modes

With this general formalism introduced in Sec. 5.1, we are ready to proceed to study VC anisotropy in detail for each MHD modes. We will use the tensor structures obtained Sec. 2.2 in order to study anisotropy due to each MHD mode.

5.2.1 Alfvén mode

Making use of Eq. (2.25), we obtain

$$\left(\hat{\xi}_{\mathbf{K}} \otimes \hat{\xi}^{*}_{\mathbf{K}}\right)_{zz} = 1 - \frac{\hat{\lambda}_z \hat{\lambda}_z}{1 - (\hat{\mathbf{K}} \cdot \hat{\Lambda})^2} = \sin^2\gamma \frac{\sin^2\psi}{1 - \sin^2\gamma\cos^2\psi} \ , \tag{5.12}$$

where $\cos\gamma = \hat{r} \cdot \hat{\lambda}$, and $0 \leq \gamma \leq \pi/2$. Note that correlation given by Eq. (5.12) vanishes at $\gamma = 0$, which is expected as motions are perpendicular to the magnetic field. Making use of Eqs. (5.8) and (5.12), the multipole moments of VC structure function for Alfvén mode can be written as

$$\mathcal{D}_n(R) = C_n(2/3) \sum_{p=-\infty}^{\infty} \hat{\mathcal{A}}_p \mathcal{W}^A_{n-p} R^{5/3} \ , \tag{5.13}$$

where $\hat{\mathcal{A}}_p$ is the coefficient of two dimensional harmonic expansion of power spectrum, and, as suggested in (Cho and Lazarian, 2002), is given by

$$\hat{\mathcal{A}}_p = \frac{1}{2\pi} \int_0^{2\pi} \mathrm{d}\psi \, \mathrm{e}^{-\mathrm{i}p\psi} \exp\left[-M_{\mathrm{A}}^{-4/3} \frac{|\cos\psi| \sin\gamma}{(1 - \cos^2\psi \sin^2\gamma)^{2/3}}\right] \ , \tag{5.14}$$

and $\mathcal{W}^A_{n-p}$ spectral weight defined as

$$\mathcal{W}^A_{n-p} = \frac{1}{2\pi} \int_0^{2\pi} \mathrm{d}\psi \, \mathrm{e}^{-\mathrm{i}(n-p)\psi} \frac{\sin^2\gamma \sin^2\psi}{1 - \sin^2\gamma\cos^2\psi} \ . \tag{5.15}$$

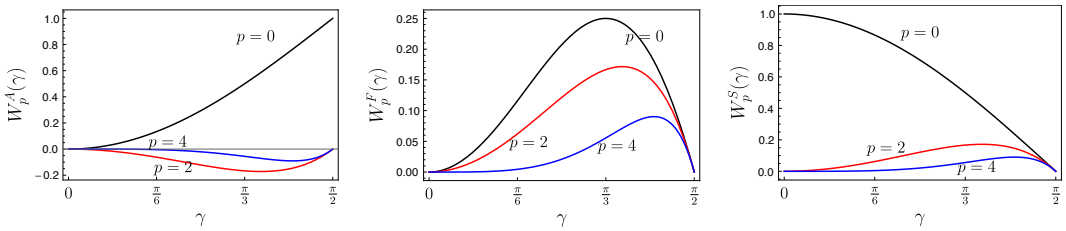

Figure 5.1: From left-hand to right-hand: spectral function of Alfvén mode $W_p^A(\gamma)$ (left-hand), low-β fast mode $W_p^F(\gamma)$ (center) and high-β slow mode $W_p^S(\gamma)$ (right-hand) for various index p (which is $n-p$ in Eq. (5.8).

An analytical form of this spectral weight exists and is given by

$$\mathcal{W}_{n-p}^A = \delta_{p,n} - \cos\gamma \left(\frac{1-\cos\gamma}{\sin\gamma}\right)^{|n-p|} . \tag{5.16}$$

It is clear from Eqs. (5.13) and (5.15) that the VC structure function of Alfvén mode vanishes at $\gamma = 0$, which reflects that there is no LOS component of the Alfvén velocity when magnetic field is along the LOS. In the opposite case $\gamma = \pi/2$ when magnetic field is perpendicular to the LOS, $\mathcal{W}_{n-p}^A = \delta_{pn}$, and multipole moments of the VC structure function $\mathcal{D}_n(R) \propto \mathcal{A}_n$. It can be clearly seen from the left hand panel of Fig. 5.1. For general γ, it is also clear from the figure that the magnitude of the function $\mathcal{W}_{n-p}^A$ decays rapidly as $|n-p|$ increases. This means that for our practical purposes, it is enough to just take few terms near $p \approx n$ in the sum presented in Eq. (5.13).

Fig. 5.2 shows some important properties of Alfvén mode. Firstly, looking at this figure one can clearly see that this mode looks more isotropic with increasing Alfvén Mach number $M_{\rm A}$, as characterised by the decreasing level of quadrupole to monopole and octupole to monopole ratio and increasing level of isotropy degree with increasing $M_{\rm A}$. It is also quite clear from the left-hand and central panel of the figure that this mode becomes highly anisotropic at $\gamma = \pi/2$, which is expected. Note that the finite quadrupole to monopole ratio at $\gamma = 0$ is misleading in a sense that both quadrupole and monopole vanish at $\gamma = 0$. In the case when one considers the mixture of modes, this problem is

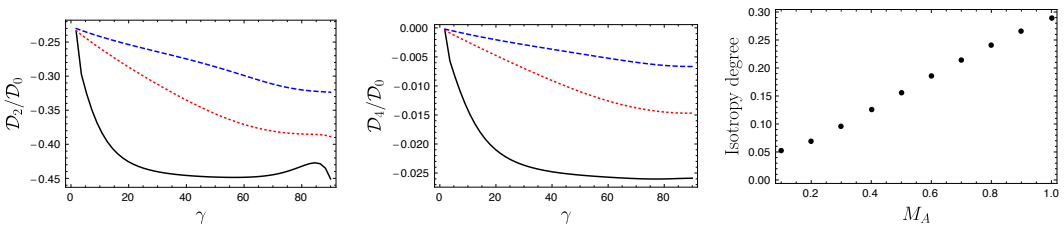

Figure 5.2: Alfvén mode. Left-hand and center: quadrupole to monopole and octupole to monopole ratio for various γ. Solid line is for $M_{\rm A} = 0.1$, dotted line for $M_{\rm A} = 0.4$ and dashed line for $M_{\rm A} = 0.7$. Right-hand: isotropy degree for various $M_{\rm A}$ at $\gamma = \pi/2$.

remedied as slow modes and high-β fast modes have non-vanishing monopole at $\gamma = 0$.

5.2.2 Slow mode

Using Eq. (2.34), we can write

$$\left(\hat{\xi}_{\mathbf{K}} \otimes \hat{\xi}^*_{\mathbf{K}}\right)_{zz} = \frac{\hat{\lambda}_z \hat{\lambda}_z}{1 - (\hat{\mathbf{K}} \cdot \hat{\Lambda})^2} = \frac{\cos^2\gamma}{1 - \sin^2\gamma \cos^2\psi} \,. \tag{5.17}$$

Using Eqs. (5.8) and (5.17), one can obtain the multipole moments of the VC structure function as

$$\mathcal{D}_n(R) = C_n(2/3) \sum_{p=-\infty}^{\infty} \hat{A}_p \mathcal{W}^S_{n-p} R^{5/3} \,, \tag{5.18}$$

where the spectral weight function $\mathcal{W}^S_p$ is given by

$$\begin{aligned} \mathcal{W}^S_{n-p} &= \frac{1}{2\pi} \int_0^{2\pi} \mathrm{d}\psi \, \mathrm{e}^{-\mathrm{i}(n-p)\psi} \frac{\cos^2\gamma}{1 - \cos^2\psi \sin^2\gamma} \\ &= \cos\gamma \left(\frac{1 - \cos\gamma}{\sin\gamma}\right)^{|n-p|} \,. \end{aligned} \tag{5.19}$$

The spectral weight function of slow modes, given by Eq. (5.19), is plotted in the left-hand panel of Fig. 5.1. It is clear from Fig. 5.1 that $\mathcal{W}^S_{n-p}$ vanishes at $\gamma = \pi/2$ for all $n - p$, and therefore, the structure function vanishes at this

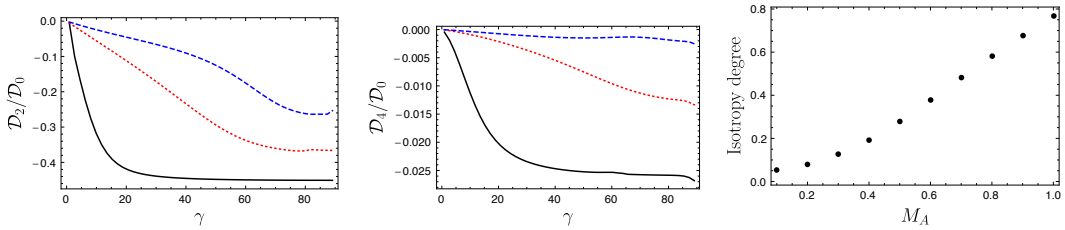

Figure 5.3: High-β slow mode. Left-hand and center: quadrupole to monopole and octupole to monopole ratio for various γ. Solid line is for $M_{\rm A} = 0.1$, dotted line for $M_{\rm A} = 0.4$ and dashed line for $M_{\rm A} = 0.7$. Right-hand: isotropy degree for various $M_{\rm A}$ at $\gamma = \pi/3$.

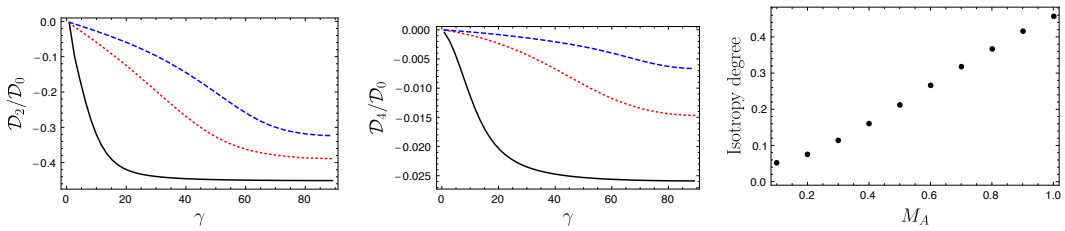

Figure 5.4: Low-β slow mode. Left-hand and center: quadrupole to monopole and octupole to monopole ratio for various γ. Solid line is for $M_{\rm A} = 0.1$, dotted line for $M_{\rm A} = 0.4$ and dashed line for $M_{\rm A} = 0.7$. Right-hand: isotropy degree for various $M_{\rm A}$ at $\gamma = \pi/3$.

angle. In the opposite case, $\gamma = 0$, $\mathcal{W}^S_{n-p}$ vanishes for all non-zero $n-p$ and equal to 1 for $n = p$, but $\hat{\mathcal{A}}_p = 0$ for $p > 0$; therefore, no anisotropy is present. For general γ, $\mathcal{W}^S_{n-p}$ decays very rapidly with increasing $|n-p|$, which implies that for practical purposes, it is enough to just few terms near $p \approx n$ in the sum presented in Eq. (5.18).

Slow modes in low-β have their correlation function as $\langle v_i v_j \rangle \propto \hat{\lambda}_i \hat{\lambda}_j$ and therefore, it can be straightforwardly shown that

$$\mathcal{D}_n(R) = C_n(2/3)\cos^2\gamma \hat{\mathcal{A}}_n R^{5/3} \ . \tag{5.20}$$

Slow modes in both high- and low-β plasma are highly anisotropic at small $M_{\rm A}$ and become more isotropic with increasing $M_{\rm A}$. This is clearly shown in Figs. 5.3 and 5.4. Moreover, the anisotropy level of both high- and low-β slow modes are similar. This is because the dominant term in Eq.(5.18) is the

diagonal term $n = p$, while the $\cos^2\gamma$ term in Eq. (5.20) cancels upon taking ratio of multipole moments, thus the ratio of multipole moments in both cases yield similar results. It is important to note that the anisotropy of slow modes at $\gamma = \pi/2$ cannot be measured as both quadrupole and monopole vanish at $\gamma = \pi/2$.

5.2.3 Fast mode

Fast modes in high-β are purely compressible modes with a velocity tensor structure given by Eq. (2.28). The power spectrum of fast modes is isotropic, and therefore the velocity correlation tensor is isotropic as well.

On the other hand, low-β fast mode is anisotropic with the anisotropy built in its tensor structure (see Eq. (2.31)). Making use of Eq. (2.31), we obtain

$$\left(\hat{\xi}_{\mathbf{K}} \otimes \hat{\xi}^*_{\mathbf{K}}\right)_{zz} = \frac{(\sin\gamma\cos\gamma)^2\cos^2\psi}{1-\sin^2\gamma\cos^2\psi} \ . \tag{5.21}$$

Keeping in mind that fast modes have isotropic power spectrum so that only $\hat{\mathcal{A}}_0$ in non-vanishing, we have

$$\mathcal{D}_n(R) = C_n(1/2)\mathcal{A}_0\mathcal{W}^F_n R^{3/2} \ , \tag{5.22}$$

where the spectral weight function W^F_n is defined as

$$\begin{aligned}\mathcal{W}^F_n &= \frac{1}{2\pi}\int_0^{2\pi} \mathrm{d}\psi \mathrm{e}^{-\mathrm{i}n\psi}\frac{(\sin\gamma\cos\gamma)^2\cos^2\psi}{1-\sin^2\gamma\cos^2\psi} \\ &= -\cos^2\gamma\delta_{n0} + \cos\gamma\left(\frac{1-\cos\gamma}{\sin\gamma}\right)^{|n|} \ . \end{aligned} \tag{5.23}$$

This spectral weight function of fast mode is plotted in the central panel of Fig. 5.1, which shows that this function vanishes both at $\gamma = 0$ and $\gamma = \pi/2$. The left-hand panel of Fig. 5.5 shows that the quadrupole to monopole ratio of low-β fast mode is ~ 0.3 through out the entire range of γ. The quadrupole

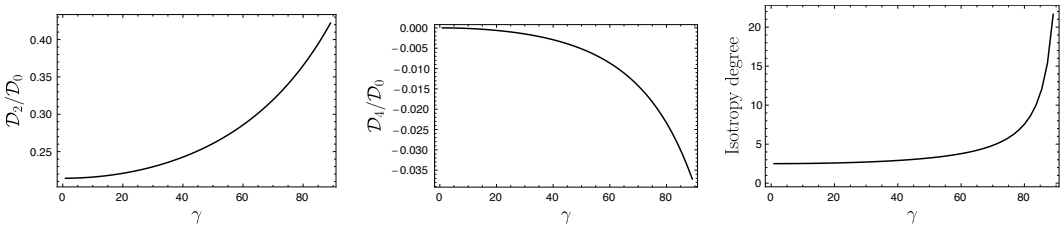

Figure 5.5: Low-β fast mode. Left-hand to right-hand: quadrupole to monopole, octupole to monopole ratio and isotropy degree for various γ.

to monopole ratio somewhat increases with increasing γ to its maximum value ≈ 0.4 at $\gamma = \pi/2$, however, the amplitude of both monopole and quadrupole is ~ 0 at $\gamma \sim \pi/2$. In fact, the optimal signal is obtained at $\gamma \sim \pi/3$.

Note that since $C_2(1/2) > 0$, the quadrupole moment of fast mode is positive, which is also distinct from Alfvén mode. We found that this is due to the fact that anisotropy of fast mode comes from its anisotropic tensor structure and not from its power spectrum.

5.2.4 Mixture of modes

Real world setting of MHD turbulence involves superposition of the different MHD modes. Therefore, we consider the effect of mixtures of different MHD modes in the observed VC anisotropy. In the case of mixture between Alfvén and slow modes, Fig. 5.6 clearly shows that the observed anisotropy is unaffected by this mixture in different regimes. For instance, the observed anisotropy of the mixture at $\gamma \gtrsim \pi/4$ is the same as that of Alfvén mode alone while at $\gamma \lesssim \pi/4$, the anisotropy level is similar to that of slow modes alone. This is again due to the fact that at $\gamma \approx \pi/2$ signal from Alfvén mode is dominant while at $\gamma \approx 0$ signal from slow mode is dominant. On the other hand, we expect the mixture of fast mode with other two modes to decrease the level of anisotropy. This is because the quadrupole moment (which is the measure of anisotropy) of fast mode is opposite in sign than that of other modes.

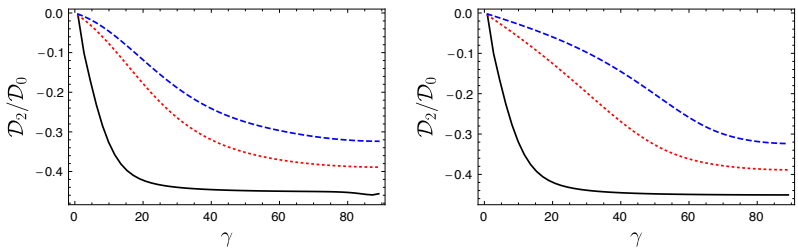

Figure 5.6: Mixture of modes. Left-hand: quadrupole to monopole ratio for a mixture of 85% Alfvén and 15% high-β slow modes. Right-hand: same for a mixture of 50% Alfvén and 50% low-β slow modes. Solid line is for $M_{\rm A} = 0.1$, dotted line for $M_{\rm A} = 0.4$ and dashed line for $M_{\rm A} = 0.7$.

5.2.5 Density effects

The main aim of using velocity VC is to obtain information about velocity spectrum. Looking at Eq. (3.20), one can see that the VC structure function contains not only the contribution from velocity effects but also from density effects. In this regard, separating velocity contribution from density contribution is not always possible. In particular, if the density spectrum is shallow, as is the case for super-sonic turbulence, one might not be able obtain the velocity spectra from the VC. On the other hand, for a steep density spectra the velocity spectra can be extracted if the density dispersion in a turbulent field is less than the mean density (Esquivel et al., 2007). This has been clearly illustrated in the left-hand panel of the Fig. 5.7, where the VC structure function is plotted for various ratios of σ_ρ/ρ_0. It is clearly shown in the figure that the velocity spectra can be obtained when $\sigma_\rho/\rho_0 < 1$, while the spectra is corrupted by the density-velocity cross-term when $\sigma_\rho/\rho_0 > 1$.

As explained in Lazarian and Esquivel (2003, henceforth LE03), VC can trace the velocity spectrum if the VC structure function is much larger than the first term of Eq. (3.20). If this condition is not fulfilled, the velocity spectrum can be obtained by subtracting the first term (product of velocity dispersion and density correlation) of Eq. (3.20) as long as the density corre-

lation can be measured independently[1] and density-velocity correlation is not strong. A potential challenge is the determination of velocity dispersion in the case when thermal broadening is large. However, one can circumvent this by using emission lines of heavier species. In this regard, LE03 introduced a notion of 'modified' velocity VC (MVC), where the first term of Eq. (3.20) was subtracted. Formally, the structure function of MVC in the absence of density-velocity correlation is

$$\mathcal{D}_{\rm MVC}(\mathbf{R}) \approx \int_{-S}^{S} {\rm d}z[\xi_\rho(\mathbf{r})D_z(\mathbf{r}) - \xi_\rho(0,z)D_z(0,z)] \ . \tag{5.24}$$

It was explained in LE06 that MVCs can trace the velocity spectrum better than the 'unnormalised' VC (UVC) if the lag R under study be smaller than the saturation scale of the velocity structure function as well as the line of sight extent S of the turbulent cloud. We find that the MVC is able to trace the velocity spectra even for a shallow spectrum, as illustrated in Fig. 5.7. In fact, Fig. 5.8 clearly show that modified VC work better than UVC at smaller lags R. Note that for shallow density field, density-velocity cross-term yields a scaling $R^{1+\nu_\rho+\nu}$, while pure velocity term yields $R^{1+\nu}$, and since $\nu_\rho < 0$ for a shallow density spectra, this cross-term scaling can dominate the MVC scaling is extremely small scale. Although, we see that MVCs work well even for shallow density spectra, there are two important points to make. First, we require $\sigma_\rho/\rho_0 < 1$ to obtain velocity spectra correctly, otherwise density-velocity correlation (which we ignored) becomes important (Esquivel et al. 2007). However, shallow density often does not fulfil this criteria. Second, shallow density is often associated with high sonic Mach number $M_{\rm s}$ where non-Gaussian features are often prominent, significantly affecting the statistics. To sum up, one needs to know σ_ρ/ρ_0 to conclude if MVCs work for shallow

[1]Note that one can obtain this contribution from the density term observationally by measuring intensity fluctuations. For instance, in the language of VCA this term can be obtained through intensity statistics in the 'thick slice' limit (see LP00 for more details).

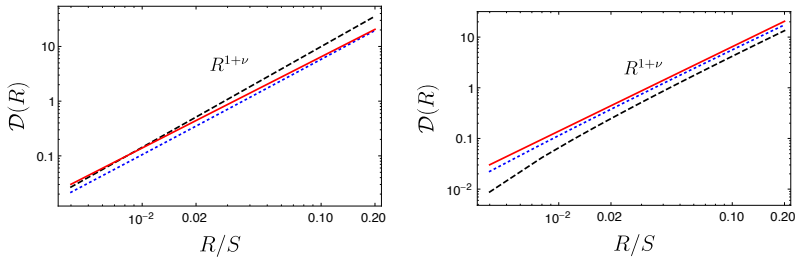

Figure 5.7: First panel: MVC structure function for various σ_ρ/ρ_0 for *steep* velocity field of Kolmogorov index 2/3 and density fields of index $\nu_\rho = 1/2$. The solid line is expected power law of $R^{5/3}$, the dotted line is for $\sigma_\rho/\rho_0 = 0.5$ and the dashed line for $\sigma_\rho/\rho_0 = 1$. One can see some deviation from the power law behaviour already at $\sigma_\rho/\rho_0 = 1$. This deviation is expected to be stronger with increasing σ_ρ/ρ_0. Second panel: The same but for *shallow* density with $\nu_\rho = -1/2$. The dotted line is for $\sigma_\rho/\rho_0 = 0.5$ and dashed line is for $\sigma_\rho/\rho_0 = 1$. Solid line is the power law $R^{5/3}$ from pure velocity effects.

spectra.

Our study of anisotropy was for constant density field. In the case when density field is anisotropic, one should also account for the anisotropy due to density effects as well. For MVC the anisotropy is dominated by velocity effects as long as the density dispersion is less than the mean density. On the other hand, both density and velocity effects contribute to the UVC anisotropy.

5.2.6 Comparisons with earlier numerical works

The numerical study of anisotropies with VC has been carried out in the past in LE06, Esquivel and Lazarian (2011, hereafter EL11) and Burkhart et al. (2014, hereafter BX14). Here we compare our findings with the findings of EL11 and BX14. EL11 studied anisotropies at $\gamma = \pi/2$, while BX14 studied anisotropy at varying γ as well. Both of these studies found out a clear dependence of anisotropy with Alfvén Mach number $M_{\rm A}$. They reported that the anisotropy increases with decreasing $M_{\rm A}$, which coincides with our result. As an example, at $M_{\rm A} = 0.7$ and $M_{\rm s} = 2.3$, the degree of isotropy in both the papers was reported to be ~ 0.3, while our results show that in the case when Alfvén and slow modes are dominant, the isotropy degree at $M_{\rm A} = 0.7$ is around ~ 0.25,

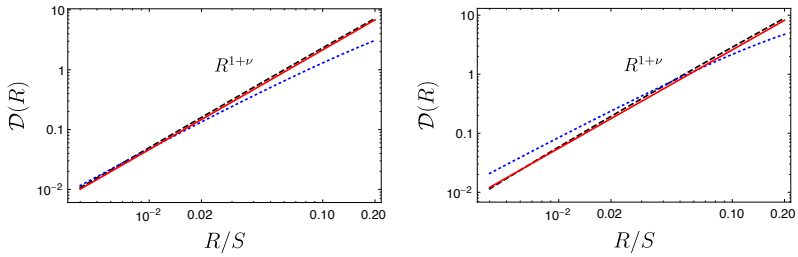

Figure 5.8: Plot showing comparison of MVC with UVC at $\sigma_\rho/\rho_0 = 0.5$ at short scales $R < S$. The dashed line in both the panels are for MVC, dotted line is for UVC and solid line shows the power law $R^{5/3}$ from pure velocity effects. In both figures a *steep* velocity spectrum of Kolmogorov index is assumed, whereas density spectrum is assumed to be *steep* (with $\nu_\rho = 1/2$) in the first panel and *shallow* (with $\nu_\rho = -1/2$) in the second. It is clear that MVC works well for both steep and shallow spectra.

which is close to their results. Our finding that the degree of anisotropy is highest at $\gamma = \pi/2$ matches with the findings in BX14, where it was stated that at $\gamma = \pi/2$ the anisotropy is highest regardless of the sonic Mach number $M_{\rm s}$. It is clear from our finding that the isotropy degree of VC is clearly dependent on $M_{\rm A}$. However, it was discussed in EL11 and BX14 that besides a dependence of isotropy degree of $M_{\rm A}$, there exists a weak dependence on $M_{\rm s}$ as well. Although there is no direct role of $M_{\rm s}$ in determining the degree of isotropy in our formalism, this weak dependence can be explained by noting that with an increasing $M_{\rm s}$, there is an increasing contribution from fast mode, thus decreasing the level of anisotropy. This is consistent with the results in EL11 and BX14.

Chapter 6

Discussion

6.1 Foundations of the technique

This thesis continues the work of quantitative study of the PPV space that was initiated in LP00 for the case of optically thin turbulent medium and later extended in LP04 for the absorbing media. These advances produced the machinery for describing the PPV space that our present study is based upon.

The next significant advancement is related to the present-day understanding of MHD turbulence theory (see Beresnyak and Lazarian 2015 for a review). Theoretical and numerical research (GS95, Lithwick and Goldreich 2001; Cho and Lazarian 2002, 2003; Kowal and Lazarian 2010) have shown that the MHD turbulence can be viewed as a superposition of the cascades of Alfvén, slow and fast modes. The representation of the statistical properties of these cascades in the global frame of reference was obtained in LP12, where the anisotropy analysis of synchrotron fluctuations was quantified. We particularly stress the importance of the observational frame, as this frame is related to the mean magnetic field, and the statistics of fluctuations in this frame is different from the statistics in the local magnetic field frame in which the Alfvénic turbulence is formulated (Cho and Vishniac 2000; LV00; Maron and Goldreich 2001; Cho et al. 2002).

6.2 New Power of VCA and centroids

The present study significantly extends the ability of the VCA and VC techniques by augmenting their ability to study turbulence magnetization and to determine the magnetic field direction in a turbulent cloud. It also outlines possible ways for separating contribution of Alfvén, slow and fast modes. The latter is important due to the fact that different modes have different impact for astrophysical processes. For instance, Alfvénic modes are essential for magnetic field reconnection (LV99; see also Lazarian et al. 2015 and references therein), superdiffusion of cosmic rays perpendicular to the mean magnetic field direction (Lazarian and Yan 2014), while fast modes dominate resonance scattering of cosmic rays (Yan and Lazarian 2002). The potential ability of VCA and VC to determine the relative contribution of these different modes for spectroscopic data complements this ability for the technique in LP12 and LP16 for synchrotron data. This has the potential of bringing observational quantitative studies of turbulence to a new level.

6.3 Model assumptions

Our analytical studies require adopting different assumptions. First is that the fluctuations are Gaussian. This assumption is satisfied to an appreciable degree by the turbulent velocity field (see Monin et al. 1975), but is not necessarily a good assumption for the description of density fluctuations, especially at high sonic Mach number. Fortunately, the VCA is mostly focused on studying velocity statistics and for some regimes, e.g. steep density, the density fluctuations do not affect statistics of thin slices. It was also shown in LP00 that the VCA formulae stay valid even for the lognormal distribution of density. Thus, we do not believe that our Gaussianity assumption is a serious shortcoming.

The independence of velocity and density fluctuations is another assumption employed in the derivation of the basic equations of the VCA. The effect

of this assumption was analysed in LP00, where it was shown that even in the case of the maximal possible velocity-density cross-correlation that follows from general Cauchy-Schwarz inequality (see Mathews and Walker 1970), the expressions for the thin slices stay the same for the steep velocity (see more discussion in appendix D of LP00). The measures of anisotropy are expected to be more robust compared to the spectrum. Thus, we expect the VCA not to be affected by this assumption.

The decomposition of MHD turbulence into Alfvén, slow and fast modes is also an approximation based on the assumption of small coupling between these different modes. The degree of coupling of the modes was quantified in Cho and Lazarian (2002), and it was shown to be very moderate unless the sonic Mach number of the media is very high. The exact spectral slope of fast modes may change for high sonic Mach number, but this should not change significantly the anisotropy analysis in this thesis.

In terms of the turbulent media to be studied by the techniques we have studied in our work, it is assumed that the media are isothermal. This is an excellent assumption for molecular clouds. The effects of the variations of temperature within atomic hydrogen were discussed in LP00, where it was shown that temperature variations make the contributions of hotter gas sub-dominant compared to the colder gas.

6.4 Comparison between VCA, Centroids and VCS

The VCA introduced in LP00 provided a new foundation for studying velocity and density turbulence by studying the changes of spectral slope of intensity fluctuations within velocity slices of PPV cubes. It was shown in LP00 that by choosing a sufficiently thin slice, one might be able recover the velocity spectrum, whereas for sufficiently thick slice the velocity effects get washed

away and only density spectrum can be recovered. The VCA was later extended in LP04 to account for the effects of self-absorption of emission lines. The results of LP04 suggests that in the presence of self-absorption, one might not be able to recover velocity spectrum, especially if the absorption is strong or the thermal broadening $\beta_{\rm T}$ is larger than the dispersion of the velocity field. In fact, it was shown in LP04 that at some intermediate wavenumber K, one might observe a universal spectrum $P(K) \sim K^{-3}$, a spectrum measured in a number of studies (see examples in Lazarian 2009). The original formulation of VCA dealt only with power spectra, and this technique was further extended in this thesis to study the anisotropies induced by magnetic field in a turbulent plasma. This study shows how the anisotropy of an underlying turbulent field maps to anisotropy of intensity fluctuations, and shows how the level of anisotropy depends on the Alfvén Mach number as well as the angle between LOS and mean magnetic field.

VC is another powerful technique to study turbulence. We believe that our extension of VC to study turbulence anisotropies significantly improves the value and power of this technique. The geometrical construction of VCA and UVC is presented in Fig. 3.2.

Although both VCA and VC can be used to study turbulence properties, there are several differences between the two techniques. The first important difference between the VCA and VC is how thermal broadening $\beta_{\rm T}$ affects them. While VCA cannot recover velocity spectrum at scales R where $D_z(R) < \beta_{\rm T}$, VC still work in this regime. This means that VCA does not work well for sub-sonic turbulence unless we use emission lines from sub-dominant slow massive species. VC, on the other hand, are not reliable for supersonic turbulence (see Esquivel et al. 2007). This is in contrast with VCA, which works well in this regime.

Besides VCA and VC, VCS is another useful technique to study turbulence. Unlike VCA and VC, VCS exclusively uses data along the velocity coordinate

(in particular in the Fourier space), and one does not need to spatially resolve the scale of turbulence under study. A major advantage of VCS is that only few independent measurements are enough to obtain information about the underlying velocity field (Chepurnov & Lazarian 2008). It is important to note, however, that VCS does not deal with anisotropies, but only with spectrum.

We stress the importance of using different techniques like VCA, VCS and VC when studying multi-phase ISM, e.g. H I and H α. While VCA and VCS do not work well for gas components with large thermal broadening $\beta_{\rm T}$ due to thermal dampening of the fluctuations[1], VC work well for both hot and cold components at least as long as the turbulence is subsonic. Therefore, synergy of different techniques is advantageous, given that different techniques work well at different regimes.

6.5 Spectroscopic and synchrotron studies of magnetic turbulence

For synchrotron polarization studies, the analogue of PPV cube is the position-position-frequency (PPF) cube. In LP16, a number of techniques were suggested aimed at obtaining the information about magnetic field and the density of cosmic electrons using these cubes. In terms of anisotropy studies, it was suggested there to make use of the analysis of synchrotron intensity fluctuations in order to determine the same parameters that we focused in this study, namely the mean magnetic field direction, the degree of magnetization of the media and the contribution of Alfvén, slow and fast modes. This suggests that studies of turbulence using synchrotron and spectroscopic data can be very much complementary. Indeed, for the understanding of dynamics of the ISM as well as for processes of the transport of heat and cosmic rays, it is

[1]One strategy to use VCA and VCS in a hot medium is to use emission lines from heavy species like Fe.

essential to understand the properties of turbulent cascade in different interstellar phases. Synchrotron emission samples turbulence mostly in the diffuse hot and warm media (see Draine 2010 for the table of the interstellar phases), while the turbulence in H I and molecular gas is well sampled via spectroscopic measurements[2]. The correspondence of the properties of magnetic turbulence in different interstellar phases would testify about the single turbulent cascade on the galactic scale, which can be a discovery with important consequences for different branches of astrophysical research, e.g. for cosmic ray physics (see Schlickeiser 2002).

While the properties of turbulent fluctuations of magnetic field and velocity are closely related, there are differences. In particular, magnetic field is solenoidal, while velocity in MHD turbulence can have a potential component. Therefore, the treatments of anisotropy of magnetic turbulence and velocity turbulence in this work and in LP12 are similar, but not completely identical. Potentially, the VCA technique provides way to study compressible motions in a more adequate way.

The generalization of the anisotropy study from pure synchrotron intensity in LP12 to synchrotron polarization in LP15 opened up ways to study anisotropies of MHD statistics in the PPF space. It is also interesting to compare the statistics of the PPV and the PPF. The PPV statistics is homogeneous along the v-axis, while the one of PPF is inhomogeneous. As a result, due to the effect of Faraday depolarization, for different frequencies one can sample turbulence at different distances from the observer, which allows study of the spatial distribution of turbulence. Such an effect is not present for the PPV studies. However, the homogeneity of the PPV in the v-direction allows one to better separate the contribution of the Alfvén, fast and slow modes by varying the slice thickness. Therefore, the statistical information in PPV is complimentary

[2]Future X-ray spectroscopy (similar to Astro-H (Mitsuda et al., 2014)) should provide a way to study hot plasma turbulence using spectroscopic techniques as well.

to the statistics that can be obtained from PPF.

6.6 Synergy with other techniques

In this thesis, we studied anisotropies of intensity fluctuations and VC fluctuations by extensively making use of PPV space formalism. We have also discussed and compared VC with the VCA and VCS, the techniques that were developed also by using PPV space formalism. Another technique called principal component analysis (PCA, see Brunt and Heyer 2002) can also be used to study turbulence anisotropies. However, unlike the VC and VCA, it is not easy to quantify PCA using PPV data. Nevertheless, recent studies have shown the sensitivity of PCA to the phase information (Correia et al. 2016), although the trend is not yet clear.

Another important technique to study turbulence using velocity slice of PPV space is the spectral correlation function (SCF, see Rosolowsky et al. 1999). The SCF is very similar to VCA if one removes the adjustable parameters from SCF. In fact, both SCF and VCA measure correlations of intensity in velocity slices of PPV, but the SCF treats outcomes empirically. There also exist numerous techniques identifying and analyzing clumps and shells in PPV (see Houlahan and Scalo 1992; Williams et al. 1994; Stutzki and Guesten 1990; Pineda et al. 2006; Ikeda et al. 2007).

Besides the VCA and VC, there are also some other techniques to study sonic and Alfvén Mach numbers. Some of these techniques include so called Tsallis statistics (see Esquivel and Lazarian 2010; Tofflemire et al. 2011), bispectrum (see Burkhart et al. 2009), and genus analysis (see Chepurnov et al. 2008). Using different available techniques allows one to obtain a comprehensive picture of MHD turbulence.

One of the parameters that influence the VCA is the density statistics, which includes both its spectrum and anisotropy. This statistics can be obtained

through the analysis of different data sets, e.g. dust emission or absorption. This should increase the accuracy of the VCA in determining the statistics of velocity.

Combining the present technique with the synchrotron studies for independently obtaining the magnetization and decomposition of turbulence into the fundamental MHD modes is very advantageous. The intriguing opportunity of obtaining the angle between the mean magnetic field and the LOS on the basis of synchrotron polarization data that were discussed in LP16 allows one to remove the degeneracy between this angle and the Mach number that exists otherwise.

6.7 Future work

All the studies of turbulence that were mentioned above do not account for the absorption by dust, however. This is acceptable for studies of turbulence using radio lines, e.g. 21 cm H I line, CO lines. However, dust absorption affects optical and UV lines. In fact, this was a problem that the earlier researchers were aware of (see Münch 1958). Thus, a natural extension of the important techniques, such as VCA, VCS and VC, that are used to study ISM turbulence would be to take into account the effects of dust absorption. This has already been achieved in our recent work Kandel et al. (2017a), where the effects of dust absorption on spectroscopic study of turbulence was studied. Physically, emission from optical depth larger than unity are absorbed by dust. However, in the presence of dust density fluctuations, the physical depth along the line of sight at which the optical depth reaches unity also fluctuates. Thus, the aim of the paper was to answer the following question: in the presence of dust absorption, can velocity and density spectra characterising turbulence still be obtained using emission lines? Our work shows that while velocity spectra can be obtained even in the presence of dust absorption, one might not be able to

obtain gas density spectra, as dust saturates different statistical measures.

As a next step, we are interested in using dust polarization maps to study ISM turbulence. Dusts are important foregrounds that need to be subtracted for the study of CMB polarization. However, they are also valuable in the study of ISM turbulence. Polarization maps can be decomposed into purely solenoidal E modes and purely compressible B modes. Recent Planck measurements of dust polarization at 353 GHz shows that the power of E mode is twice that of power in B mode (Adam et al., 2016). This result was surprising, as previous expectation was an equal power in these polarization modes. Caldwell et al. (2017) attempted to explain this surprising result using the model of MHD turbulence as a superposition of three MHD waves: Alfvén, fast and slow. Based on their result, they concluded that at large scale turbulence could be unimportant, as there is a very narrow range of parameters in the theoretical model that could possibly mimic the Planck result. This result perturbed the community as it questions the generally accepted notion of turbulent origin of dust-polarization fluctuations. To address the issue raised by Caldwell et al. (2017), we are revisiting the problem in Kandel et al. (2017b) and are arguing that with realistic interstellar medium (ISM) conditions, the range of theoretical parameters that mimics the Planck result does not contradict to what we know about the ISM at high galactic latitudes. In fact, we showed that the Planck result can be explained in the context of MHD turbulence if the Alfvén Mach number in the high Galactic latitude is less than 0.5 (see Fig. 6.1). The latter number is in agreement with the existing expectations (see Beck 2016). Our ongoing work (in prep) has also raised some interesting and exciting possibilities of using temperature-E mode (TE) cross-correlation to study extent of density-magnetic field correlation, compressibility of the turbulent media. We also plan to carry out similar analysis using Planck result of synchrotron polarization.

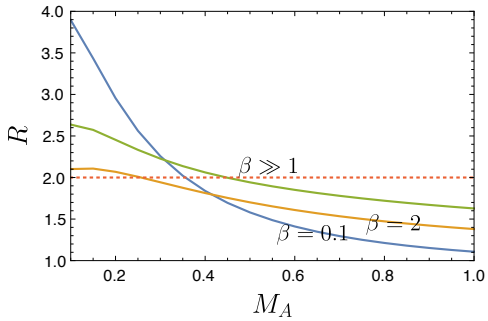

Figure 6.1: Ratio of E to B power for dust polarization for an equal mix of Alfvén, fast and slow modes. Three curves at $\beta = 0.1$, $\beta = 2$ and $\beta = 10$ are shown. The dotted line is the Planck expectation of 2. One can clearly see that at low M_A, the ratio of 2 can be easily achieved.

Chapter 7

Summary

In this thesis, we have extended the VCA and VC technique based on the analysis of fluctuation statistics in the velocity slices of the PPV space (i.e. velocity channel maps). Unlike the earlier study in LP00 and LP04, we accounted for the anisotropy of turbulence and provided expressions for the anisotropies in the velocity channel maps and VC maps that arise from Alfvén, slow and fast modes of MHD turbulence. We calculated how these anisotropies change with the thickness of the velocity channel maps and compared our results with the numerical study in ELP15.

Our study main results are as follows.

- Analytical expressions for the measure of anisotropy of intensity fluctuations in slices of PPV space, as well as for the VC were obtained.

- The procedures of separating contributions to anisotropy arising from density fluctuations and velocity fluctuations were studied, and the technique of establishing the anisotropies of density and velocity underlying turbulent field was formulated.

- The separation of the contributions from Alfvén, slow and fast modes was investigated for the thin slice regime of VCA, as well as for VC, and the ratio of the anisotropic to isotropic part of the slice intensity

fluctuations, as well as VC fluctuations were identified as a measure for fluid magnetization and compressibility.

- We showed the complementary nature of turbulence studies with VC and the Velocity Channel Analysis (VCA). Both techniques can measure turbulence spectra and anisotropy. While VC are reliable for study of subsonic turbulence statistics, one has to use only heavier species, e.g. metals in hydrogen gas, to study subsonic turbulence using VCA.

- Analytical expression of UVC structure function and anisotropy level for sub-Alfvénic turbulence are derived. These expressions are used to study the anisotropy arising from three MHD modes: Alfvén, fast and slow. It is shown that the quadrupole to monopole ratio of fast mode is positive, while it is negative for Alfvén and slow mode. In other words, iso-correlation contours are elongated along sky-projected magnetic field direction for Alfvén and slow modes, and orthogonal to it for fast modes, which is same as what VCA predicts.

Bibliography

R Adam, Peter AR Ade, Nabila Aghanim, M Arnaud, J Aumont, C Baccigalupi, Anthony J Banday, RB Barreiro, JG Bartlett, N Bartolo, et al. Planck intermediate results-xxx. the angular power spectrum of polarized dust emission at intermediate and high galactic latitudes. *Astronomy & Astrophysics*, 586:A133, 2016.

JW Armstrong, BJ Rickett, and SR Spangler. Electron density power spectrum in the local interstellar medium. *ApJ*, 443:209–221, 1995.

Rainer Beck. Magnetic fields in spiral galaxies. *The Astronomy and Astrophysics Review*, 24(1):4, 2016.

F Bensch, Jürgen Stutzki, and Volker Ossenkopf. Quantification of molecular cloud structure using the δ-variance. *Astronomy & Astrophysics*, 366(2): 636–650, 2001.

A. Beresnyak and A. Lazarian. MHD Turbulence, Turbulent Dynamo and Applications. In A. Lazarian, E. M. de Gouveia Dal Pino, and C. Melioli, editors, *Magnetic Fields in Diffuse Media*, volume 407 of *Astrophysics and Space Science Library*, page 163, 2015.

A Beresnyak, A Lazarian, and J Cho. Density scaling and anisotropy in supersonic magnetohydrodynamic turbulence. *ApJ Letters*, 624(2):L93, 2005.

Axel Brandenburg and A Lazarian. Astrophysical hydromagnetic turbulence. *Space Science Reviews*, 178(2-4):163–200, 2013.

Christopher M Brunt and Mark H Heyer. Interstellar turbulence. i. retrieval of velocity field statistics. *ApJ*, 566(1):276, 2002.

Blakesley Burkhart and A Lazarian. The column density variance-relationship. *ApJ Letters*, 755(1):L19, 2012.

Blakesley Burkhart and Alex Lazarian. The phase coherence of interstellar density fluctuations. *arXiv preprint arXiv:1511.03660*, 2015.

Blakesley Burkhart, D Falceta-Gonçalves, G Kowal, and A Lazarian. Density studies of mhd interstellar turbulence: statistical moments, correlations and bispectrum. *ApJ*, 693(1):250, 2009.

Blakesley Burkhart, A Lazarian, Alyssa Goodman, and Erik Rosolowsky. Hierarchical structure of magnetohydrodynamic turbulence in position-position-velocity space. *ApJ*, 770(2):141, 2013.

Blakesley Burkhart, A Lazarian, IC Leão, JR De Medeiros, and A Esquivel. Measuring the alfvénic nature of the interstellar medium: Velocity anisotropy revisited. *ApJ*, 790(2):130, 2014.

Blakesley Burkhart, A Lazarian, D Balsara, C Meyer, and J Cho. Alfvénic turbulence beyond the ambipolar diffusion scale. *ApJ*, 805(2):118, 2015.

Robert R Caldwell, Chris Hirata, and Marc Kamionkowski. Dust-polarization maps and interstellar turbulence. *The Astrophysical Journal*, 839(2):91, 2017.

Subrahmanyan Chandrasekhar. The theory of axisymmetric turbulence. *Philosophical Transactions of the Royal Society of London A: Mathematical, Physical and Engineering Sciences*, 242(855):557–577, 1950.

A Chepurnov and A Lazarian. Turbulence spectra from doppler-broadened spectral lines: tests of the velocity channel analysis and velocity coordinate spectrum techniques. *ApJ*, 693(2):1074, 2009.

A Chepurnov and A Lazarian. Extending the big power law in the sky with turbulence spectra from wisconsin hα mapper data. *ApJ*, 710(1):853, 2010.

A. Chepurnov, J. Gordon, A. Lazarian, and S. Stanimirovic. Topology of Neutral Hydrogen within the Small Magellanic Cloud. *ApJ*, 688:1021-1028, December 2008. doi: 10.1086/591655.

A Chepurnov, J Gordon, A Lazarian, and S Stanimirovic. Topology of neutral hydrogen within the small magellanic cloud. *The Astrophysical Journal*, 688 (2):1021, 2008.

Jungyeon Cho and A Lazarian. Compressible magnetohydrodynamic turbulence: mode coupling, scaling relations, anisotropy, viscosity-damped regime and astrophysical implications. *MNRAS*, 345(1):325–339, 2003.

Jungyeon Cho and Alex Lazarian. Compressible sub-alfvénic mhd turbulence in low-β plasmas. *Physical Review Letters*, 88(24):245001, 2002.

Jungyeon Cho and Alex Lazarian. Generation of compressible modes in mhd turbulence. *Theoretical and Computational Fluid Dynamics*, 19(2):127–157, 2005.

Jungyeon Cho and Ethan T Vishniac. The anisotropy of magnetohydrodynamic alfvénic turbulence. *ApJ*, 539(1):273, 2000.

Jungyeon Cho, Alex Lazarian, and Ethan T Vishniac. Simulations of magnetohydrodynamic turbulence in a strongly magnetized medium. *ApJ*, 564(1): 291, 2002.

C. Correia, A. Lazarian, B. Burkhart, D. Pogosyan, and J. R. De Medeiros. Principal component analysis studies of turbulence in optically thick gas. *ApJ*, 818(2):118, 2016. URL `http://stacks.iop.org/0004-637X/818/i=2/a=118`.

AA Deshpande, KS Dwarakanath, and W Ml Goss. Power spectrum of the density of cold atomic gas in the galaxy toward cassiopeia a and cygnus a. *The Astrophysical Journal*, 543(1):227, 2000.

Bruce T Draine. *Physics of the interstellar and intergalactic medium*. Princeton University Press, 2010.

Bruce G Elmegreen and John Scalo. Interstellar turbulence i: observations and processes. *arXiv preprint astro-ph/0404451*, 2004.

A Esquivel and A Lazarian. Tsallis statistics as a tool for studying interstellar turbulence. *ApJ*, 710(1):125, 2010.

A Esquivel, A Lazarian, S Horibe, J Cho, V Ossenkopf, and J Stutzki. Statistics of velocity centroids: effects of density–velocity correlations and non-gaussianity. *MNRAS*, 381(4):1733–1744, 2007.

A Esquivel, A Lazarian, and D Pogosyan. Studying the interstellar magnetic field from anisotropies in velocity channels. *ApJ*, 814(1):77, 2015.

Alejandro Esquivel and A Lazarian. Velocity centroids as tracers of the turbulent velocity statistics. *ApJ*, 631(1):320, 2005.

Alejandro Esquivel and Alex Lazarian. Velocity anisotropy as a diagnostic of the magnetization of the interstellar medium and molecular clouds. *ApJ*, 740 (2):117, 2011.

Alejandro Esquivel, A Lazarian, D Pogosyan, and Jungyeon Cho. Velocity statistics from spectral line data: effects of densityvelocity correlations, magnetic field and shear. *MNRAS*, 342(1):325–336, 2003.

C. Federrath. On the universality of supersonic turbulence. *MNRAS*, 436: 1245–1257, December 2013. doi: 10.1093/mnras/stt1644.

Christoph Federrath. On the universality of interstellar filaments: theory meets simulations and observations. *MNRAS*, 457(1):375–388, 2016.

Christoph Federrath, Ralf S Klessen, and Wolfram Schmidt. The density probability distribution in compressible isothermal turbulence: Solenoidal versus compressive forcing. *ApJ Letters*, 688(2):L79, 2008.

Christoph Federrath, Ralf S Klessen, and Wolfram Schmidt. The fractal density structure in supersonic isothermal turbulence: solenoidal versus compressive energy injection. *ApJ*, 692(1):364, 2009.

Christoph Federrath, J Roman-Duval, RS Klessen, Wolfgang Schmidt, and M-M Mac Low. Comparing the statistics of interstellar turbulence in simulations and observations-solenoidal versus compressive turbulence forcing. *A&A*, 512:A81, 2010.

P Goldreich and S Sridhar. Toward a theory of interstellar turbulence. 2: Strong alfvenic turbulence. *ApJ*, 438:763–775, 1995.

Diego F González-Casanova, Alexander Lazarian, and Reinaldo Santos-Lima. Magnetic fields in early protostellar disk formation. *ApJ*, 819(2):96, 2016.

Mark Heyer, Hao Gong, Eve Ostriker, and Christopher Brunt. Magnetically aligned velocity anisotropy in the taurus molecular cloud. *ApJ*, 680(1):420, 2008.

Mark H Heyer and F Peter Schloerb. Application of principal component analysis to large-scale spectral line imaging studies of the interstellar medium. *ApJ*, 475(1):173, 1997.

JC Higdon. Density fluctuations in the interstellar medium: Evidence for anisotropic magnetogasdynamic turbulence. i-model and astrophysical sites. *ApJ*, 285:109–123, 1984.

Padraig Houlahan and John Scalo. Recognition and characterization of hierarchical interstellar structure. ii-structure tree statistics. *ApJ*, 393:172–187, 1992.

Norio Ikeda, Kazuyoshi Sunada, and Yoshimi Kitamura. A survey of dense cores in the orion a cloud. *ApJ*, 665(2):1194, 2007.

PC Jain and Prem Kumar. The fluctuations of density in axisymmetric turbulence. *Proc. Nat. Int. of India*, 28, 1961.

D. Kandel, A. Lazarian, and D. Pogosyan. Extending velocity channel analysis for studying turbulence anisotropies. *MNRAS*, 461(2):1227–1259, 2016a. URL `http://mnras.oxfordjournals.org/content/461/2/1227.abstract`.

D Kandel, A Lazarian, and D Pogosyan. Study of velocity centroids based on the theory of fluctuations in position–position–velocity space. *Monthly Notices of the Royal Astronomical Society*, 464(3):3617–3635, 2016b.

D Kandel, A Lazarian, and D Pogosyan. Effects of dust absorption on spectroscopic studies of turbulence. *Monthly Notices of the Royal Astronomical Society*, 2017a.

D Kandel, A Lazarian, and D Pogosyan. Ratio of e to b mode power for galactic foreground. *arXiv preprint arXiv:1707.06276*, 2017b.

SC Kleiner and RL Dickman. Large-scale structure of the taurus molecular complex. ii-analysis of velocity fluctuations and turbulence. iii-methods for turbulence. *ApJ*, 295:466–484, 1985.

Eric W Koch, Caleb G Ward, Stella Offner, Jason L Loeppky, and Erik W Rosolowsky. Identifying tools for comparing simulations and observations of spectral-line data cubes. *Monthly Notices of the Royal Astronomical Society*, 2017.

Lukas Konstandin, Christoph Federrath, Ralf S Klessen, and Wolfram Schmidt. Statistical properties of supersonic turbulence in the lagrangian and eulerian frameworks. *Journal of Fluid Mechanics*, 692:183–206, 2012.

G Kowal, A Lazarian, and A Beresnyak. Density fluctuations in mhd turbulence: spectra, intermittency, and topology. *ApJ*, 658(1):423, 2007.

Grzegorz Kowal and A Lazarian. Velocity field of compressible magnetohydrodynamic turbulence: wavelet decomposition and mode scalings. *ApJ*, 720 (1):742, 2010.

A. Lazarian. Astrophysical Implications of Turbulent Reconnection: from cosmic rays to star formation. In E. M. de Gouveia dal Pino, G. Lugones, and A. Lazarian, editors, *Magnetic Fields in the Universe: From Laboratory and Stars to Primordial Structures.*, volume 784 of *American Institute of Physics Conference Series*, pages 42–53, September 2005. doi: 10.1063/1.2077170.

A Lazarian. Enhancement and suppression of heat transfer by mhd turbulence. *ApJ Letters*, 645(1):L25, 2006.

A. Lazarian. Obtaining Spectra of Turbulent Velocity from Observations. *SSR*, 143:357–385, March 2009.

A Lazarian. Reconnection diffusion in turbulent fluids and its implications for star formation. *Space Science Reviews*, 181(1-4):1–59, 2014.

A Lazarian and Alejandro Esquivel. Statistics of velocity from spectral data: modified velocity centroids. *ApJ Letters*, 592(1):L37, 2003.

A Lazarian and D Pogosyan. Velocity modification of the power spectrum from an absorbing medium. *ApJ*, 616(2):943, 2004.

A Lazarian and D Pogosyan. Studying turbulence using doppler-broadened lines: velocity coordinate spectrum. *ApJ*, 652(2):1348, 2006.

A Lazarian and D Pogosyan. Studying velocity turbulence from doppler-broadened absorption lines: statistics of optical depth fluctuations. *ApJ*, 686(1):350, 2008.

A. Lazarian and D. Pogosyan. Spectrum and anisotropy of turbulence from multi-frequency measurement of synchrotron polarization. *ApJ*, 818(2):178, 2016.

A Lazarian and Ethan T Vishniac. Reconnection in a weakly stochastic field. *ApJ*, 517(2):700, 1999.

A Lazarian and Huirong Yan. Superdiffusion of cosmic rays: implications for cosmic ray acceleration. *ApJ*, 784(1):38, 2014.

A Lazarian, D Pogosyan, and A Esquivel. Seeing through the dust: The detection of hi and the exploration of the ism in galaxies (asp conf. proc. 276), ed. *AR Taylor, TL Landecker, & AG Willis (San Francisco, CA: ASP)*, 182, 2002.

A Lazarian, A Esquivel, and R Crutcher. Magnetization of cloud cores and envelopes and other observational consequences of reconnection diffusion. *ApJ*, 757(2):154, 2012.

Alex Lazarian and Dmitri Pogosyan. Statistical description of synchrotron intensity fluctuations: studies of astrophysical magnetic turbulence. *ApJ*, 747(1):5, 2012.

Alex Lazarian, Dmitri Pogosyan, Enrique Vázquez-Semadeni, and Bárbara Pichardo. Emissivity statistics in turbulent compressible magnetohydrodynamic flows and the density-velocity correlation. *ApJ*, 555(1):130, 2001.

Alex Lazarian, G Eyink, E Vishniac, and Grzegorz Kowal. Turbulent reconnection and its implications. *Philosophical Transactions of the Royal Society*

of London A: Mathematical, Physical and Engineering Sciences, 373(2041): 20140144, 2015.

Alexander Lazarian and Dmitry Pogosyan. Velocity modification of hi power spectrum. *ApJ*, 537(2):720, 2000.

MRM Leão, EM de Gouveia Dal Pino, R Santos-Lima, and A Lazarian. The collapse of turbulent cores and reconnection diffusion. *ApJ*, 777(1):46, 2013.

Pak Shing Li, Christopher F McKee, and Richard I Klein. Magnetized interstellar molecular clouds–i. comparison between simulations and zeeman observations. *Monthly Notices of the Royal Astronomical Society*, 452(3): 2500–2527, 2015.

Yoram Lithwick and Peter Goldreich. Compressible magnetohydrodynamic turbulence in interstellar plasmas. *ApJ*, 562(1):279, 2001.

Mordecai-Mark Mac Low and Ralf S Klessen. Control of star formation by supersonic turbulence. *Reviews of modern physics*, 76(1):125, 2004.

Jason Maron and Peter Goldreich. Simulations of incompressible magnetohydrodynamic turbulence. *ApJ*, 554(2):1175, 2001.

J. Mathews and R.L. Walker. *Mathematical Methods of Physics*. Addison-Wesley World Student Series. W. A. Benjamin, 1970. ISBN 9780805370027.

C. F. McKee and E. C. Ostriker. Theory of Star Formation. *ARRA*, 45:565–687, September 2007. doi: 10.1146/annurev.astro.45.051806.110602.

Mark S Miesch and John Bally. Statistical analysis of turbulence in molecular clouds. *ApJ*, 429:645–671, 1994.

Mark S Miesch, John Scalo, and John Bally. Velocity field statistics in star-forming regions. i. centroid velocity observations. *ApJ*, 524(2):895, 1999.

Kazuhisa Mitsuda, Richard L Kelley, Hiroki Akamatsu, Thomas Bialas, Kevin R Boyce, Gregory V Brown, Edgar Canavan, Meng Chiao, Elisa Costantini, Jan-Willem den Herder, et al. Soft x-ray spectrometer (sxs): the high-resolution cryogenic spectrometer onboard astro-h. In *Proc. SPIE*, volume 9144, page 91442A, 2014.

M-A Miville-Deschênes, G Joncas, E Falgarone, and F Boulanger. High resolution 21 cm mapping of the ursa major galactic cirrus: Power spectra of the high-latitude hi gas. *Astronomy & Astrophysics*, 411(2):109–121, 2003.

M-A Miville-Deschênes, PG Martin, A Abergel, J-P Bernard, F Boulanger, G Lagache, LD Anderson, P André, H Arab, J-P Baluteau, et al. Herschel-spire observations of the polaris flare: Structure of the diffuse interstellar medium at the sub-parsec scale. *Astronomy & Astrophysics*, 518:L104, 2010.

Andrei S. Monin, A. M. Yaglom, and J. L. Lumley, editors. *Statistical Fluid Mechanics: Mechanics of Turbulence, Vol. 2*. The MIT Press, first english ed. edition, 4 1975. ISBN 9780262130981. URL `http://amazon.com/o/ASIN/026213098X/`.

David Montgomery and Leaf Turner. Anisotropic magnetohydrodynamic turbulence in a strong external magnetic field. *Physics of Fluids*, 24(5):825–831, 1981. doi: http://dx.doi.org/10.1063/1.863455. URL `http://scitation.aip.org/content/aip/journal/pof1/24/5/10.1063/1.863455`.

G Münch. Internal motions in the orion nebula. *Reviews of Modern Physics*, 30(3):1035, 1958.

G Münch and Albert D Wheelon. Space-time correlations in stationary isotropic turbulence. *Physics of Fluids (1958-1988)*, 1(6):462–468, 1958.

Ramesh Narayan and Mikhail V Medvedev. Thermal conduction in clusters of galaxies. *ApJ Letters*, 562(2):L129, 2001.

CR O'dell and Hector O Castaneda. Evidence for turbulence in h ii regions. *ApJ*, 317:686–692, 1987.

V Ossenkopf, M Krips, and J Stutzki. Structure analysis of interstellar clouds-i. improving the δ-variance method. *A&A*, 485(3):917–929, 2008.

J. E. Pineda, P. Caselli, A. A. Goodman, E. Rosolowsky, and J. B. Foster. The COMPLETE Calibration of 12CO and 13CO in Perseus. In *American Astronomical Society Meeting Abstracts*, volume 38 of *Bulletin of the American Astronomical Society*, page 968, December 2006.

IG Plunkett and GC Jain. Three generalised negative binomial distributions. *Biometrische Zeitschrift*, 17(5):286–302, 1975.

Julia Roman-Duval, Christoph Federrath, Christopher Brunt, Mark Heyer, James Jackson, and Ralf S Klessen. The turbulence spectrum of molecular clouds in the galactic ring survey: A density-dependent principal component analysis calibration. *ApJ*, 740(2):120, 2011.

Erik W Rosolowsky, Alyssa A Goodman, David J Wilner, and Jonathan P Williams. The spectral correlation function: A new tool for analyzing spectral line maps. *ApJ*, 524(2):887, 1999.

EW Rosolowsky, JE Pineda, J Kauffmann, and AA Goodman. Structural analysis of molecular clouds: dendrograms. *ApJ*, 679(2):1338, 2008.

R Santos-Lima, A Lazarian, EM de Gouveia Dal Pino, and J Cho. Diffusion of magnetic field and removal of magnetic flux from clouds via turbulent reconnection. *ApJ*, 714(1):442, 2010.

R Santos-Lima, EM de Gouveia Dal Pino, Grzegorz Kowal, D Falceta-Gonçalves, A Lazarian, and MS Nakwacki. Magnetic field amplification and evolution in turbulent collisionless magnetohydrodynamics: An application to the intracluster medium. *ApJ*, 781(2):84, 2014.

R. Schlickeiser. *Cosmic Ray Astrophysics*. 2002.

John V Shebalin, William H Matthaeus, and David Montgomery. Anisotropy in mhd turbulence due to a mean magnetic field. *Journal of Plasma Physics*, 29(03):525–547, 1983.

Rowan J Smith, Simon CO Glover, and Ralf S Klessen. On the nature of star-forming filaments–i. filament morphologies. *MNRAS*, 445(3):2924–2941, 2014.

Lyman Spitzer Jr. *Physical processes in the interstellar medium*. John Wiley & Sons, 2008.

J Stutzki, F Bensch, A Heithausen, V Ossenkopf, and M Zielinsky. On the fractal structure of molecular clouds. *Astronomy and Astrophysics*, 336:697–720, 1998.

Jürgen Stutzki and Rolf Guesten. High spatial resolution isotopic co and cs observations of m17 sw-the clumpy structure of the molecular cloud core. *ApJ*, 356:513–533, 1990.

Benjamin M Tofflemire, Blakesley Burkhart, and A Lazarian. Interstellar sonic and alfvenic mach numbers and the tsallis distribution. *ApJ*, 736(1):60, 2011.

Jonathan P Williams, Eugene J De Geus, and Leo Blitz. Determining structure in molecular clouds. *ApJ*, 428:693–712, 1994.

Huirong Yan and A Lazarian. Cosmic-ray scattering and streaming in compressible magnetohydrodynamic turbulence. *ApJ*, 614(2):757, 2004.

Huirong Yan and A Lazarian. Cosmic-ray propagation: nonlinear diffusion parallel and perpendicular to mean magnetic field. *ApJ*, 673(2):942, 2008.

Huirong Yan and Alex Lazarian. Scattering of cosmic rays by magnetohydrodynamic interstellar turbulence. *Physical review letters*, 89(28):281102, 2002.

Appendix A

Turbulence Statistics in PPV Space

Below we present the main expressions of the theory that we are going to use within our study.

The transformation between real space and PPV space is of the form $(\mathbf{X}, z) \rightarrow (\mathbf{X}, v)$ where v is the LOS velocity of the gas element. The PPV density $\rho_s(\mathbf{X}, v)$ is dependent on both density of the gas in the real space and its velocity, and is written as (LP04)

$$\rho_s(\mathbf{X}, v) = \int_0^S \mathrm{d}z \rho(\mathbf{x}) \Phi_v(v, \mathbf{x}), \tag{A.1}$$

where S is spatial extent of the turbulent cloud and Φ_v is the Maxwell distribution of the thermal component of the turbulent particles defined by

$$\Phi_v(v, \mathbf{x}) = \frac{1}{\sqrt{2\pi\beta_{\mathrm{T}}}} \exp\left[-\frac{(v - u(\mathbf{x}))^2}{2\beta_{\mathrm{T}}}\right], \tag{A.2}$$

where $u(\mathbf{x})$ is the non-thermal velocity of a particle at position $\mathbf{x}$ which consists of the contribution of turbulent velocity as coherent velocity with the gas cloud. If the gas is isolated, and coherent motions are negligible, as we adopt in

this paper, u is the LOS component of the turbulent motion, and $\beta_{\rm T}$ is the temperature parameter.

Intensity of radiation in an optically thin line is proportional to the 'density of emitters' of PPV space. This density is the result of the velocity mapping of emitters from XYZ to XYV space and is, in general, significantly different from the real space density. To describe statistical properties of PPV density, we use the correlation

$$\xi_s(R,\phi,v_1,v_2) \equiv \langle \rho_s(\mathbf{X}_1,v_1)\rho_s(\mathbf{X}_2,v_2)\rangle, \tag{A.3}$$

or structure

$$d_s(R,\phi,v_1,v_2) = \left\langle \left(\rho_s(\mathbf{X}_1,v_1)-\rho_s(\mathbf{X}_2,v_2)\right)^2\right\rangle, \tag{A.4}$$

functions, where, in contrast to LP00 we take into account the dependence of the correlations on the angle ϕ of the separation vector $\mathbf{R}=\mathbf{X}_1-\mathbf{X}_2$. between the two LOS,

The averaging is performed over realizations of two random fields turbulent velocity $\mathbf{u}$ and real space density ρ of the emitters. Statistical properties of these quantities reflect the properties of the magnetized turbulent processes.

The turbulent velocity field is assumed to be described by the Gaussian two point probability distribution function (LP00)

$$P(u_1,u_2) = \frac{1}{\pi\sqrt{2D_z(\infty)-D_z(\mathbf{r})}\sqrt{D_z(\mathbf{r})}}\exp\left[-\frac{u^2}{2D_z(\mathbf{r})}\right] \exp\left[-\frac{u_+^2}{D_z(\infty)-D_z(\mathbf{r})/2}\right], \tag{A.5}$$

where $u_1=u_z(\mathbf{r}_1),\ldots$ and $u=u_1-u_2$, $u_+=(u_1+u_2)/2$.

No assumptions about Gaussianity of the density inhomogeneities of the sources are made. We introduce density correlation function $\xi(\mathbf{r}) \equiv \langle \rho(\mathbf{x}_1)\rho(\mathbf{x}_2)\rangle$

whose properties are to be determined or modelled. Splitting the density into the mean value and fluctuations, $\rho = \langle\rho\rangle + \delta\rho$, we have $\xi(\mathbf{r}) = \langle\rho\rangle^2 + \langle\delta\rho(\mathbf{x}_1)\delta\rho(\mathbf{x}_2)\rangle = \langle\rho\rangle^2 + \tilde{\xi}(r)$. For specific calculations, we consider two distinct cases. If density perturbations have a *shallow* power spectrum, $\langle\delta\rho_k^2\rangle \propto k^{-3+\nu_\rho}$, $\nu_\rho > 0$, the correlation function is modelled as

$$\xi(\mathbf{r}) = \langle\rho\rangle^2 + \langle\delta\rho^2\rangle \frac{r_c^{\nu_\rho}}{r_c^{\nu_\rho} + r^{\nu_\rho}} \approx \langle\rho\rangle^2 + \langle\delta\rho^2\rangle \left(r_c/r\right)^{\nu_\rho} \ , \ r > r_c \tag{A.6}$$

while if the power spectrum is steep, $\nu_\rho < 0$, the density correlation function is

$$\xi(\mathbf{r}) = \langle\rho\rangle^2 + \langle\delta\rho^2\rangle \frac{r_c^{-\nu_\rho}}{r_c^{-\nu_\rho} + r^{-\nu_\rho}} \approx \langle\rho\rangle^2 + \langle\delta\rho^2\rangle - \langle\delta\rho^2\rangle \left(r/r_c\right)^{-\nu_\rho} \ , \tag{A.7}$$

for $r < r_c$. The difference between the two cases is that for *shallow* density, the scaling range lies at separations exceeding the correlation length, $r > r_c$, with r_c associated with short scale damping, while for *steep* density it lies at separations shorter than the correlation length, $r < r_c$, which is now associated with the largest energy injection scale. Eq. [A.7] shows that for the *steep* spectrum, scale dependent part of the correlation function is always subdominant to the constant $\langle\rho\rangle^2 + \langle\delta\rho^2\rangle = \langle\rho^2\rangle$.

Using Eq. (A.1) and Eq. (A.5), it can be shown that (see LP04)

$$\begin{aligned}\xi_s(\mathbf{r},v_1,v_2) \approx & \frac{S}{\sqrt{D_z(\infty)+\beta_{\rm T}}} \exp\left[-\frac{v_+^2}{D_z(\infty)+\beta_{\rm T}}\right] \\ & \int_{-S}^{S} {\rm d}z \left(1-\frac{|z|}{S}\right) \frac{\langle\rho\rangle^2 + \tilde{\xi}(\mathbf{r})}{\sqrt{D_z(\mathbf{r})+2\beta_{\rm T}}} \exp\left[-\frac{v^2}{2(D_z(\mathbf{r})+2\beta_{\rm T})}\right].\end{aligned} \tag{A.8}$$

under the assumption that density fluctuations are uncorrelated with the turbulent velocities. The arguments can be found in LP00, but importantly this assumption has been checked in numerical MHD simulations (Esquivel et al., 2003) and has been found to hold with sufficient accuracy.

The first exponential term reflects the amplitude of correlation depending

on the value of the central velocity v_+ relative to the variance of the turbulent velocities $D(\infty)/2$. The LOS integral term reflects the statistics of the turbulence at different separation scales $\mathbf{R}$ and velocity differences v.

Since density correlation function has a constant term, there are non-trivial correlations in PPV cube even for uniform density of emitters. They arise from different velocities of the emitters. Thus in our discussion we split the PPV correlations into *velocity* and *density* contributions

$$\tilde{\xi}_s(\mathbf{R},\phi,v) = \tilde{\xi}_v(\mathbf{R},\phi,v) + \tilde{\xi}_\rho(\mathbf{R},\phi,v), \tag{A.9}$$

where

$$\tilde{\xi}_v(\mathbf{R},\phi,v) \propto \int_{-S}^{S} \mathrm{d}z \frac{\bar{\rho}^2(\mathbf{r})}{\sqrt{D_z(\mathbf{r})}} \exp\left[-\frac{v^2}{2D_z(\mathbf{r})}\right], \tag{A.10}$$

and

$$\tilde{\xi}_\rho(\mathbf{R},\phi,v) \propto \int_{-S}^{S} \mathrm{d}z \frac{\tilde{\xi}(\mathbf{r})}{\sqrt{D_z(\mathbf{r})}} \exp\left[-\frac{v^2}{2D_z(\mathbf{r})}\right]. \tag{A.11}$$

In these expressions we have omitted for brevity the thermal effects and the finite cloud size effects. We should stress that although *density* correlation contribution is zero when the gas density is uniform, it depends on both density and velocity fluctuations when gas distribution is inhomogeneous.

This theory for PPV correlations allows for angular dependence of the correlation functions ξ and D_z. Consequently, after the integration over z the anisotropic dependence on polar angle ϕ is still allowed. This allows us, in what follows, to use whole machinery developed in our earlier works to deal with the anisotropic turbulence.

Let us turn to the quantity that can be measured in the observations. The measured intensity of radiation in a velocity channel of width Δv, centred at velocty v_i is given by the integral

$$I(\mathbf{R},v_i) = \epsilon \int_{v_i-\Delta v/2}^{v_i+\Delta v/2} dv_1 \rho_s(\mathbf{R},v_1). \tag{A.12}$$

With this, it can be shown that the intensity correlation function is (LP04)

$$\xi_{\rm I}(\mathbf{R},\Delta v) \propto \frac{\epsilon^2\bar{\rho}^2}{2\pi}\int_{-S}^{S}{\rm d}z\,\frac{1+\tilde{\xi}_s(\mathbf{r})}{D_z^{1/2}(\mathbf{r})} \int_{-\infty}^{\infty}{\rm d}v\,W_i(v,\Delta v,\beta_{\rm T})\exp\left[-\frac{v^2}{2D_z(\mathbf{r})}\right], \tag{A.13}$$

where $W_i(v,\Delta v,\beta)$ is a composite window of channel i. Its properties are such that for zero temperature $\beta_{\rm T}=0$ its width is bounded by Δv, but for high temperature $\beta_{\rm T}>\Delta v^2$ it is given by the thermal width $\beta_{\rm T}$. Thus, thermal broadening sets the minimal effective channel width. In LP00 we have shown the importance of distinction between *thin* and *thick* channels. The criterion is set by comparison of characteristic velocity difference at the scale of separation between the LOS, $\sqrt{D(R)}$ and the channel width Δv. In *thin* channels such difference is resolved $\Delta v<\sqrt{D_z(R)}$, while in *thick* it is not, $\Delta v>\sqrt{D_z(R)}$. Thus in a *thin* channel velocity differences along the LOS within the channel can be neglected, $v=0$ leaving intensity correlations to be sensitive both to density and velocity differences between the LOS,

$$\xi_{\rm I}(\mathbf{R},\Delta v) \propto \frac{\epsilon^2\bar{\rho}^2}{2\pi}\int_{-S}^{S}{\rm d}z\,\frac{1+\tilde{\xi}_s(\mathbf{r})}{D_z^{1/2}(\mathbf{r})}\,. \tag{A.14}$$

In contrast, in *thick* channels, velocities are integrated over, leaving only density inhomogeneities as the source of intensity fluctuations

$$\xi_{\rm I}(\mathbf{R},\Delta v) \propto \frac{\epsilon^2\bar{\rho}^2}{2\pi}\int_{-S}^{S}{\rm d}z\left[1+\tilde{\xi}_s(\mathbf{r})\right]. \tag{A.15}$$

We note that *thick* slicing can be obtained synthetically, by adding intensities (before computing the correlations) for adjacent thinner channels. Our ability to have *thin* velocity channels is limited by the instrument spectral resolution and the thermal broadening.

Appendix B

General Approach To Find Velocity Correlation In Real Space

The velocity correlation tensor in the axisymmetric case in Fourier space is

$$\langle v_i(\mathbf{k}) v_j^*(\mathbf{k}') \rangle = \mathcal{A}(k, \hat{\mathbf{k}} \cdot \hat{\lambda}) \left(\hat{\xi}_{\mathbf{k}} \otimes \hat{\xi}_{\mathbf{k}}^* \right)_{ij}, \tag{B.1}$$

where $\mathcal{A}(k, \hat{\mathbf{k}} \cdot \hat{\lambda})$ is the power spectrum and $\left(\hat{\xi}_{\mathbf{k}} \otimes \hat{\xi}_{\mathbf{k}}^* \right)_{ij}$ is a $\hat{\lambda}$-dependent tensor build from the displacement direction characteristic for the given mode. Correspondingly, in real space the velocity correlation function can be written as

$$\langle v_i(\mathbf{x}_1) v_j(\mathbf{x}_1 + \mathbf{r}) \rangle = \int \mathrm{d}k \, k^2 \, \mathrm{d}\Omega_k \, \mathrm{e}^{i\mathbf{k}\cdot\mathbf{r}} \mathcal{A}(k, \hat{\mathbf{k}} \cdot \hat{\lambda}) \left(\hat{\xi}_{\mathbf{k}} \otimes \hat{\xi}_{\mathbf{k}}^* \right)_{ij}. \tag{B.2}$$

The power spectrum can be represented in terms of spherical harmonics as

$$\mathcal{A}(k, \hat{\mathbf{k}} \cdot \hat{\lambda}) = \sum_{\ell_1 m_1} \frac{4\pi}{2\ell_1 + 1} \mathcal{A}_{\ell_1}(k) Y_{\ell_1 m_1}(\hat{\mathbf{k}}) Y_{\ell_1 m_1}^*(\hat{\lambda}), \tag{B.3}$$

and similarly

$$\left(\hat{\xi}_{\mathbf{k}} \otimes \hat{\xi}^{*}_{\mathbf{k}}\right)_{ij} = \sum_{\ell_2 m_2} c^{ij}_{\ell_2 m_2}(\hat{\lambda}) Y_{\ell_2 m_2}(\hat{\mathbf{k}}) \ , \tag{B.4}$$

Using well-known representation for the plane wave

$$\mathrm{e}^{i\mathbf{k}.\mathbf{r}} = 4\pi \sum_{\ell m} i^{\ell} j_{\ell}(kr) Y_{\ell m}(\hat{\mathbf{k}}) Y^{*}_{\ell m}(\hat{\mathbf{r}}). \tag{B.5}$$

we obtain

$$\begin{aligned}\langle v_i v_j \rangle = \sum_{\ell m} 4\pi i^{\ell} Y^{*}_{\ell m}(\hat{\mathbf{r}}) \sum_{\ell_1 m_1} \frac{4\pi}{2\ell_1 + 1} Y^{*}_{\ell_1 m_1}(\hat{\lambda}) \sum_{\ell_2 m_2} c^{ij}_{\ell_2 m_2}(\hat{\lambda}) \\ \int \mathrm{d}k\, k^2\, \mathrm{d}\Omega_k\, j_{\ell}(kr) \mathcal{A}_{\ell_1}(k) Y_{\ell m}(\hat{\mathbf{k}}) Y_{\ell_1 m_1}(\hat{\mathbf{k}}) Y_{\ell_2 m_2}(\hat{\mathbf{k}})\end{aligned} \tag{B.6}$$

Defining

$$\mathcal{T}_{\ell \ell_1}(r) = \int \mathrm{d}k\, k^2 j_{\ell}(kr) \mathcal{A}_{\ell_1}(k) \tag{B.7}$$

and the symbol Ψ that can be represented in terms of Wigner-3j symbols

$$\Psi_{\ell m, \ell_1 m_1, \ell_2 m_2} = \int \mathrm{d}\Omega_k Y_{\ell m}(\theta_k, \phi_k) Y_{\ell_1 m_1}(\theta_k, \phi_k) Y_{\ell_2 m_2}(\theta_k, \phi_k) \tag{B.8}$$

$$\begin{aligned}\Psi_{\ell m, \ell_1 m_1, \ell_2 m_2} = \sqrt{\frac{(2\ell+1)(2\ell_1+1)(2\ell_2+1)}{4\pi}} \begin{pmatrix} \ell & \ell_1 & \ell_2 \\ 0 & 0 & 0 \end{pmatrix} \\ \begin{pmatrix} \ell & \ell_1 & \ell_2 \\ m & m_1 & m_2 \end{pmatrix}\end{aligned} \tag{B.9}$$

we arrive at a suitable for further analysis form for the correlation tensor

$$\begin{aligned}\langle v_i v_j \rangle = \sum_{\ell m} 4\pi i^{\ell} Y^{*}_{\ell m}(\hat{\mathbf{r}}) \sum_{\ell_1 m_1} \frac{4\pi}{2\ell_1 + 1} Y^{*}_{\ell_1 m_1}(\hat{\lambda}) \\ \sum_{\ell_2 m_2} c^{ij}_{\ell_2 m_2}(\hat{\lambda}) \mathcal{T}_{\ell \ell_1}(r) \Psi_{\ell m, \ell_1 m_1, \ell_2 m_2} \ .\end{aligned} \tag{B.10}$$

For this expression, we will derive A_ξ, B_ξ, C_ξ and D_ξ (cf. Eq.(2.6)). We develop the following procedure to find these coefficients. Using the fact that A_ξ, B_ξ, C_ξ and D_ξ are invariant under rotation of coordinate frame, as these coefficients depend only on $\mu \equiv \hat{\mathbf{r}} \cdot \hat{\lambda}$, we shall work in $\hat{\lambda} = \hat{\mathbf{z}}$ frame. In this frame, Eq. (B.10) is simplified to

$$\langle v_i v_j \rangle = \sum_{\ell m} 4\pi i^\ell (-1)^m Y_{\ell m}(\hat{\mathbf{r}}) \sum_{\ell_1} \sqrt{\frac{4\pi}{2\ell_1+1}} \sum_{\ell_2} c^{ij}_{\ell_2 m}(\hat{\mathbf{z}}) \mathcal{T}_{\ell\ell_1}(r) \Psi_{\ell(-m),\ell_1 0,\ell_2 m} \ . \tag{B.11}$$

where we have used the fact that Wigner-3j symbols vanish for $m+m_1+m_2 \neq 0$ and the relation $Y^*_{\ell(-m)}(\hat{\mathbf{r}}) = (-1)^m Y_{\ell m}(\hat{\mathbf{r}})$. We also note that $c^{ij}_{\ell_2 m}(\hat{\mathbf{z}})$ are non-zero only for $|m| \leq 2$ (since they are the multipole expansion of a direct square of a vector, we shall see this in explicit calculations further on). For an isotropic power spectrum, only $\ell_1 = 0$ survives and therefore Eq.(B.11) becomes

$$\langle v_i v_j \rangle = \sum_{\ell m} 4\pi i^\ell Y_{\ell m}(\hat{\mathbf{r}}) c^{ij}_{\ell m}(\hat{\mathbf{z}}) \mathcal{T}_{\ell 0}(r). \tag{B.12}$$

As the first step of calculations, we take $\langle v_1 v_2 \rangle$ which in $\hat{\lambda} = \hat{\mathbf{z}}$ frame has simple form $\langle v_1 v_2 \rangle = A(r, \cos\theta)\hat{\mathbf{r}}_1 \hat{\mathbf{r}}_2 = A(r, \cos\theta) \sin^2\theta \cos\phi \sin\phi$, and use this to find $A(r, \cos\theta)$. Since the expression obtained for A should be valid in all frames, we replace $\cos\theta \to \mu$ to arrive to the frame-independent $A(r, \mu)$. Next, we take $\langle v_1 v_1 \rangle = A\hat{\mathbf{r}}_1 \hat{\mathbf{r}}_1 + B$, and repeat the procedure selecting factor A as what is proportional to $\sin^2\theta \cos^2\phi$, with the remainder being B. After that, we take $\langle v_1 v_2 \rangle = A\hat{\mathbf{r}}_1 \hat{\mathbf{r}}_3 + D\hat{\mathbf{r}}_1$ and repeat the procedure by factoring out $\sin\theta\cos\theta\cos\phi$ component and looking for the remainder, which is $D\sin\theta\cos\phi$. Finally, we take $\langle v_3 v_3 \rangle = A\hat{\mathbf{r}}_3 \hat{\mathbf{r}}_3 + B + C + 2D\hat{\mathbf{r}}_3$ and use the previously found coefficients A, B and D to obtain C. This technique is applied in the subsequent sections.

Appendix C

Velocity Correlation Tensor For Different Turbulent Modes

With the technique developed in Appendix [B], it is straightforward exercise to obtain the coefficients A, B, C and D of the velocity correlation function provided that we have information about the tensor structure of a turbulent mode. In this section, we will apply the technique developed in the previous section to find these coefficients for Alfvén mode, fast mode, slow mode and strong turbulence. During our calculation, we use the knowledge about anisotropy of power spectrum of each particular mode. The power spectrum of Alfvén mode, slow mode and strong turbulence is anisotropic, while that of fast mode is isotropic (Cho and Lazarian, 2003), and this fact will be used in our subsequent calculations.

Table C.1: Mode structure of Alfvén modes for $\hat{\lambda} = \hat{\mathbf{z}}$

$c_{\ell m}^{ij}$	*Equation* (for even ℓ)
$c_{\ell m}^{11}$	$\sqrt{\pi}\delta_{\ell 0}\delta_{m0} - \Theta(\ell-2)\sqrt{\frac{\pi(2\ell+1)(\ell-2)!}{(\ell+2)!}}(\delta_{m2}+\delta_{m,-2})$
$c_{\ell m}^{22}$	$\sqrt{\pi}\delta_{\ell 0}\delta_{m0} + \Theta(\ell-2)\sqrt{\frac{\pi(2\ell+1)(\ell-2)!}{(\ell+2)!}}(\delta_{m2}+\delta_{m,-2})$
$c_{\ell m}^{12}$	$\Theta(\ell-2)i\sqrt{\frac{\pi(2\ell+1)(\ell-2)!}{(\ell+2)!}}(\delta_{m2}-\delta_{m,-2})$
$c_{\ell m}^{i3}$	$0, \qquad i \in (1,2,3)$

C.1 Alfvén mode

The tensor structure for Alfvén mode is

$$\left(\hat{\xi}_{\mathbf{k}} \otimes \hat{\xi}_{\mathbf{k}}^{*}\right)_{ij} = (\delta_{ij} - \hat{k}_i\hat{k}_j) - \frac{(\hat{k}\cdot\hat{\lambda})^2\hat{k}_i\hat{k}_j - (\hat{k}\cdot\hat{\lambda})(\hat{\lambda}_i\hat{k}_j + \hat{\lambda}_j\hat{k}_i) + \hat{\lambda}_i\hat{\lambda}_j}{1-(\hat{k}\cdot\hat{\lambda})^2}. \tag{C.1}$$

LP12 labelled the first term of the above tensor structure as E-type, and the second term as F-type. Therefore, the correlation tensor is $E-F$ type[1].

The coefficients $c_{\ell m}^{ij}$ which we shall use for the derivation of coefficients A, B, C and D are presented in Table [C.1] for $\hat{\lambda} = \hat{\mathbf{z}}$. It is important to note that $c_{\ell m}^{ij}$ is zero when ℓ is odd.

[1]LP12 obtained correlation of magnetic field, while here we are talking about correlation of velocity field. In the case of Alfvén mode, these correlations are the same, but this is in general not the case. This is because magnetic field are solenoidal, while velocity fields can be potential as well.

As a first step of our calculations, we compute

$$\langle v_1 v_2 \rangle = 4\pi \sum_{\ell \ell_1 \ell_2} i^l \sqrt{\pi(2\ell+1)}(2\ell_2+1)\sqrt{\frac{(\ell_2-2)!}{(\ell_2+2)!}}\mathcal{T}_{\ell\ell_1}(i) \begin{pmatrix} \ell & \ell_1 & \ell_2 \\ 0 & 0 & 0 \end{pmatrix} \begin{pmatrix} \ell & \ell_1 & \ell_2 \\ -2 & 0 & 2 \end{pmatrix} \left(Y_\ell^2(\hat{\mathbf{r}}) - Y_\ell^{-2}(\hat{\mathbf{r}})\right) \tag{C.2}$$

To separate $r_1 r_2 = \sin^2\theta \cos\phi \sin\phi$ factor we use the following identities of the spherical harmonics

$$Y_\ell^2(\hat{\mathbf{r}}) - Y_\ell^{-2}(\hat{\mathbf{r}}) = 4i\sqrt{\frac{(2\ell+1)(\ell-2)!}{4\pi(\ell+2)!}}\frac{P_\ell^2(\cos\theta)}{\sin^2\theta} \sin^2\theta\cos\phi\sin\phi, \tag{C.3}$$

and

$$\frac{P_\ell^2(\cos\theta)}{\sin^2\theta} = \frac{\partial^2 P_\ell(\cos\theta)}{\partial(\cos\theta)^2}, \tag{C.4}$$

thus finding

$$A = -8\pi \sum_{\ell \ell_1 \ell_2} i^l (2\ell+1)(2\ell_2+1)\sqrt{\frac{(\ell-2)!(\ell_2-2)!}{(\ell+2)!(\ell_2+2)!}}\mathcal{T}_{\ell\ell_1} \begin{pmatrix} \ell & \ell_1 & \ell_2 \\ 0 & 0 & 0 \end{pmatrix} \begin{pmatrix} \ell & \ell_1 & \ell_2 \\ -2 & 0 & 2 \end{pmatrix} \frac{\partial^2 P_\ell(\mu)}{\partial\mu^2}. \tag{C.5}$$

after generalization to an arbitrary frame by replacing $\cos\theta \to \mu$.

Next step of calculation involves finding B, and for that we take

$$\langle v_1 v_1 \rangle = 4\pi \sum_{\ell \ell_1} i^l \sqrt{(2\ell+1)}\sqrt{\pi} \begin{pmatrix} \ell & \ell_1 & 0 \\ 0 & 0 & 0 \end{pmatrix} \begin{pmatrix} \ell & \ell_1 & 0 \\ 0 & 0 & 0 \end{pmatrix}$$
$$\mathcal{T}_{\ell\ell_1} Y_\ell^0(\hat{\mathbf{r}}) - 4\pi \sum_{\ell \ell_1 \ell_2} i^l \sqrt{\pi(2\ell+1)}(2\ell_2+1)\sqrt{\frac{(\ell_2-2)!}{(\ell_2+2)!}}$$
$$\begin{pmatrix} \ell & \ell_1 & \ell_2 \\ 0 & 0 & 0 \end{pmatrix} \begin{pmatrix} \ell & \ell_1 & \ell_2 \\ -2 & 0 & 2 \end{pmatrix} \mathcal{T}_{\ell\ell_1} \left(Y_\ell^2(\hat{\mathbf{r}}) + Y_\ell^{-2}(\hat{\mathbf{r}}) \right). \tag{C.6}$$

The above expression can be simplified by considering the following identities of spherical harmonics

$$Y_\ell^2(\hat{\mathbf{r}}) + Y_\ell^{-2}(\hat{\mathbf{r}}) = 2\sqrt{\frac{(2\ell+1)(\ell-2)!}{4\pi(\ell+2)!}} P_\ell^2(\cos\theta)(2\cos^2\phi - 1), \tag{C.7}$$

and

$$Y_\ell^0(\hat{\mathbf{r}}) = \sqrt{\frac{2l+1}{4\pi}} P_\ell(\cos\theta). \tag{C.8}$$

The second term in Eq.(C.6) contains contribution from A term that is proportional to $\cos^2\phi$. Taking that into account, we have

$$B = 2\pi \sum_{\ell=0,2} i^\ell \mathcal{T}_{\ell\ell} P_\ell(\mu) + 4\pi \sum_{\ell \ell_1 \ell_2} i^l (2\ell+1)(2\ell_2+1)$$
$$\sqrt{\frac{(\ell-2)!(\ell_2-2)!}{(\ell+2)!(\ell_2+2)!}} \begin{pmatrix} \ell & \ell_1 & \ell_2 \\ 0 & 0 & 0 \end{pmatrix} \begin{pmatrix} \ell & \ell_1 & \ell_2 \\ -2 & 0 & 2 \end{pmatrix} \mathcal{T}_{\ell\ell_1} P_\ell^2(\mu). \tag{C.9}$$

To find D, we note that $\langle v_1 v_3 \rangle = 0$, and therefore, in our choice of frame

$D = -A\cos\theta$. Therefore, in general

$$D = 8\pi \sum_{\ell\ell_1\ell_2} i^l (2\ell+1)(2\ell_2+1)\sqrt{\frac{(\ell-2)!(\ell_2-2)!}{(\ell+2)!(\ell_2+2)!}} \begin{pmatrix} \ell & \ell_1 & \ell_2 \\ 0 & 0 & 0 \end{pmatrix} \begin{pmatrix} \ell & \ell_1 & \ell_2 \\ -2 & 0 & 2 \end{pmatrix} \mathcal{T}_{\ell\ell_1\mu} \frac{\partial^2 P_\ell(\mu)}{\partial\mu^2} \tag{C.10}$$

Similarly, we note that $\langle v_3 v_3 \rangle = 0$, and therefore, $C = -A\cos^2\theta - B - 2D\cos\theta = A\cos^2\theta - B$ which gives

$$C = -2\pi \sum_{\ell=0,2} i^\ell \mathcal{T}_{\ell\ell} P_\ell(\mu) - 4\pi \sum_{\ell\ell_1\ell_2} i^l (2\ell+1)(2\ell_2+1) \sqrt{\frac{(\ell-2)!(\ell_2-2)!}{(\ell+2)!(\ell_2+2)!}} \begin{pmatrix} \ell & \ell_1 & \ell_2 \\ 0 & 0 & 0 \end{pmatrix} \begin{pmatrix} \ell & \ell_1 & \ell_2 \\ -2 & 0 & 2 \end{pmatrix} \mathcal{T}_{\ell\ell_1} \left(2\mu^2 \frac{\partial^2 P_\ell(\mu)}{\partial\mu^2} + P_\ell^2(\mu) \right). \tag{C.11}$$

C.2 Fast modes high-β

Fast modes in high β regime are purely compressional type of modes, and their tensor structure is

$$\left(\hat{\xi}_{\mathbf{k}} \otimes \hat{\xi}^*_{\mathbf{k}} \right)_{ij} = \hat{k}_i \hat{k}_j. \tag{C.12}$$

The power spectrum of this mode is isotropic, and therefore we utilise Eq. (B.12) for our calculations. Our first step involves computation of

$$\langle v_1 v_2 \rangle = 4\pi i^2 (-i) \sqrt{\frac{2\pi}{15}} \mathcal{T}_{20}(r) \left(Y_2^2(\hat{\mathbf{r}}) - Y_2^{-2}(\hat{\mathbf{r}}) \right), \tag{C.13}$$

which yields an isotropic form for A

$$A = -4\pi \mathcal{T}_{20}. \tag{C.14}$$

Table C.2: Mode structure of fast Modes in low-β For $\hat{\lambda} = \hat{z}$.

$c^{ij}_{\ell m}$	*Equation*(for even ℓ)
$c^{11}_{\ell m}$	$\sqrt{\pi}\delta_{\ell 0}\delta_{m0} + \Theta(\ell-2)\sqrt{\frac{\pi(2\ell+1)(\ell-2)!}{(\ell+2)!}}(\delta_{m2}+\delta_{m,-2})$
$c^{22}_{\ell m}$	$\sqrt{\pi}\delta_{\ell 0}\delta_{m0} - \Theta(\ell-2)\sqrt{\frac{\pi(2\ell+1)(\ell-2)!}{(\ell+2)!}}(\delta_{m2}+\delta_{m,-2})$
$c^{12}_{\ell m}$	$-i\Theta(\ell-2)\sqrt{\frac{\pi(2\ell+1)(\ell-2)!}{(\ell+2)!}}(\delta_{m2}-\delta_{m,-2})$
$c^{i3}_{\ell m}$	$0, \qquad i \in (1,2,3)$

The next step is to compute

$$\langle v_1 v_1 \rangle = 4\pi \frac{2\sqrt{\pi}}{3}\mathcal{T}_{00}Y_0^0(\hat{\mathbf{r}}) + 4\pi\mathcal{T}_{20}\frac{2}{3}\sqrt{\frac{\pi}{5}}Y_2^0(\hat{\mathbf{r}}) + 4\pi i^2\sqrt{\frac{2\pi}{15}}\mathcal{T}_{20}(r)\left(Y_2^2(\hat{\mathbf{r}}) + Y_2^{-2}(\hat{\mathbf{r}})\right), \tag{C.15}$$

which after subtracting $A\sin^2\theta\cos^2\phi$ contribution gives

$$B = \frac{4\pi}{3}\mathcal{T}_{00}(r) + \frac{4\pi}{3}\mathcal{T}_{20}(r). \tag{C.16}$$

It is easy to check that $C = D = 0$ for this mode. This is expected because both tensor structure as well as power spectrum are isotropic.

C.3 Fast modes low-β

For fast Modes in low β regime, the tensor structure of velocity field in Fourier space is

$$\left(\hat{\xi}_{\mathbf{k}} \otimes \hat{\xi}^*_{\mathbf{k}}\right)_{ij} = \frac{\hat{k}_i\hat{k}_j - (\hat{k}\cdot\hat{\lambda})(\hat{k}_i\hat{\lambda}_j + \hat{k}_j\hat{\lambda}_i) + (\hat{k}\cdot\hat{\lambda})^2\hat{\lambda}_i\hat{\lambda}_j}{1-(\hat{k}\cdot\hat{\lambda})^2}. \tag{C.17}$$

The power spectrum of this mode is isotropic. To find the coefficients

A, B, C and D, our starting point is to utilise the table presented above. Noting the similarity of Table [C.2] with Table [C.1], it is easy to derive these coefficients just by considering the previous results. Similar to the previous section, the velocity has no component along the symmetry axis, so that $D = -A\mu$, and $C = A\mu^2 - B$. Due to the fact that the power spectrum is isotropic in this case, the results heavily simplify, and we have the final result for the correlation coefficients as

$$A = 8\pi \sum_{\ell} i^l (2\ell + 1) \frac{(\ell - 2)!}{(\ell + 2)!} \mathcal{T}_{\ell 0} \frac{\partial^2 P_\ell(\mu)}{\partial \mu^2} \tag{C.18}$$

$$\begin{aligned} B = {} & 2\pi \mathcal{T}_{00} + 4\pi \sum_{n=2,2}^{\infty} i^n (2n + 1) \frac{n!}{(n + 2)!} \mathcal{T}_{n0} P_n(\mu) \\ & - 8\pi \sum_{n=0,2} (2n + 1) P_n(\mu) \sum_{l=n+2,2}^{\infty} i^l (2\ell + 1) \frac{(\ell - 2)!}{(\ell + 2)!} \mathcal{T}_{\ell 0} \end{aligned} \tag{C.19}$$

$$\begin{aligned} C = -2\pi T_{00} + 4\pi \sum_{\ell} i^l (2\ell + 1) \frac{(\ell - 2)!}{(\ell + 2)!} \mathcal{T}_{\ell 0} \Bigg(& P_\ell^2(\mu) \\ & + 2\mu^2 \frac{\partial^2 P_\ell(\mu)}{\partial \mu^2} \Bigg) \end{aligned} \tag{C.20}$$

$$D = -8\pi \sum_{\ell} i^l (2\ell + 1) \frac{(\ell - 2)!}{(\ell + 2)!} \mathcal{T}_{\ell 0} \mu \frac{\partial^2 P_\ell(\mu)}{\partial \mu^2}. \tag{C.21}$$

C.4 Slow modes high-β

The velocity correlation tensor in Fourier Space for slow Modes in high β is

$$\left(\hat{\xi}_{\mathbf{k}} \otimes \hat{\xi}^*_{\mathbf{k}} \right)_{ij} = \left(\frac{(\hat{k} \cdot \hat{\lambda})^2 \hat{k}_i \hat{k}_j + \hat{\lambda}_i \hat{\lambda}_j - (\hat{k} \cdot \hat{\lambda})(\hat{k}_i \hat{\lambda}_j + \hat{k}_j \hat{\lambda}_i)}{1 - (\hat{k} \cdot \hat{\lambda})^2} \right). \tag{C.22}$$

This was identified to be F-type in LP12. Besides the tensor structure, the power spectrum of slow modes is also anisotropic, and is the same as for Alfvén

Table C.3: Mode structure of slow modes in high-β For $\hat{\lambda} = \hat{z}$.

$c_{\ell m}^{ij}$	*Equation*(for even ℓ)
$c_{\ell m}^{11}$	$\frac{\sqrt{\pi}}{3}\delta_{\ell 0}\delta_{m0} + \frac{2}{3}\sqrt{\frac{\pi}{5}}\delta_{\ell 2}\delta_{m0} + \left(\frac{1}{2}\sqrt{\frac{\pi}{30}}\delta_{\ell 2} + \Theta(\ell-4)\sqrt{\frac{\pi(2\ell_2+1)(\ell_2-2)!}{(\ell_2+2)!}}\right)(\delta_{m2} + \delta_{m,-2}).$
$c_{\ell m}^{22}$	$\frac{\sqrt{\pi}}{3}\delta_{\ell 0}\delta_{m0} + \frac{2}{3}\sqrt{\frac{\pi}{5}}\delta_{\ell 2}\delta_{m0} - \left(\frac{1}{2}\sqrt{\frac{\pi}{30}}\delta_{\ell 2} + \Theta(\ell-4)\sqrt{\frac{\pi(2\ell_2+1)(\ell_2-2)!}{(\ell_2+2)!}}\right)(\delta_{m2} + \delta_{m,-2}).$
$c_{\ell m}^{33}$	$\frac{4\sqrt{\pi}}{3}\left(\delta_{\ell 0} - \frac{1}{\sqrt{5}}\delta_{\ell 2}\right)\delta_{m0}$
$c_{\ell m}^{12}$	$-i\left(\frac{1}{2}\sqrt{\frac{\pi}{30}}\delta_{\ell 2} + \Theta(\ell-4)\sqrt{\frac{\pi(2\ell+1)(\ell-2)!}{(\ell+2)!}}\right)(\delta_{m2} - \delta_{m,-2})$
$c_{\ell m}^{13}$	$\sqrt{\frac{2\pi}{15}}\delta_{\ell 2}(\delta_{m1} - \delta_{m,-1})$
$c_{\ell m}^{23}$	$-i\sqrt{\frac{2\pi}{15}}\delta_{\ell 2}(\delta_{m1} + \delta_{m,-1})$

mode.

All the coefficients $c_{\ell m}^{ij}$ relevant for our calculations for this mode are summarised in Table C.3. The first step as usual is to compute the following element

$$\begin{aligned}\langle v_1 v_2\rangle = 4\pi \sum_{\ell\ell_1} i^l \sqrt{\pi(2\ell+1)}\Bigg(&\sqrt{\frac{1}{24}}\begin{pmatrix}\ell & \ell_1 & 2\\ 0 & 0 & 0\end{pmatrix}\begin{pmatrix}\ell & \ell_1 & 2\\ -2 & 0 & 2\end{pmatrix}\\ &+\sum_{\ell_2=4,2}^{\infty}(2\ell_2+1)\sqrt{\frac{(\ell_2-2)!}{(\ell_2+2)!}}\begin{pmatrix}\ell & \ell_1 & \ell_2\\ 0 & 0 & 0\end{pmatrix}\begin{pmatrix}\ell & \ell_1 & \ell_2\\ -2 & 0 & 2\end{pmatrix}\Bigg)\\ &\mathcal{T}_{\ell\ell_1}(-i)\left(Y_\ell^2(\hat{\mathbf{r}}) - Y_\ell^{-2}(\hat{\mathbf{r}})\right)\end{aligned} \tag{C.23}$$

Using the relations for spherical harmonics Eq. (C.3) and Eq. (C.4), we arrive

to the general form

$$A = 8\pi \sum_{\ell\ell_1} i^l (2\ell+1) \sqrt{\frac{(\ell-2)!}{(\ell+2)!}} \left(\sqrt{\frac{1}{24}} \begin{pmatrix} \ell & \ell_1 & 2 \\ 0 & 0 & 0 \end{pmatrix} \begin{pmatrix} \ell & \ell_1 & 2 \\ -2 & 0 & 2 \end{pmatrix} + \sum_{\ell_2=4,2}^{\infty} (2\ell_2+1) \sqrt{\frac{(\ell_2-2)!}{(\ell_2+2)!}} \begin{pmatrix} \ell & \ell_1 & \ell_2 \\ 0 & 0 & 0 \end{pmatrix} \begin{pmatrix} \ell & \ell_1 & \ell_2 \\ -2 & 0 & 2 \end{pmatrix} \right) \mathcal{T}_{\ell\ell_1} \frac{\partial^2 P_\ell(\mu)}{\partial \mu^2}, \quad \text{(C.24)}$$

As a next step, we compute

$$\langle v_1 v_1 \rangle = 4\pi \sum_{\ell\ell_1} i^\ell \sqrt{(2\ell+1)} \left(\frac{\sqrt{\pi}}{3} \begin{pmatrix} \ell & \ell_1 & 0 \\ 0 & 0 & 0 \end{pmatrix}^2 + \frac{2}{3}\sqrt{\pi} \begin{pmatrix} \ell & \ell_1 & 2 \\ 0 & 0 & 0 \end{pmatrix}^2 \right) \mathcal{T}_{\ell\ell_1} Y_\ell^0(\hat{\mathbf{r}}) + 4\pi \sum_{\ell\ell_1} i^l \sqrt{\pi(2\ell+1)} \left(\sqrt{\frac{1}{24}} \begin{pmatrix} \ell & \ell_1 & 2 \\ 0 & 0 & 0 \end{pmatrix} \begin{pmatrix} \ell & \ell_1 & 2 \\ -2 & 0 & 2 \end{pmatrix} + \sum_{\ell_2=4,2}^{\infty} (2\ell_2+1) \sqrt{\frac{(\ell_2-2)!}{(\ell_2+2)!}} \begin{pmatrix} \ell & \ell_1 & \ell_2 \\ 0 & 0 & 0 \end{pmatrix} \begin{pmatrix} \ell & \ell_1 & \ell_2 \\ -2 & 0 & 2 \end{pmatrix} \right) \mathcal{T}_{\ell\ell_1} \left(Y_\ell^2(\hat{\mathbf{r}}) + Y_\ell^{-2}(\hat{\mathbf{r}}) \right). \quad \text{(C.25)}$$

Upon using the identities for spherical harmonics Eq.(C.7), it is easy to see that the second term in the above equation partially contains A contribution. Therefore, after some manipulations, we obtain an expression for B valid in a

general frame:

$$B = \frac{2\pi}{3}\sum_{\ell=0,2} i^{\ell}\mathcal{T}_{\ell\ell}P_{\ell}(\mu) + \frac{4\pi}{3}\sum_{\ell\ell_1} i^{\ell}(2\ell+1)\begin{pmatrix}\ell & \ell_1 & 2\\ 0 & 0 & 0\end{pmatrix}^2$$
$$\mathcal{T}_{\ell\ell_1}P_{\ell}(\mu) - 4\pi\sum_{\ell\ell_1} i^{l}(2\ell+1)\sqrt{\frac{(\ell-2)!}{(\ell+2)!}}\left(\sqrt{\frac{1}{24}}\begin{pmatrix}\ell & \ell_1 & 2\\ 0 & 0 & 0\end{pmatrix}\right.$$
$$\begin{pmatrix}\ell & \ell_1 & 2\\ -2 & 0 & 2\end{pmatrix} + \sum_{\ell_2=4,2}^{\infty}(2\ell_2+1)\sqrt{\frac{(\ell_2-2)!}{(\ell_2+2)!}}\begin{pmatrix}\ell & \ell_1 & \ell_2\\ 0 & 0 & 0\end{pmatrix}$$
$$\left.\begin{pmatrix}\ell & \ell_1 & \ell_2\\ -2 & 0 & 2\end{pmatrix}\right)\mathcal{T}_{\ell\ell_1}P_{\ell}^2(\mu). \qquad \text{(C.26)}$$

Next, to find out D, we compute

$$\langle v_1 v_3\rangle = 4\pi\sum_{\ell\ell_1} i^{\ell}\sqrt{\frac{2\pi}{15}}\sqrt{5(2\ell+1)}\begin{pmatrix}\ell & \ell_1 & \ell_2\\ 0 & 0 & 0\end{pmatrix}$$
$$\begin{pmatrix}\ell & \ell_1 & \ell_2\\ -1 & 0 & 1\end{pmatrix}\mathcal{T}_{\ell\ell_1}(-1)\left(Y_{\ell}^{1}(\hat{\mathbf{r}}) + Y_{\ell}^{-1}(\hat{\mathbf{r}})\right). \qquad \text{(C.27)}$$

With some simplifications, and following the general procedure of subtracting the contribution from A, we finally obtain

$$D = 4\pi\sum_{\ell\ell_1} i^{\ell}(2\ell+1)\sqrt{\frac{2(\ell-1)!}{3(\ell+1)!}}\begin{pmatrix}\ell & \ell_1 & 2\\ 0 & 0 & 0\end{pmatrix}\begin{pmatrix}\ell & \ell_1 & 2\\ -1 & 0 & 1\end{pmatrix}$$
$$\mathcal{T}_{\ell\ell_1}\frac{\partial P_{\ell}(\mu)}{\partial\mu} - 8\pi\sum_{\ell\ell_1} i^{l}(2\ell+1)\sqrt{\frac{(\ell-2)!}{(\ell+2)!}}\left(\sqrt{\frac{1}{24}}\begin{pmatrix}\ell & \ell_1 & 2\\ 0 & 0 & 0\end{pmatrix}\right.$$
$$\begin{pmatrix}\ell & \ell_1 & 2\\ -2 & 0 & 2\end{pmatrix} + \sum_{\ell_2=4,2}^{\infty}(2\ell_2+1)\sqrt{\frac{(\ell_2-2)!}{(\ell_2+2)!}}\begin{pmatrix}\ell & \ell_1 & \ell_2\\ 0 & 0 & 0\end{pmatrix}$$
$$\left.\begin{pmatrix}\ell & \ell_1 & \ell_2\\ -2 & 0 & 2\end{pmatrix}\right)\mathcal{T}_{\ell\ell_1}\mu\frac{\partial^2 P_{\ell}(\mu)}{\partial\mu^2}. \qquad \text{(C.28)}$$

Final set of calculation involves computing

$$\langle v_3 v_3 \rangle = 4\pi \sum_{\ell\ell_1} i^\ell \frac{4\sqrt{(2\ell+1)}}{3}\sqrt{\pi} \begin{pmatrix} \ell & \ell_1 & 0 \\ 0 & 0 & 0 \end{pmatrix}^2 \mathcal{T}_{\ell\ell_1} Y_\ell^0(\hat{\mathbf{r}}) \\ -4\pi \sum_{\ell\ell_1} i^\ell \frac{4\sqrt{(2\ell+1)}}{3}\sqrt{\pi} \begin{pmatrix} \ell & \ell_1 & 2 \\ 0 & 0 & 0 \end{pmatrix}^2 \mathcal{T}_{\ell\ell_1} Y_\ell^0(\hat{\mathbf{r}}), \tag{C.29}$$

which after considering possible contribution from all other coefficients, we finally arrive to an expression for C valid at all frames:

$$C = 2\pi \sum_\ell i^\ell \mathcal{T}_{\ell\ell} P_\ell(\mu) - 4\pi \sum_{\ell\ell_1} i^\ell (2\ell+1) \begin{pmatrix} \ell & \ell_1 & 2 \\ 0 & 0 & 0 \end{pmatrix}^2 \mathcal{T}_{\ell\ell_1} P_\ell(\mu) \\ - 8\pi \sum_{\ell\ell_1} i^\ell (2\ell+1) \sqrt{\frac{2(\ell-1)!}{3(\ell+1)!}} \begin{pmatrix} \ell & \ell_1 & 2 \\ 0 & 0 & 0 \end{pmatrix} \begin{pmatrix} \ell & \ell_1 & 2 \\ -1 & 0 & 1 \end{pmatrix} \mathcal{T}_{\ell\ell_1} \\ \mu \frac{\partial P_\ell(\mu)}{\partial \mu} + 4\pi \sum_{\ell\ell_1} i^l (2\ell+1) \sqrt{\frac{(\ell-2)!}{(\ell+2)!}} \left(\sqrt{\frac{1}{24}} \begin{pmatrix} \ell & \ell_1 & 2 \\ 0 & 0 & 0 \end{pmatrix} \right. \\ \begin{pmatrix} \ell & \ell_1 & 2 \\ -2 & 0 & 2 \end{pmatrix} + \sum_{\ell_2=4,2}^{\infty} (2\ell_2+1) \sqrt{\frac{(\ell_2-2)!}{(\ell_2+2)!}} \begin{pmatrix} \ell & \ell_1 & \ell_2 \\ 0 & 0 & 0 \end{pmatrix} \\ \left. \begin{pmatrix} \ell & \ell_1 & \ell_2 \\ -2 & 0 & 2 \end{pmatrix} \right) \mathcal{T}_{\ell\ell_1} \left(P_\ell^2(\mu) + 2\mu^2 \frac{\partial^2 P_\ell(\mu)}{\partial \mu^2} \right). \tag{C.30}$$

C.5 Slow modes low-β

Slow modes in low β have the tensor structure

$$\left(\hat{\xi}_{\mathbf{k}} \otimes \hat{\xi}_{\mathbf{k}}^* \right)_{ij} \propto \hat{\lambda}_i \hat{\lambda}_j. \tag{C.31}$$

It is clear from the above tensor structure that $c^{ij}_{\ell_2 m_2}$ is only non-zero for $\ell_2 = m_2 = 0$. This heavily simplifies Eq.B.11, and subsequent calculation allows us

Table C.4: Mode structure of strong turbulence

$c_{\ell m}^{ij}$	*Equation*
$c_{\ell m}^{11}$	$\left(\frac{4\sqrt{\pi}}{3}\delta_{l0}+\frac{2\sqrt{\pi}}{3\sqrt{5}}\delta_{l2}\right)\delta_{m0}-\sqrt{\frac{2\pi}{15}}\delta_{l2}(\delta_{m2}+\delta_{m,-2})$
$c_{\ell m}^{22}$	$\left(\frac{4\sqrt{\pi}}{3}\delta_{l0}+\frac{2\sqrt{\pi}}{3\sqrt{5}}\delta_{l2}\right)\delta_{m0}+\sqrt{\frac{2\pi}{15}}\delta_{l2}(\delta_{m2}+\delta_{m,-2})$
$c_{\ell m}^{33}$	$\left(\frac{4\sqrt{\pi}}{3}\delta_{l0}-\frac{4\sqrt{\pi}}{3\sqrt{5}}\delta_{l2}\right)\delta_{m0}$
$c_{\ell m}^{12}$	$i\sqrt{\frac{2\pi}{15}}\delta_{l2}(\delta_{m2}-\delta_{m,-2})$
$c_{\ell m}^{13}$	$\sqrt{\frac{2\pi}{15}}\delta_{l2}(\delta_{m1}-\delta_{m,-1})$
$c_{\ell m}^{23}$	$-i\sqrt{\frac{2\pi}{15}}\delta_{l2}(\delta_{m1}+\delta_{m,-1})$

to compute C and arrive to a general form

$$C=\sum_{\ell}4\pi i^{\ell}\mathcal{T}_{\ell\ell}P_{\ell}(\mu). \tag{C.32}$$

All other coefficients vanish in this mode.

C.6 Strong turbulence

In a strong turbulence with the uncorrelated mix of equal power Alfvén and slow modes, we expect pure E-type correlation, which has a Fourier component

$$\left(\hat{\xi}_{\mathbf{k}}\otimes\hat{\xi}_{\mathbf{k}}^{*}\right)_{ij}=(\delta_{ij}-\hat{\mathbf{k}}_{i}\hat{\mathbf{k}}_{j}). \tag{C.33}$$

The real space correlation function has been already derived in LP12 using Chandrashekhar's notations, but here we derive it using the formalism we developed in the previous section. We will use Table C.4 in the subsequent calculations in this section. To find the coefficients A, B, C and D, we follow

the procedure described in Appendix B. Consider

$$\langle v_1 v_2 \rangle = 4\pi \sum_{\ell} i^{\ell} \sum_{\ell_1} \sqrt{\frac{2\pi}{3}} \sqrt{(2\ell+1)} \mathcal{T}_{\ell\ell_1} \begin{pmatrix} \ell & \ell_1 & 2 \\ 0 & 0 & 0 \end{pmatrix} \begin{pmatrix} \ell & \ell_1 & 2 \\ -2 & 0 & 2 \end{pmatrix} i(Y_{\ell}^{2}(\hat{\mathbf{r}}) - Y_{\ell}^{-2}(\hat{\mathbf{r}})). \tag{C.34}$$

In the frame we are dealing with, only $\hat{\mathbf{r}}_1 \hat{\mathbf{r}}_2$ contributes, and therefore upon simplification, we obtain (after considering that A should only depend on $\mu = \hat{r}.\hat{\lambda}$),

$$A = -8\pi \sum_{\ell} i^{\ell} \sum_{\ell_1} (2\ell+1) \sqrt{\frac{2(\ell-2)!}{3(\ell+2)!}} \mathcal{T}_{\ell\ell_1} \begin{pmatrix} \ell & \ell_1 & 2 \\ 0 & 0 & 0 \end{pmatrix} \begin{pmatrix} \ell & \ell_1 & 2 \\ -2 & 0 & 2 \end{pmatrix} \frac{\partial^2 P_{\ell}(\mu)}{\partial \mu^2}. \tag{C.35}$$

Similarly, we compute

$$\langle v_1 v_1 \rangle = \frac{8\pi}{3} \sum_{\ell} i^{\ell} \mathcal{T}_{\ell\ell} P_{\ell}(\cos\theta) + \frac{4\pi}{3} \sum_{\ell\ell_1} i^{\ell} (2\ell+1) \mathcal{T}_{\ell\ell_1} \begin{pmatrix} \ell & \ell_1 & 2 \\ 0 & 0 & 0 \end{pmatrix}^2 P_{\ell}(\cos\theta) - 4\pi \sum_{\ell\ell_1} i^{\ell} \sqrt{\frac{2\pi}{3}} \sqrt{(2\ell+1)} \mathcal{T}_{\ell\ell_1} \begin{pmatrix} \ell & \ell_1 & 2 \\ 0 & 0 & 0 \end{pmatrix} \begin{pmatrix} \ell & \ell_1 & 2 \\ -2 & 0 & 2 \end{pmatrix} (Y_{\ell}^{2}(\hat{\mathbf{r}}) + Y_{\ell}^{-2}(\hat{\mathbf{r}})). \tag{C.36}$$

In our choice of co-ordinates, $\langle v_1 v_1^* \rangle$ is contributed by A and B. Therefore to find B, we need to subtract the contribution of A. This subtraction affects the

last factor in the above equation, and we are left with

$$B = \frac{8\pi}{3}\sum_{\ell} i^{\ell}\mathcal{T}_{\ell\ell}P_{\ell}(\mu) + \frac{4\pi}{3}\sum_{\ell\ell_1} i^{\ell}(2\ell+1)\mathcal{T}_{\ell\ell_1}\begin{pmatrix}\ell & \ell_1 & 2\\ 0 & 0 & 0\end{pmatrix}^2 P_{\ell}(\mu) + 4\pi\sum_{\ell\ell_1} i^{\ell}(2\ell+1)\sqrt{\frac{2(\ell-2)!}{3(\ell+2)!}}\mathcal{T}_{\ell\ell_1}\begin{pmatrix}\ell & \ell_1 & 2\\ 0 & 0 & 0\end{pmatrix}\begin{pmatrix}\ell & \ell_1 & 2\\ -2 & 0 & 2\end{pmatrix}P_{\ell}^2(\mu). \tag{C.37}$$

Next, we compute

$$\langle v_1 v_3\rangle = 4\pi\sum_{\ell\ell_1} i^{\ell}\sqrt{\frac{2\pi}{3}}\sqrt{(2\ell+1)}\mathcal{T}_{\ell\ell_1}\begin{pmatrix}\ell & \ell_1 & 2\\ 0 & 0 & 0\end{pmatrix}\begin{pmatrix}\ell & \ell_1 & 2\\ -1 & 0 & 1\end{pmatrix}(-1)(Y_{\ell}^{1}(\hat{\mathbf{r}}) + Y_{\ell}^{*1}(\hat{\mathbf{r}})). \tag{C.38}$$

Using the fact that the above correlation is contributed by A and D, and subtracting the contribution of A, we finally obtain

$$D = 4\pi\sum_{\ell\ell_1} i^{\ell}(2\ell+1)\sqrt{\frac{2(\ell-1)!}{3(\ell+1)!}}\mathcal{T}_{\ell\ell_1}\begin{pmatrix}\ell & \ell_1 & 2\\ 0 & 0 & 0\end{pmatrix}\begin{pmatrix}\ell & \ell_1 & 2\\ -1 & 0 & 1\end{pmatrix}\frac{\partial P_{\ell}(\mu)}{\partial\mu} + 8\pi\sum_{\ell\ell_1} i^{\ell}(2\ell+1)\sqrt{\frac{2(\ell-2)!}{3(\ell+2)!}}\mathcal{T}_{\ell\ell_1}\begin{pmatrix}\ell & \ell_1 & 2\\ 0 & 0 & 0\end{pmatrix}\begin{pmatrix}\ell & \ell_1 & 2\\ -2 & 0 & 2\end{pmatrix}\mu\frac{\partial^2 P_{\ell}(\mu)}{\partial\mu^2}. \tag{C.39}$$

Finally, to obtain C we compute

$$\langle v_3 v_3 \rangle = \frac{8\pi}{3} \sum_{\ell} i^{\ell} \mathcal{T}_{\ell\ell} P_{\ell}(\cos\theta) - \frac{8\pi}{3} \sum_{\ell\ell_1} i^{\ell} (2\ell+1) \mathcal{T}_{\ell\ell_1} \begin{pmatrix} \ell & \ell_1 & 2 \\ 0 & 0 & 0 \end{pmatrix}^2 P_{\ell}(\cos\theta) \tag{C.40}$$

The above correlation comes from the contribution of A, B, C and D. Therefore, to find C, we subtract all other contributions to obtain

$$\begin{aligned} C = -4\pi \sum_{\ell\ell_1} i^{\ell} (2\ell+1) \mathcal{T}_{\ell\ell_1} \begin{pmatrix} \ell & \ell_1 & 2 \\ 0 & 0 & 0 \end{pmatrix}^2 P_{\ell}(\mu) - 8\pi \\ \sum_{\ell\ell_1} i^{\ell} (2\ell+1) \sqrt{\frac{2(\ell-1)!}{3(\ell+1)!}} \mathcal{T}_{\ell\ell_1} \begin{pmatrix} \ell & \ell_1 & 2 \\ 0 & 0 & 0 \end{pmatrix} \begin{pmatrix} \ell & \ell_1 & 2 \\ -1 & 0 & 1 \end{pmatrix} \\ \mu \frac{\partial P_{\ell}(\mu)}{\partial \mu} - 4\pi \sum_{\ell\ell_1} i^{\ell} (2\ell+1) \sqrt{\frac{2(\ell-2)!}{3(\ell+2)!}} \mathcal{T}_{\ell\ell_1} \begin{pmatrix} \ell & \ell_1 & 2 \\ 0 & 0 & 0 \end{pmatrix} \\ \begin{pmatrix} \ell & \ell_1 & 2 \\ -2 & 0 & 2 \end{pmatrix} \left(P_{\ell}^2(\mu) + 2\mu^2 \frac{\partial^2 P_{\ell}(\mu)}{\partial \mu^2} \right) \end{aligned} \tag{C.41}$$

Appendix D

Approximate Expression For The $z-$ Projection Of The Velocity Structure Function

To study intensity maps analytically, we require knowledge of the $z-$ projection of velocity structure function. An anisotropic velocity structure function manifests in the anisotropy of intensity channel maps. Therefore, for our analytical calculation, we first study how anisotropy is built in the $z-$ projection of the velocity structure function. The projection structure function is given

$$D_z(\mathbf{r}) = 2[(B(0) - B) + (C(0) - C)\cos^2\gamma - A\cos^2\theta \\ -2D\cos\theta\cos\gamma] \ , \tag{D.1}$$

where A, B, C and D depend on the particular mode of turbulence and has been derived in Appendix [C] for different modes of turbulence. For the analysis we carry out, it is particularly useful to do the multipole decomposition of these coefficients in Legendre polynomials, so that

$$A = \sum_n A_n(r) P_n(\mu) \ , \tag{D.2}$$

and so on, where $A_n(r)$ can be easily obtained with the knowledge of A. The expression above is particularly useful to obtain approximate expression for $D_z(r,\mu)$, as the coefficients $A_n(r)$ are usually a decreasing function of n. This motivates us to write $D_z(r,\mu)$ by considering the coefficients only upto second order in n, i.e. $A = A_0 + A_2 P_2(\mu)$ and so on. We define that the power spectrum $\mathcal{A}_{\ell_1} \propto k^{-m}$ (cf. Eq. (2.13)). Keeping this in mind, it can be shown that each regularised coefficients $A, B(0)-B, C(0)-C, D$ are proportional to $r^{m-3} \equiv r^{\nu}$. Since $A, B, ..$ are functions of r in the same fashion, we explicitly factor out r^{ν} from them, so that in the following analysis, it is to be understood that any r^{ν} factor comes from these coefficients, and $A_n, ..$ are simply some numerical constants. With these approximations and definitions, Eq. (D.1) can be written as

$$\begin{aligned} D_z(\mathbf{r}) \approx 2[&(B_0(0) - B_0(r) - B_2(r)P_2(\mu)) + (C_0(0) - C_0(r) \\ &-C_2(r)P_2(\mu))\cos^2\gamma - (A_0(r) + A_2(r)P_2(\mu))\cos^2\theta \\ &-2D_1(r)\mu\cos\theta\cos\gamma] \end{aligned} \tag{D.3}$$

To obtain the explicit dependence of D_z on ϕ, we use the relation for μ in-terms of different angles involved in our setup

$$\mu = \sin\gamma\sin\theta\cos\phi + \cos\gamma\cos\theta, \tag{D.4}$$

which when used in Eq. (D.3) shows that D_z is related to ϕ only upto $\cos^2\phi$:

$$D_z(\mathbf{r}) \approx c_1 - c_2\cos\phi - c_3\cos^2\phi. \tag{D.5}$$

The detailed relations involving parameters c_1, c_2 and c_3 are presented in the Table [D.1]. For the sake of clarity, these parameters are themselves broken into different pieces. As we will show later, this representation will be useful when carrying out the $z-$ integral to find the intensity structure function.

Table D.1: Different parameters in the approximate D_z

Parameters	*Equation*
c_1	$(q_1 + q_2 \cos^2\theta + q_3 \cos^4\theta) r^\nu$
c_2	$(s_1 + s_2 \cos^2\theta) r^\nu \sin\theta \cos\theta \sin\gamma \cos\gamma$
c_3	$(u_1 + u_2 \cos^2\theta) r^\nu \sin^2\theta \sin^2\gamma$
q_1	$2(B_0(0) - B_0) + 2(C_0(0) - C_0)\cos^2\gamma + B_2 + C_2 \cos^2\gamma.$
q_2	$-2A_0 + A_2 - 4D_1 \cos\gamma - 3(B_2 + C_2 \cos^2\gamma)\cos^2\gamma$
q_3	$-3A_2 \cos^2\gamma$
s_1	$6(B_2 + C_2 \cos^2\gamma) + 4D_1$
s_2	$6A_2$
u_1	$3(B_2 + C_2 \cos^2\gamma)$
u_2	$3A_2$

For the sake of convenience for further analysis, we write Eq. (D.5) as

$$D_z(\mathbf{r}) \approx f_1(1 - f_2 \cos\phi - f_3 \cos^2\phi), \tag{D.6}$$

where,

$$f_1 = c_1, \qquad f_2 = \frac{c_2}{c_1}, \qquad f_3 = \frac{c_3}{c_1}. \tag{D.7}$$

Appendix E

Evaluating ϕ Integral for Pure Velocity Term

In order to fully obtain multipole moments of intensity structure function (cf. 4.4), we need to evaluate the integral of the form

$$\int_0^{2\pi} d\phi \frac{\mathrm{e}^{-im\phi}}{\sqrt{f_1(1 - f_2\cos\phi - f_3\cos^2\phi)}}.$$

To evaluate this integral, we will use generalised Gegenbauer polynomial expansion (Plunkett and Jain, 1975) defined as

$$\frac{1}{(1 - \rho x - \zeta x^2)^\alpha} = \sum_{n=0}^{\infty} C_n^{(\alpha)}(\rho, \zeta) x^n, \tag{E.1}$$

where, $\rho + \zeta < 1$, and

$$\begin{aligned} C_n^{(\alpha)}(\rho, \zeta) =& \frac{\rho^n \Gamma[\alpha + n - 1]}{\Gamma[\alpha] n!} \\ & {}_2F_1\left(-\frac{n}{2}, \frac{-n+1}{2}; -\alpha - n + 2; \frac{-4\zeta}{\rho^2}\right) \end{aligned} \tag{E.2}$$

or equivalently

$$C_n^{(\alpha)}(\rho) = \sum_{j=0}^{\lfloor n/2 \rfloor} \frac{\Gamma(n-j+\alpha)}{\Gamma(\alpha) j! \Gamma[n-2j+1]} \zeta^j \rho^{n-2j}. \tag{E.3}$$

Using the above equations we can write

$$\begin{aligned}
&\int_0^{2\pi} \mathrm{d}\phi \frac{\mathrm{e}^{-im\phi}}{\sqrt{f_1(1-f_2\cos\phi - f_3\cos^2\phi)}} \\
&\quad = \sum_{n=0}^{\infty} \frac{C_n^{(1/2)}(f_2,f_3)}{\sqrt{f_1}} \int_0^{2\pi} d\phi \mathrm{e}^{-im\phi} \cos^n\phi \\
&\quad = \sum_{n=m,2}^{\infty} \frac{2^{-n} C_n^{(1/2)}(f_2,f_3)}{\sqrt{f_1}} \frac{2\pi\Gamma[n+1]}{\Gamma\left[\frac{n-m}{2}+1\right]\Gamma\left[\frac{n+m}{2}+1\right]},
\end{aligned} \tag{E.4}$$

where the sum in n starts at m and proceeds at a step of 2, which implies that m and n should have the same parity. This parity information is particularly useful later to arrive to the conclusion that only even multipoles survive. For any $n < m$, the integral is zero, therefore, these terms have no contribution. Upon using definition of $C_n^{(1/2)}$, and considering the fact that n is positive to write $\Gamma[n+1] = n!$, we have

$$\begin{aligned}
&\int_0^{2\pi} \mathrm{d}\phi \frac{\mathrm{e}^{-im\phi}}{\sqrt{f_1(1-f_2\cos\phi - f_3\cos^2\phi)}} \\
&= \sum_{n=m,2}^{\infty} \frac{2\sqrt{\pi}}{\sqrt{f_1}} \frac{2^{-n}\sin^n\gamma\Gamma\left[n+1\right]}{\Gamma\left[\frac{n-m}{2}+1\right]\Gamma\left[\frac{n+m}{2}+1\right]} \sum_{j=0}^{\lfloor n/2 \rfloor} \frac{\Gamma\left[n-j+\frac{1}{2}\right]}{j!\Gamma[n-2j+1]} \\
&\qquad (\cos\gamma)^{n-2j} f_3^j f_2^{n-2j}.
\end{aligned} \tag{E.5}$$

Appendix F

Evaluating z Integral for Pure Velocity Term

To obtain multipole moments of the intensity structure function, we now carry out the $z-$ integral (cf. Eq. 4.4)

$$\int_{-\infty}^{\infty} dz \, \frac{1}{\sqrt{f_1}} f_3^j f_2^{n-2j} = \int_{-\infty}^{\infty} dz \, c_1^{-n+j-1/2} c_2^{n-2j} c_3^j$$
$$= \int_{-\infty}^{\infty} dz \cos^{n-2j}\theta (q_1 + q_2 \cos^2\theta + q_3 \cos^4\theta)^{-n+j-1/2}$$
$$(s_1 + s_2 \cos^2\theta)^{n-2j} (u_1 + u_2 \cos^2\theta)^j \sin^n\theta r^{-\nu/2}. \tag{F.1}$$

Using $\sin\theta = R/r$, and $\cos\theta = z/r$, we have

$$\int_{-\infty}^{\infty} dz \, \frac{1}{\sqrt{f_1}} f_3^j f_2^{n-2j} = \int_{-\infty}^{\infty} \mathrm{d}z \, r^{-\nu/2-2(n-j)} R^n z^{n-2j}$$
$$(q_1 + q_2 r^{-2} z^2 + q_3 r^{-4} z^4)^{-n+j-1/2}$$
$$(s_1 + s_2 r^{-2} z^2)^{n-2j} (u_1 + u_2 r^{-2} z^2)^j. \tag{F.2}$$

One of the most important points to note at this stage is that for odd n, the above integral vanishes, since for odd n, z^{n-2j} is an odd function in z, while all other functions involved in this problem are even. This implies that the

multipole contribution, which is the weight of $e^{-im\phi}$, comes only from even m, which is consistent with the symmetry of our problem.

Note that the above is valid only when $n \geq 2$, for $\nu > 0$. When $n = 0$, we have to consider regularization of the integral (cf. Eq. (4.4)). The integral we are interested at, when $n = 0$, is

$$\mathcal{I}_0 = \int_{-\infty}^{\infty} dz \left[\frac{1}{\sqrt{q_1 + q_2 + q_3} z^{\nu/2}} - \frac{1}{\sqrt{q_1 + q_2 \cos^2\theta + q_3 \cos^4\theta} r^{\nu/2}} \right] \tag{F.3}$$

which after change of variable $z = R\cot\theta$ can also be written as

$$\mathcal{I}_0 = R^{1-\nu/2} \int_0^{\pi} \mathrm{d}\theta \frac{1}{\sin^2\theta} \left[\frac{(\tan\theta)^{\nu/2}}{\sqrt{q_1 + q_2 + q_3}} - \frac{(\sin\theta)^{\nu/2}}{\sqrt{q_1 + q_2 \cos^2\theta + q_3 \cos^4\theta}} \right]. \tag{F.4}$$

An approximate form of (F.3) can be obtained by method of series expansion. For that we write the integrand as

$$\begin{aligned} &\frac{1}{\sqrt{q_1 + q_2 + q_3} z^{\nu/2}} - \frac{1}{\sqrt{q_1 + q_2 \cos^2\theta + q_3 \cos^4\theta} r^{\nu/2}} \\ &\approx \frac{1}{\sqrt{q_1 + q_2} z^{\nu/2}} - \frac{1}{\sqrt{q_1 + q_2 \frac{z^2}{R^2 + z^2}} r^{\nu/2}} \\ &\approx \left[\frac{1}{\sqrt{q_1 + q_2} z^{\nu/2}} - \frac{1}{\sqrt{q_1 + q_2} r^{\nu/2}} \right] + \frac{q_2 R^2}{2(q_1 + q_2)^{3/2} r^{2+\nu/2}}, \end{aligned} \tag{F.5}$$

where in the first step, we used the fact that q_3 contribution is negligible[1]. The above approximation is fairly good as long as $q_1 + q_2 > q_2$. With this

[1] We verified this numerically. Analytically this can be understood by noting that q_1 and q_2 consists of monopole contribution while q_3 consists of only quadrupole contribution (cf. Table. D.1).

approximation, we finally arrive to

$$\mathcal{I}_0 \approx -R^{1-\nu/2}\sqrt{\frac{\pi}{q_1+q_2}}\left[\frac{\Gamma\left(\frac{\nu}{4}-\frac{1}{2}\right)}{\Gamma\left(\frac{\nu}{4}\right)} - \frac{q_2}{2(q_1+q_2)}\frac{\Gamma\left(\frac{\nu}{4}+\frac{1}{2}\right)}{\Gamma\left(\frac{\nu}{4}+1\right)}\right]. \tag{F.6}$$

To evaluate Eq.(F.2) we first note the the following: due to the presence of a factor z^{n-2j}, which is a suppressing factor for small z, and for $n \neq 2j$, the integral in Eq. (F.2) gives significantly small value when $n \neq 2j$ in comparison to the case when $n = 2j$. Therefore, we will only consider the case when $n = 2j$. To make further simplifications, we approximate the integrand as

$$\begin{aligned} r^{-\nu/2-n}R^n(q_1+q_2r^{-2}z^2+q_3r^{-4}z^4)^{-n/2-1/2}(u_1+u_2r^{-2}z^2)^{n/2} \\ \approx r^{-\nu/2-n}R^n(q_1+q_2r^{-2}z^2)^{-n/2-1/2}u_1^{n/2} \\ \approx r^{-\nu/2-n}R^n q_1^{-n/2-1/2}u_1^{n/2}\left(1-\frac{n+1}{2}\frac{q_2}{q_1}\frac{z^2}{r^2}\right), \end{aligned} \tag{F.7}$$

where we have carried out expansion valid for $q_1 > q_2$. Therefore, we finally have

$$\mathcal{I} \approx R^{1-\nu/2}\frac{\sqrt{\pi}}{q_1^{(n+1)/2}}\left(\frac{\Gamma\left(\frac{\nu}{4}+\frac{n-1}{2}\right)}{\Gamma\left(\frac{\nu}{4}+\frac{n}{2}\right)} - \frac{(n+1)}{4}\frac{q_2}{q_1}\frac{\Gamma\left(\frac{\nu}{4}+\frac{n+1}{2}\right)}{\Gamma\left(\frac{\nu}{4}+\frac{n}{2}+1\right)}\right)u_1^{n/2}. \tag{F.8}$$

Eqs. (F.6, F.8) allow us to obtain multipole moment of any even order.